The Dissertation Committee for Yonghyun Kim Certifies that this is the approved version of the following dissertation:

Atomic-Scale Modeling and Experimental Studies for Dopants and Defects in Si and SiGe Nano-scale CMOS Devices

Committee:

Sanjay K. Banerjee, Supervisor

Taras A. Kirichenko, Co-Supervisor

Jack C. Lee

Leonard F. Register

Emanuel Tutuc

Graeme Henkelman

Atomic-Scale Modeling and Experimental Studies
for Dopants and Defects in Si and SiGe Nano-scale CMOS Devices

by

Yonghyun Kim, B.S.; M.S.

Dissertation

Presented to the Faculty of the Graduate School of

The University of Texas at Austin

in Partial Fulfillment

of the Requirements

for the Degree of

Doctor of Philosophy

The University of Texas at Austin

May, 2010

Dedication

To my Parents and Families

Acknowledgements

Atomic-Scale Modeling and Experimental Studies
for Dopants and Defects in Si and SiGe Nano-scale CMOS Devices

Publication No._____

Yonghyun Kim, Ph.D.

The University of Texas at Austin, 2010

Supervisor: Sanjay K. Banerjee

Co-Supervisor: Taras A. Kirichenko

Continued scaling of CMOS devices with Si and Si_xGe_{1-x} down to 22 nm design node or beyond will require the formation of ever shallower and more abrupt junctions with higher doping levels in order to manage the short channel effects. With the increasing importance of surface proximity and stress effects, the lateral diffusion in gate-extension overlap region strongly influences both threshold voltage roll-off degradation and DIBL increase by requiring an optimized abruptness and diffusion for better device performance. Therefore, the detailed understanding of defect-dopant interactions in the disordered and/or strained systems is essential to develop a predictive kinetic model for the evolution of dopant concentration and electrical activation profiles. Our density functional theory calculations provide the guidance for experimental designs to realize ultra-shallow junction formation required for future generations of nano-scale CMOS devices.

Few systematic studies in epitaxially-grown Si_xGe_{1-x} channel CMOS have been reported. The physical mechanisms of boron diffusion in strained Si_xGe_{1-x}/Si heterojunction layers with different Si_xGe_{1-x} layer thicknesses and Ge content (>50%) are addressed, especially with high temperature annealing. In addition, the effects of the fluorine incorporated during BF_2 implant on boron diffusion are investigated to provide more insight into short channel device design. In this study, we investigate how short channel margins are affected by Ge mole fraction and Si_xGe_{1-x} layer thickness in a compressively strained Si_xGe_{1-x}/Si heterojunction PMOS with high temperature annealing.

Series resistance characterization in S/D extension region and gate oxide interface trap characterization for Si, Si_xGe_{1-x}, and Ge nMOSFETs are done. TCAD device simulation is also performed to evaluate which distributions of interface traps will significantly affect the electrical characteristics such as flatband voltage (V_{FB}) shift and threshold voltage (V_{th}) shift based on capacitance-voltage (CV) and current-voltage (IV) curves. n^+/p and p^+/n diode structures are studied in order to decouple the electrical characteristics from the gated-diode (GD) MOSFETs. With the extraction of S/D series resistance from various channel lengths, possible reasons for performance degradation in Si_xGe_{1-x} and Ge nMOSFETs, based on simulations, are proposed.

Table of Contents

List of Tables

xi

List of Figures

xiv

CHAPTER 1: RESEARCH BACKGROUND

1.1 MOTIVATION

According to the 2007 International Technology Roadmap for Semiconductors (ITRS), scaling CMOS beyond the 22 nm node and beyond may require moving away from bulk CMOS in Si with SiO_2 gate dielectrics [1]. Existing understanding for implant and diffusion will not be enough for such novel materials and device structures characterized by non-planar topographies and high surface-to-volume ratios. In addition, strained silicon, silicon-on-insulator (SOI), and Si_xGe_{1-x} will make it difficult to obtain the detailed understanding of junction formation, amorphization/regrowth, interface kinetics, and extended defect behavior [1]. The ability to form ever shallower and more abrupt junctions while maintaining or increasing dopant activation is at the heart of technology scaling in order to minimize short channel effects and series resistance. Detailed understanding of dopant-defect annealing and activation remains a challenging problem, particularly with the move towards very low thermal budget flows and millisecond annealing techniques where ion implantation damage may not be fully removed.

1.2 ATOMIC SCALE MODELING FOR DEFECT AND DOPANT INTERACTIONS

1.2.1 Dopant Diffusion and Modeling Approach

Technology computer-aided design (TCAD) has become essential to advanced technology development, contributing to every aspect of semiconductor technology development from front-end process and device modeling to equipment and lithography modeling [2]. Without an extensive use of TCAD tools, the complexity is such that technology development cannot be successfully completed in almost every aspect of aggressively scaled CMOS technology. Front-end process and device simulation has

played a critical role by giving insight into the relationships between processing choices and device performance that cannot be obtained from physical metrology tools alone [2]. Therefore, TCAD simulations have become a key enabler for the semiconductor industry to continue to achieve increasing device density and performance with high yield and manufacturability.

In the areas of front-end process modeling, atomic-scale process modeling of defect and dopant interactions has significantly enabled the deeper understanding in the diffusion and clustering of dopants and defects during implantation and post-implantation annealing. Based on multiscale modeling approach with fundamental physical properties as shown in Fig. 1.1, the comprehensive models capable of predicting dopant concentration and activated electrical concentrations during ultrashallow junction formation can be incorporated in large-scale kinetic Monte Carlo (KMC) and continuum simulation methods.
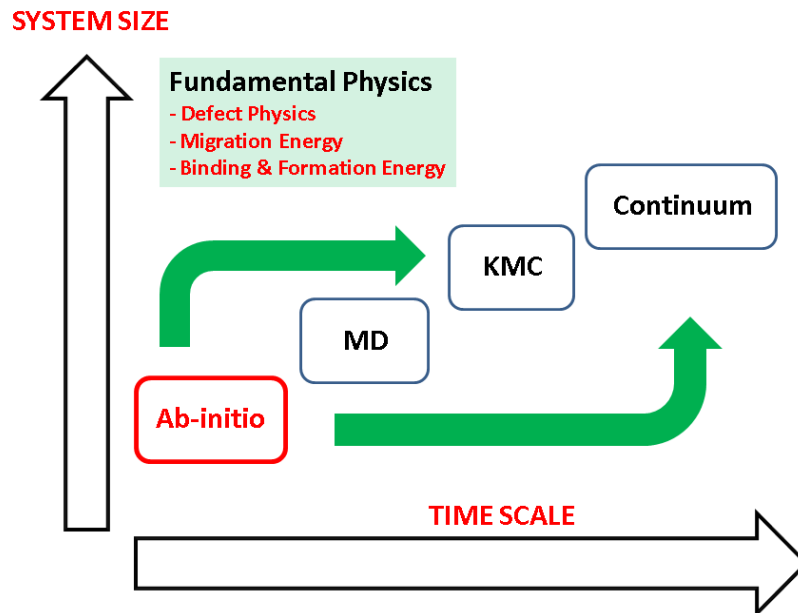
FIGURE 1.1: Multiscale modeling approach for defect-dopant interaction.
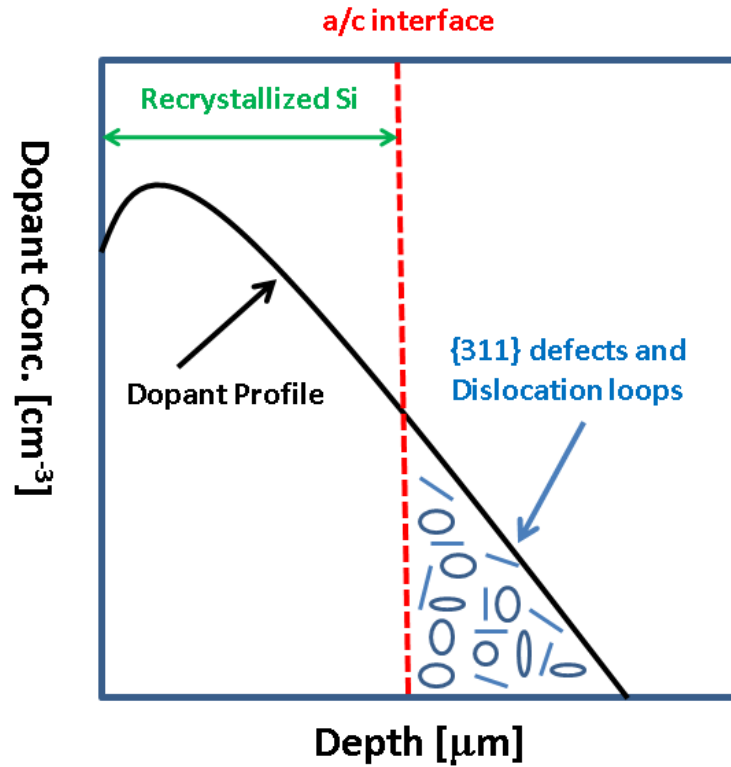
FIGURE 1.2: Schematic diagram of junction formation and re-crystallization in silicon during the subsequent annealing after implant-induced damage.

When dopants are implanted into silicon, the silicon is amorphized with both interstitial and vacancy defects due to crystal damage depending on the implant energy and dose. While Frenkel pairs are generated, there are excess interstitials equal to the number of implanted dopants when silicon is annealed because the dopants finally occupy a lattice site, which is referred as "+1 model" [3]. During the subsequent annealing to re-crystallize the silicon, interstitial-vacancy (IV) recombination and vacancy diffusion to the surface reduce the defect population [4-6]. Then, interstitials are left beyond the projected range of the dopant where they can form extended defects such as {311} rod-like defects and dislocation loops, as shown in Fig. 1.2 [4-6].

3
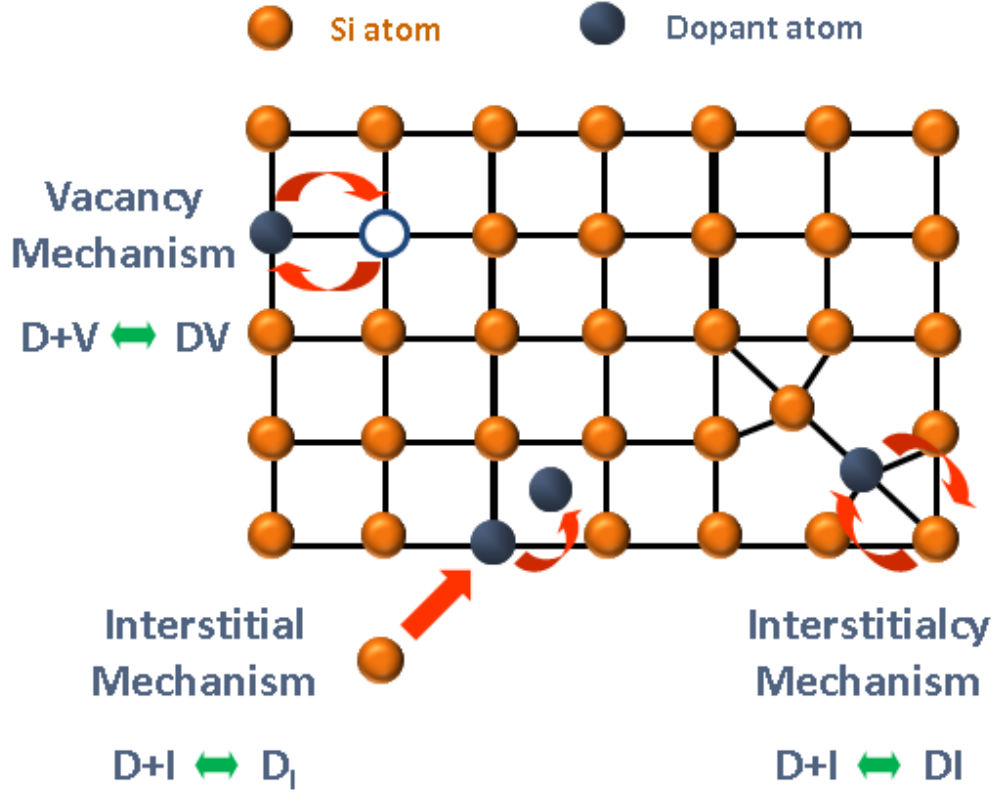
FIGURE 1.3: Schematic diagram for defect-mediated diffusion mechanism in silicon.

During high temperature annealing, there can be anomalous transient enhanced diffusion (TED), which is believed to be due to the rod-like {311} defects and dislocation loops which are responsible for the enhanced diffusivity, especially for boron-interstitial diffusion. The stability and density of {311} extended defects and dislocation loops also affect the point defect diffusion with their dissolution because they are the sources of free interstitials during high temperature annealing.

The point defect diffusion mechanisms can be identified as substitutional diffusion, vacancy diffusion, interstitial diffusion, interstitial-substitutional diffusion, and interstitialcy diffusion as shown in Fig. 1.3. For interstitialcy diffusion, interstitial atom kicks out substitutional dopant atom into interstitial site. These impurities can diffuse to

adjacent substitutional sites and create new self-interstitials. The interstitial position of the diffusing dopant atom is purely a transition state when the impurity moves from one substitutional site to other sites.

The physical properties should be investigated in order to understand the dopant diffusion behaviors in silicon: the implantation of energetic ions and damage production, the structure and activation energies of point defects, point defect interactions for cluster formation, the structure and activation energies of clusters, and the interactions between point defects and substitutional dopant atoms.

1.2.2 Density Functional Theory (DFT)

The structural and interaction properties of many solid-state and molecular systems have been investigated by the quantum-mechanical total energy calculations based on density functional theory (DFT) [7-10]. DFT minimizes the total energy by optimizing the electronic and nuclear coordinates in the system while it solves the charge density distribution instead of the quantum-mechanical many-body problem of electrons in the field of atomic nuclei [7-10].

In DFT, Born-Oppenheimer approximation is applied for simplifying the complicated calculations of electron-ion interactions in the system while the movement of ions is treated adiabatically and electron-ion Coulomb interactions are considered [11]. The Kohn-Sham equations are described below [8]:

$$\left[\frac{-\hbar^2}{2m}\nabla^2 + V_{ion}(\vec{r}) + V_H(\vec{r}) + V_{XC}(\vec{r})\right]\psi_i(\vec{r}) = \varepsilon_i\psi_i(\vec{r}),$$

where $\frac{-\hbar^2}{2m}\nabla^2$ is the kinetic energy term, $V_{ion}(\vec{r})$ is the electron-ion interaction term, $V_H(\vec{r})$ is Hartree electron potential term, $V_{XC}(\vec{r})$ is exchange-correlation potential term, $\psi_i(\vec{r})$ is electron wavefunction, and ε_i is Kohn-Sham eigenvalue.

The simplest approximation to exchange-correlation functional, $E_{XC}[n(r)]$, is the local-density approximation (LDA) [8], where the charge density at each point in space is independent of the density at other points. Generalized-gradient approximation (GGA) [12, 13] where $E_{XC}[n(r)]$ is a function of the density and its gradient is considered to be more precise compared to LDA. The periodic cell approximation is also used in order to simplify the problems with a finite number of electrons moving in the periodic potential. Bloch's theorem allows expansion of the electronic wavefunctions for the k-points in the Brillouin zone with a series of plane waves. Based on the approximations, KS equation can be solved self-consistently for the ground-state calculations, as shown in Fig. 1.4.

Only valence electrons are considered for physical properties in the solid state system while core electrons are replaced with pseudopotentials. Special k-points sampling method by Monkhorst and Pack [14] can be used in order to reduce the number of k-points in Brillouin zone. Ultrasoft-pseudopotentials (US-PP) [15] can also be considered in the solid for more accurate representation of the electronic wavefunctions. Conjugate-gradient method is used to fully relax the structure until the residual forces on the atoms are minimized within the pre-defined conditions. In order to perform DFT calculations, Vienna Ab-initio Simulation Package (VASP), ab-initio quantum-mechanical molecular dynamics (MD) simulator, is used to evaluate instantaneous electronic ground state [16].

trial charge ρ_{in} and trial-wavevectors ϕ_n

Hartree- and XC-potential and d.c.

Set up Hamiltonian

Subspace-diagonalization $\phi_{n'} \leftarrow U_{n'n}\phi_n$

Iterative diagonalization, optimize ϕ_n

Subspace-diagonalization $\phi_{n'} \leftarrow U_{n'n}\phi_n$

New partial occupancies f_n

New (free) energy $E = \Sigma_n \varepsilon_n f_n$ - d.c. - σS

New charge density $\rho_{out}(r) = \Sigma_n f_n |\phi_n(r)|$

Mixing of charge density $\rho_{in}, \rho_{out} \rightarrow$ new ρ_{in}

no

$\Delta E < E_{break}$
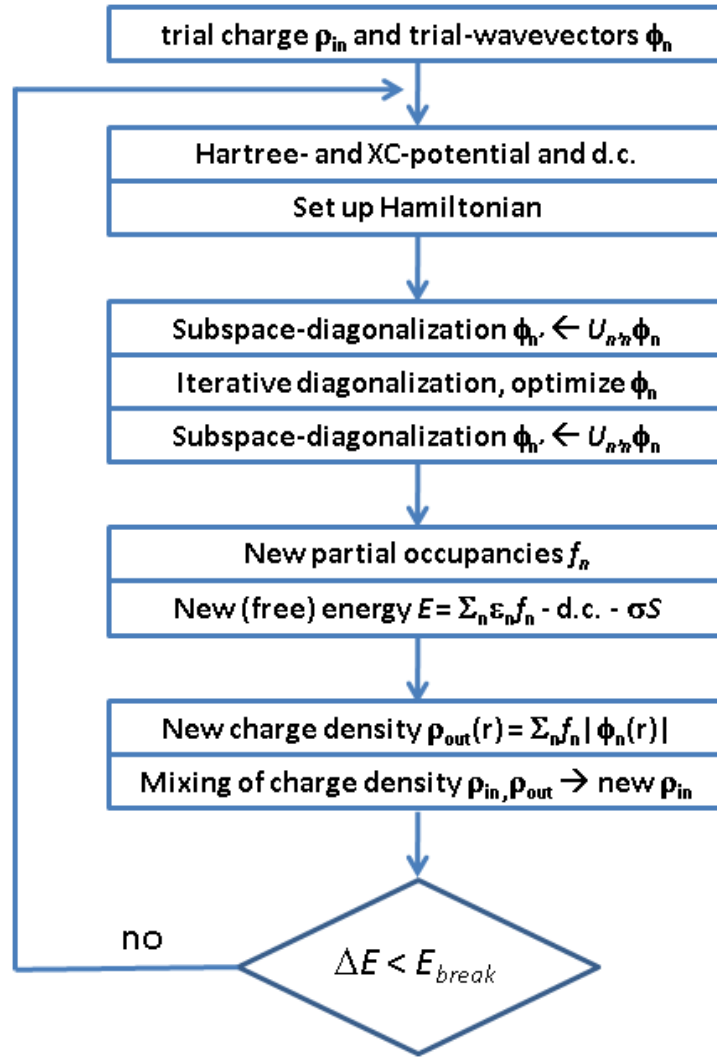
FIGURE 1.4: Self-consistent calculation of KS ground state [16].

7

1.3 Ultra Shallow Junction and Dopant Activation in CMOS

ITRS 2007 points out that the difficult challenges for doping technology for CMOS transistors are to achieve ultra-shallow doping profiles in source/drain extension regions, as shown in Fig. 1.5. One must attain progressively shallower junction depth needed to control short channel effects, as shown in Table 1.1 while optimizing the sheet resistance, doping abruptness at the extension-channel junction, and extension-gate overlap [1]. In other words, the doping processes for source/drain extension, channel, halo, and channel edges should be optimized in order to minimize the short channel effects in planar bulk CMOS transistors.

TABLE 1.1: Junction depth scaling in the S/D extension of CMOS [1].

Year	2007	2008	2009	2010	2011	2012
X_j	12.5 nm	11.0 nm	10.0 nm	9.0 nm	8.0 nm	7.0 nm

In Fig. 1.6, the as-implanted (vertical) junction depth should be minimized and TED during thermal annealing must be well controlled, while the sheet resistance is significantly reduced with high dopant activation. The lateral straggle during the vertical implantation strongly affects the lateral diffusion and overlap into the channel region [1]. Therefore, the short channel effects are strongly influenced by the vertical junction depth while the extension resistance is significantly affected by the dopant activation and lateral abruptness.
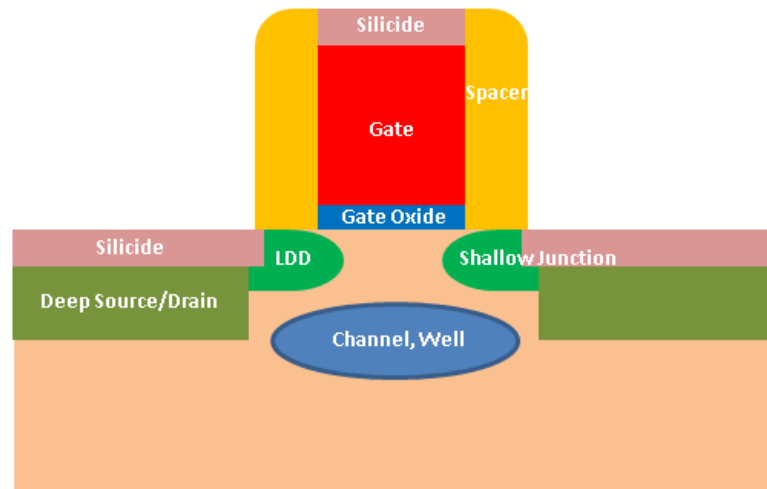
FIGURE 1.5: Schematic diagram of planar MOSFET.
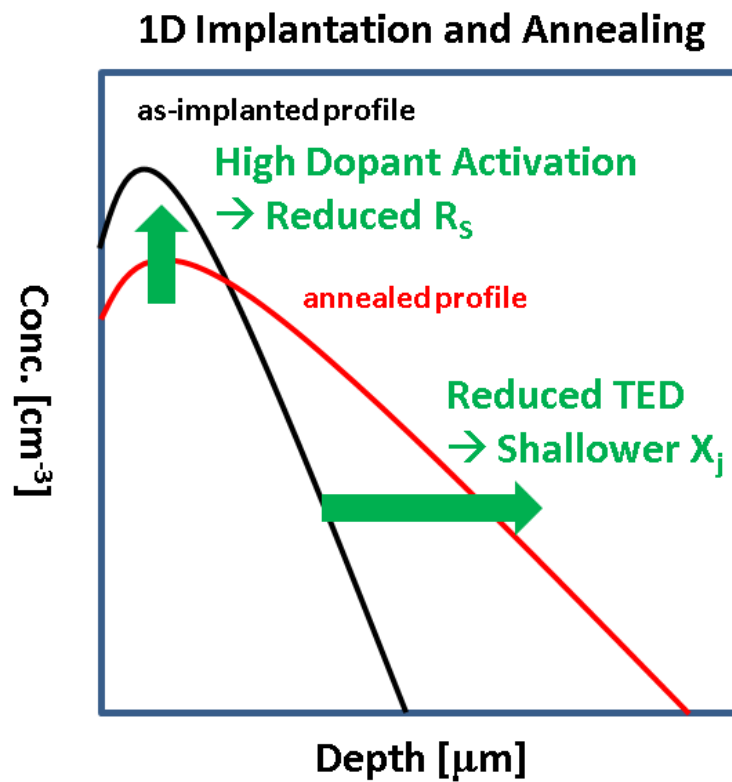
FIGURE 1.6: Illustration of 1D implantation and annealing in S/D extension of MOSFET.

A more abrupt, box-like shaped, lateral junction is conventionally assumed to have better performance in short channel devices because there is less overlap of extension doping in the channel region and then less counter doping schemes such as a halo implant are required [17, 18]. Charge sharing effects due to box-like shaped junctions can significantly degrade short channel effects such as threshold voltage roll-off and DIBL [17, 18]. Consequently there exists a trade-off for junction abruptness for optimum device performance, while maintaining the low series resistance.

1.4 OUTLINE

In the following chapters, atomic-scale modeling and experimental studies for dopant and defects in Si and Si_xGe_{1-x} nano-scale CMOS devices are investigated. In chapter 2, arsenic-interstitial clusters in silicon are discussed based on DFT calculations. In chapter 3, interstitial-mediated arsenic diffusion in strained silicon is discussed to order to investigate the strain properties and their effects on As diffusion. In chapter 4, boron diffusion retardation in $Si_{1-x}Ge_x$ is discussed based on how Ge affects the defect stability and migration barriers based on DFT calculations. In chapter 5, the role of boron transient enhanced diffusion and series resistance in high-k/metal gate $Si_{1-x}Ge_x$ pMOSFET are discussed. In chapter 6, the analysis for performance degradation factors is performed in $Si_{1-x}Ge_x$ and Ge nMOSFETs with TCAD simulations and electrical characterization. In chapter 7, the conclusion is discussed.

1.5 REFERENCE

[1] International Technology Roadmap for Semiconductors: 2007 Edition.
[2] J. Kong, IEEE Trans. VLSI Systems, 12, 1132 (2004).

[3] M.D. Giles, J. Electrochem. Soc., 138, 1160 (1991).

[4] M. Jaraiz, G.H. Gilmer, J.M. Poate, and T.D. de la Rubia, Appl. Phys. Lett., 68, 409, (1996).

[5] J.D. Plummer, M.D. Deal, and P.B. Griffin, Silicon VLSI Technology: Fundamentals, Practice, and Modeling, Prentice Hall, 2000.

[6] A. C. King, A. F. Gutierrez, A. F. Saavedra, J. Appl. Phys., 93, 2449 (2003).

[7] P.Hohenberg and W.Kohn. Phys. Rev., 136:B864 (1964).

[8] W. Kohn and L.J. Sham. Phys. Rev., 140:A1133 (1965).

[9] M. C. Payne et al. Rev. Mod. Phys., 64:1045 (1994).

[10] N. Argaman et al. Am. J. Phys., 68:69 (2000).

[11] A. L. Fetter, and J. D. Walecka, "Quantum Theory of Many-Particle Systems" McGraw-Hill, New York, p.29, 1971.

[12] J. P. Perdew, K. Burke, and M. Ernzerhof. Phys. Rev. Lett., 77:3865 (1996).

[13] G. Kresse and J. Hafner. J. Phys.: Condens. Matter, 6:8245 (1994).

[14] H.J. Monkhorst and J.D. Pack. Phys. Rev. B, 13:5188, 1976.

[15] D. Vanderbilt. Phys. Rev. B, 32:8412, 1985.

[16] http://cms.mpi.univie.ac.at/vasp/, VASP the GUIDE

[17] S. Kim, C. Park, and J. Woo, IEEE Trans. Electron Devices, 49, 457 (2002).

[18] S. Kim, C. Park, and J. Woo, IEEE Trans. Electron Devices, 49, 467 (2002).

CHAPTER 2: ARSENIC-INTERSTITIAL CLUSTERS IN SILICON

2.1 INTRODUCTION

Aggressive complementary metal oxide semiconductor field effect transistors (MOSFETs) scaling requires both ultrashallow junctions and low sheet resistance to overcome short channel effects and enhance the device performance in MOSFETs [1]. It is predicted by the International Technology Roadmap for Semiconductors (ITRS) that ultrashallow junctions less than 5 nm in depth will be necessary to produce the next generation of silicon transistors [1]. In order to achieve these challenging goals, the n-type dopant As is a desirable candidate due to its high mass, high solubility, low diffusivity and high activation. However, As also exhibits electrical deactivation and transient enhanced diffusion (TED) during post-implantation thermal annealing [2-7].

Earlier experimental and theoretical studies have shown that As TED can be mainly explained by vacancy-mediated As diffusion [5-7] and As deactivation might be driven by As_nV_m complexes [8-11]. However, Kong et al. and others have reported that interstitial-mediated As diffusion is dominant for As TED under supersaturated interstitial conditions [4, 12]. In the presence of excess Si interstitials, it is predicted that As_nV_m complexes are easily annihilated by $I-V$ recombination [13]. Hence, from the recent experimental results, it is clear that I-mediated As diffusion can be very important, together with V-mediated As diffusion [2-4]. In addition, previous experimental results have shown that As doping affects the size and density of Si {311} extended defects by trapping Si interstitials, suggesting that stable As_nI_m complexes are present at intermediate steps of anneal [14].

In presence of excess Si interstitials introduced during ion-implantation, I_2 and I_3 clusters can exist in large numbers and be highly mobile under non-equilibrium

conditions [15-17], implying a significant contribution to As TED and I_n cluster formation [2-7]. Likewise, one can expect that small As_nI_m complexes have an important important role in As TED and larger As_nI_m cluster formation, especially under Si interstitial supersaturation and high As concentrations. Harrison et al. have reported a possible formation and binding energy map of small As_nI_m complexes [18]. However, little is known about the detailed structure, stability, and dynamics of the complexes.

We present first-principles studies for the structure and dynamics of small As_nI_m complexes (AsI_2, As_2I_2, AsI_3, and As_2I_3) in crystalline Si. Using density functional theory calculations, we determine the ground state structures and the minimum energy diffusion pathways/barriers of small As_nI_m complexes, elucidating their relative roles in As TED and clustering.

2.2 COMPUTATIONAL DETAILS

All of our atomic and electronic structure calculations based on density functional theory (DFT) were done using plane wave basis ultrasoft pseuodopotential (USPP) method with the Vienna Ab-initio Simulation Package (VASP) [19-21]. The exchange-correlation energy functional is represented using the generalized gradient approximation (GGA) form of Perdew and Wang (PW91) [22]. Total energy calculations were performed on a 2×2×2 Monkhorst-Pack grid of k-points in the simple cubic cell [23]. The optimized Si lattice constant for our system is 5.457 Å. We used a cutoff energy of 200 eV for the plane-wave basis-set. A 216-atom supercell was found to sufficiently reduce system size errors in the total energy. All atoms were fully relaxed using the conjugate gradient method to minimize the total energy.

To test convergence with respect to k-points sampling and energy cutoff, we perform calculations with a 4×4×4 k-point grid and a 300 eV energy cutoff and find that our calculated formation energies vary by less than 0.2 eV, and our energy barriers by less than 0.03 eV. Local density of states (LDOS) are calculated in order to analyze defect characteristics such as the presence of gap states, their location with respect to the Fermi energy (E_F), and the presence of resonance states in the conduction band. LDOS calculations are done with a 3×3×3 k-point sampling of Brillouin zone. LDOS for different supercells are aligned using deep 2s levels of bulk Si atoms, distant from the defect structure. We calculate diffusion pathways and barriers using the nudged elastic band method [24]. To analyze the electronic structure and characterize bonding properties of stable $As_n I_m$ complexes as well as saddle points for diffusion pathways, we performed a Bader analysis [25] where the atomic volumes are defined solely from the electronic charge density. For this analysis, core charges are included within the projector augmented (PAW) framework, and the resolution of the charge density grid is increased, to give Bader charges with high accuracy. We calculated an electron localization function (ELF) iso-surface at the value of 0.80 [26]. In order to calculate the formation energy in different charged states, we applied a monopole charge correction of 0.11 eV in our 216 atom supercell, to compensate for the artificial uniform background countercharge required to maintain charge neutrality [27]. We used the experimental Si band gap of 1.2 eV to evaluate the chemical potential of electrons since DFT underestimates the gap [27].
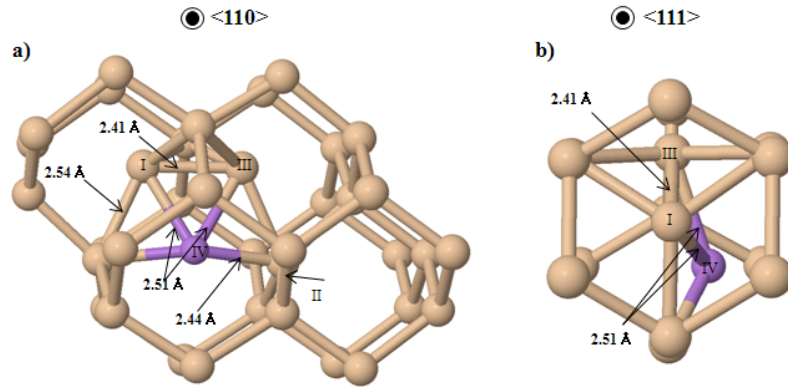
FIGURE 2.1: The ground state structure of AsI_2 viewed from the <110> and <111> directions. Yellow (light) and purple (dark) represent Si and As atoms, respectively.

2.3 DI-INTERSTITIALS WITH ONE ARSENIC ATOM (AsI_2)

We first investigated the lowest energy structure of the neutral di-interstitial with one As atom (AsI_2) and its diffusion pathway in crystalline Si. Several theoretical studies have shown that Si di-interstitials (I_2) are fast-diffusing species with a low migration barrier [15, 17]. In analogy to the Si di-interstitial, AsI_2 is also expected to be highly mobile. The lowest energy configuration identified is shown in Fig. 2.1 [15]. While I_2 has equilateral triangular shape as the ground state, the overall triangular shape of AsI_2 is slightly distorted with the addition of an As atom to the structure. As a result, the Si-Si (I-III) bond length is 2.41 Å and the As-Si (I-IV) bond length is 2.51 Å in the relaxed structure.
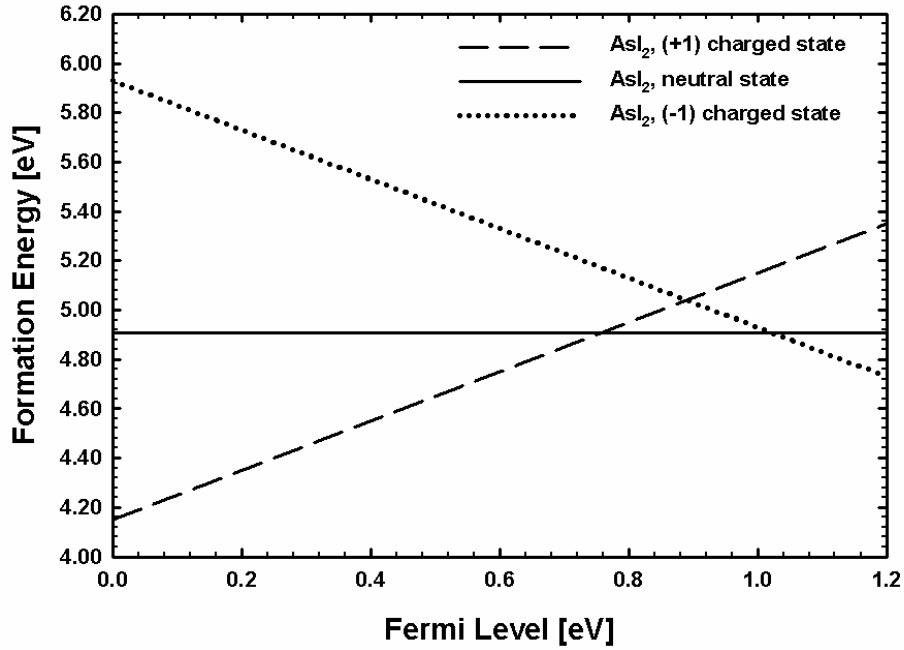
FIGURE 2.2: Formation energy as a function of Fermi level for the minimum energy configuration of AsI_2.

We assessed the stability of neutral AsI_2 in crystalline Si by its relative formation energy [28]. The formation energy in the neutral state is 4.91 eV for the relaxed configuration shown in Fig. 2.1. In Fig. 2.2, the formation energy is calculated as a function of Fermi level, which shows that neutral and negatively charged AsI_2 are stable in lightly and heavily n-doped regions in Si, respectively. The binding energy of AsI_2 is estimated to be 0.56 eV with reference to the dissociation products of neutral I_2 and substitutional As by $E_b(AsI_2) = E_f(I_2) + E_f(As) - E_f(AsI_2)$. We also calculate the binding energy with reference to the dissociation products of neutral AsI and split-<110> interstitial (I) and find it to be 1.88 eV by $E_b(AsI_2) = E_f(AsI) + E_f(I) - E_f(AsI_2)$. Although the '$I_2$ and As dissociation' route is more favorable than the 'AsI and I dissociation' route, the most probable result of AsI_2 dissociation is expected to be I and

16

and AsI in the Si lattice because both I and AsI are highly mobile. It should be noted that it is challenging to identify a complete dissociation dynamics for given arsenic-interstitial clusters. For example, the dissociation for AsI_2 pair can be the combinatorial constituents of I and AsI. In the arguments for AsI_2 dissociation, we would like to show show two possible dissociated pairs while the binding energies for two cases are shown. Although I_2 $(+As)$ itself is known to be fast diffusers, $I + AsI$ seems to be more likely due to their higher concentrations and configurational entropy effect.

In order to characterize the bonding of stable AsI_2, we calculated the LDOS for the As atom in the cluster structure and compared it with that of substitutional As. Figs. 3(a) and 3(b) show the band-gap portion of the LDOS for an As atom in a substitutional position and in the cluster, respectively. The LDOS in Fig. 2.3(b) has a high intensity peak close to the valence band edge, corresponding to a lone electron pair from the ELF. Bader analysis, summarized in Table 2.1, shows 5.6 valence electrons for stable AsI_2 in the neutral state when a substitutional As has 5.7 valence electrons. No significant charge transfer to As is found in the positively and negatively charged states of AsI_2 as compared to the neutral state.
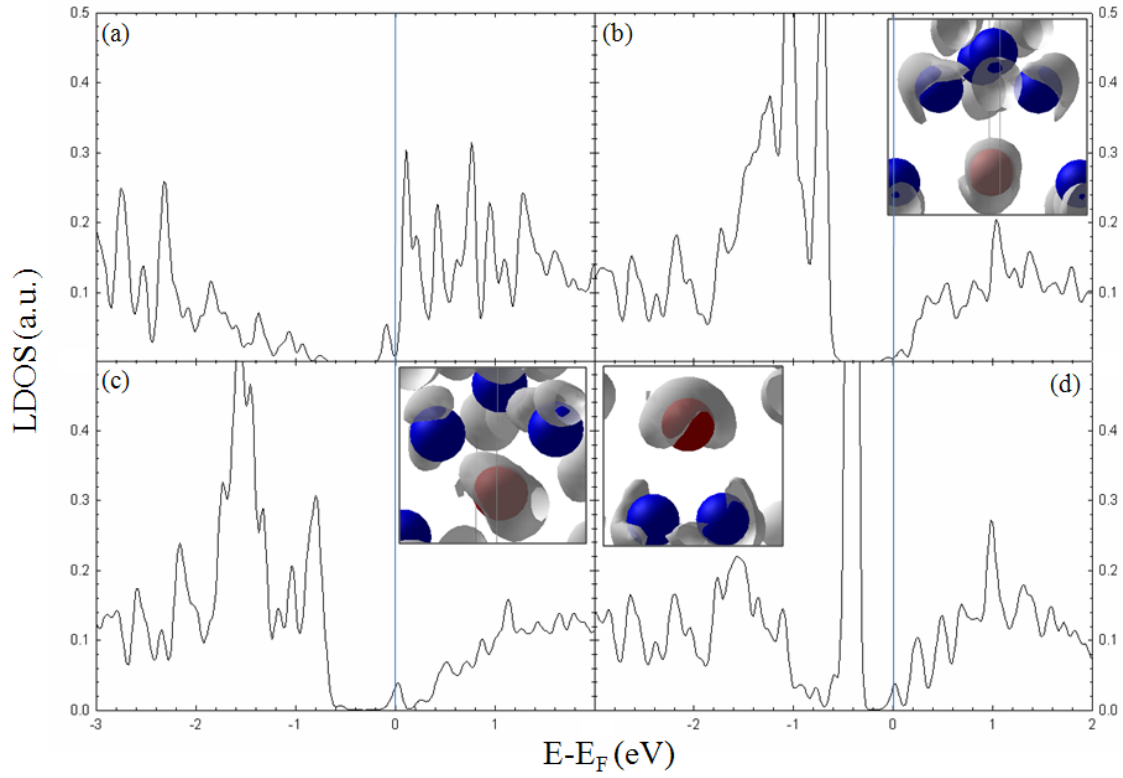
FIGURE 2.3: Local density of states (LDOS) of (a) substitutional As (red color) in crystalline Si. LDOS for interstitial As (red color) in (b) global minimum of AsI_2 in Fig. 2.1. LDOS for interstitial As (red color) in transition states of AsI_2: (c) 'T$_{AB}$' and (d) 'T$_{BC}$' shown in Fig. 2.4. The zero in horizontal axis (E-E$_F$) corresponds to the calculated Fermi level associated with the structure. The corresponding decomposed electron densities are displayed in the inset with the ELF isosurface with a value of 0.80. Blue and red represent Si and As atoms, respectively.

18
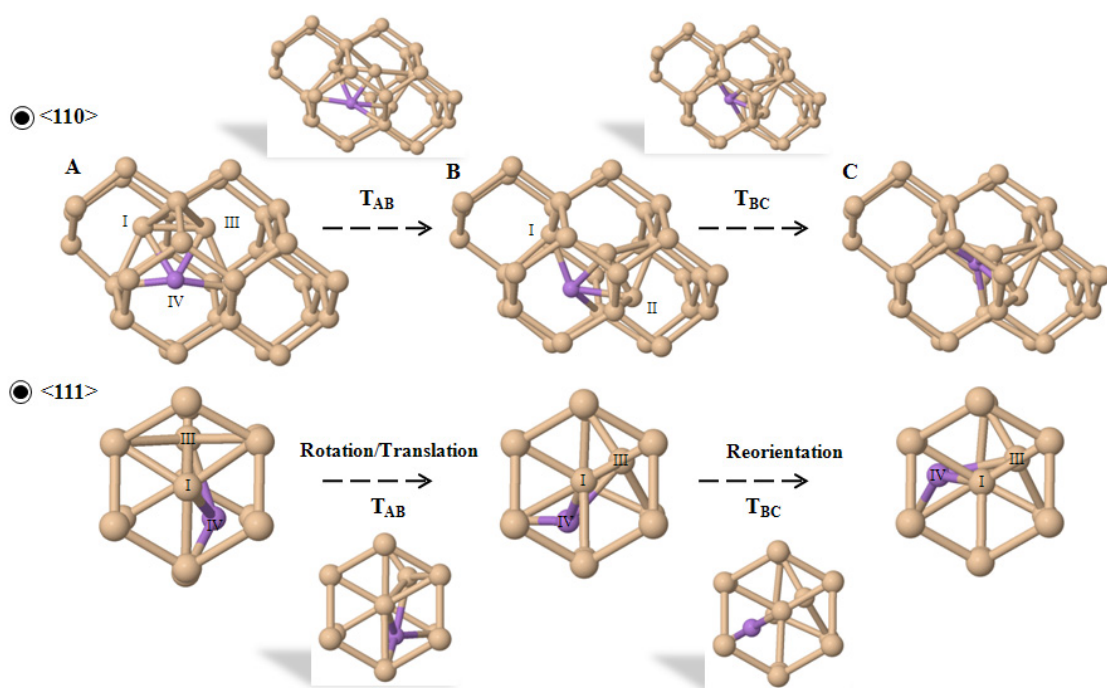
FIGURE 2.4: AsI_2 diffusion pathway in crystalline Si. The As atom is labeled as IV, while its neighboring Si atoms are labeled as I, II, and II. Yellow (light) and purple (dark) represent Si and As atoms, respectively.

TABLE 2.1: Number of valence electrons obtained from Bader decomposed charge analysis on As interstitial atom of AsI_2 and As_2I_2 in the neutral state. If (-1) and (+1) are specified, they are representing negatively and positively charged state, respectively.

	Number of Valence Electrons	
	As Substitutional	
As	5.7	
	As Interstitial	
AsI_2-'A'	5.6 [5.6 (-1), 5.6(+1)]	
AsI_2-'T$_{AB}$'	6.2	
AsI_2-'T$_{BC}$'	5.6	
	As(I)	*As(II)*
As_2I_2-'A'	5.8 [5.8 (-1), 5.7(+1)]	5.9 [5.9(-1), 5.8(+1)]
As_2I_2-'B'	5.4	5.4
As_2I_2-'C'	5.4	5.4

Next we propose a diffusion pathway for AsI_2 that occurs through three local minima, labeled as 'A', 'B', and 'C', in Fig. 2.4. Du et al. [15] suggested a novel diffusion pathway of I_2 with a migration barrier of 0.30 eV, with a mechanism consisting consisting of a translation/rotation and then a reorientation step. The diffusion pathway of AsI_2 might follow a similar trajectory to I_2 because the structures of AsI_2 and I_2 are very similar. In Fig. 2.4, the ground state configuration 'A' is rotated roughly by 60 degree with respect to the axis connecting both *Si* (I) and *Si* (II) atoms in order to reach

reach another local minimum 'B'. At the transition state 'T$_{AB}$', the rotational and translational movement of both *Si* (III) and *As* (IV) atoms are made from one *Si* lattice site to another. The reorientation mechanism of the *As* atom is shown from 'B' to 'C' through the transition state 'T$_{BC}$'. The *As* (IV) atom is rotated roughly by 60 degree about about an axis connecting the *Si* (I) and *Si* (II) atoms, without affecting the atomic position of *Si* (III).
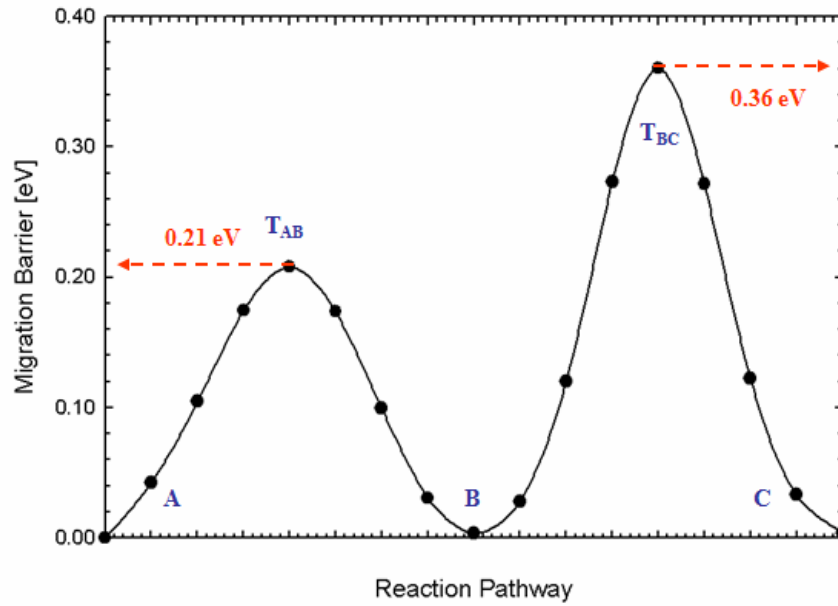
FIGURE 2.5: Migration barrier along the *AsI*$_2$ diffusion pathway, calculated with the nudged elastic band method.

The LDOS of the *As* atom in the saddle point structures reveals some interesting features of the diffusion pathway. Fig. 2.3(c) is from the saddle point of *AsI*$_2$ ('T$_{AB}$' in Fig. 2.4) and Fig. 2.3(d) is from the saddle point of *AsI*$_2$ ('T$_{BC}$' in Fig. 2.4). The *As* atom atom in Fig. 2.3(c) has 6.2 valence electrons at the saddle point. However, this increased charge state (see Table 2.1) does not lead to a substantial increase in the total energy. Upon migration from 'A' to 'B' (see Fig. 2.4), charge is locally relocated between the *As*

As and *Si* atoms in the 'T$_{AB}$' structure leading to formation of electron lone pair on *As* atom and increase of total energy. As shown in Fig. 2.3(d), the high peak in the band-gap contributes to increasing the total energy at the transition state 'T$_{BC}$'. Charge transfer at the transition state suggests that AsI_2 migration may start in neutral state, capture an electron, becoming $AsI_2^{\delta-}$ between 'A' and 'T$_{AB}$' points and lose the electron between 'T$_{AB}$' and 'B'. The viability of such recharging diffusion mechanism will depend on the position of Fermi level. The migration barrier of AsI_2 is shown in Fig. 2.5 for the translation/rotation and reorientation mechanism. The rotation/translation barrier from 'A' to 'B' is calculated to be 0.21 eV, and the reorientation barrier from 'B' into 'C' is 0.36 eV. Since AsI_2 has a low migration barrier, it is expected to be highly mobile and diffuse isotropically, similar to I_2.

2.4 DI-INTERSTITIALS WITH TWO ARSENIC ATOMS (As_2I_2)

We next investigated the structure of the neutral di-arsenic interstitial (As_2I_2) in crystalline *Si*. Starting with several stable configurations of I_2 [15, 29], an extensive search of energetically favorable configurations of As_2I_2 was done in order to identify the global minima. We assessed the stability of neutral As_2I_2 in *Si* by the relative formation energy [30]. Based on the structural configurations in Fig. 2.6, the formation energies for '(a)', '(b)', and '(c)' are given by 3.90 eV, 4.07 eV, and 4.15 eV in the neutral state, respectively. Our identified atomic structure of As_2I_2 in Fig. 2.6(a) is more energetically favorable by 0.52 eV in terms of formation energy, as compared to previous calculations [18]. In Fig. 2.7, the formation energy is calculated as a function of Fermi level, which shows that neutral As_2I_2 is stable in both lightly and heavily n-doped Si.
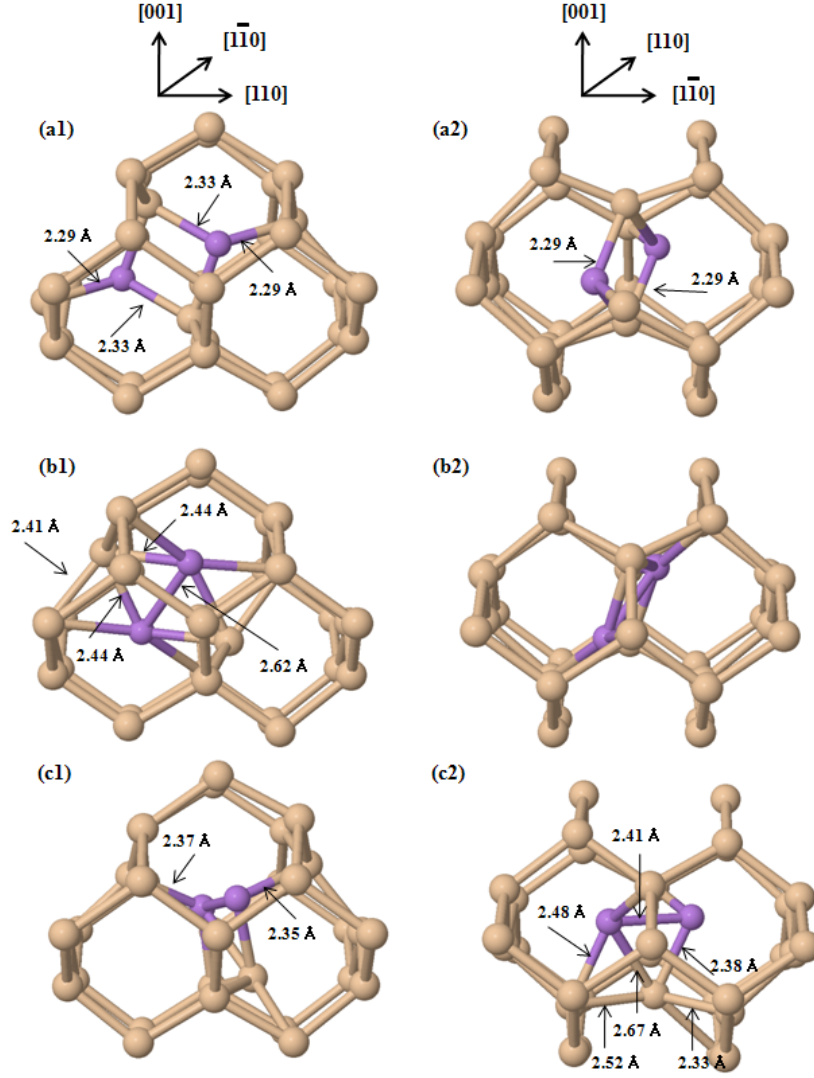
FIGURE 2.6: Atomic configurations of As_2I_2 in the <110> and <111> directions: (a1) the lowest energy configuration, (b1) and (c1) local minimum configuration. As is shown with purple (dark) atom and Si is shown with yellow (light) atom.
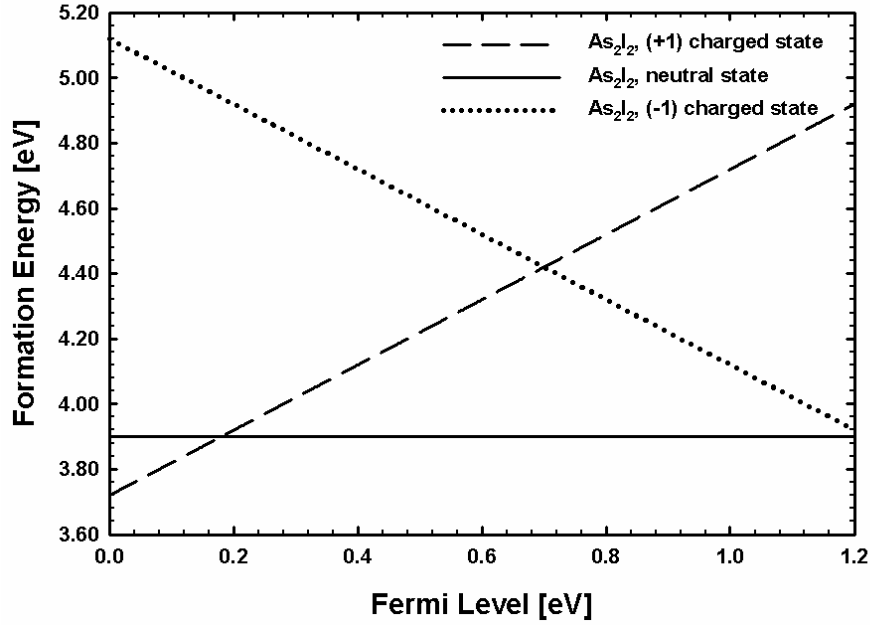
FIGURE 2.7: Formation energy as a function of Fermi level for minimum energy configuration of As_2I_2. The experimental band gap for Si is 1.2 eV.

Consideration of the two local minima ('(b)' and '(c)' in Fig. 2.6) helps us identify the relative roles of chemical bonding and symmetry for the stabilization of As_2I_2 structures. Starting with the global minimum configuration 'Fig. 2.6(a)', we can clearly observe that the most stable structure is highly symmetric and well-bonded. A possible reason for the stabilization is that both the *Si* and *As* atoms in the global minimum have formed highly symmetric, sp³-like bond configurations. The sp³-like hybridization is supported by the fact that the sum of bond angles between the *As* atom and its three neighboring *Si* atoms is 324.3°, close to the sum of angles (3×109°=327°). As is evident from the absence of sharp peaks near or in the band gap in Fig 8 (b), this pair is fully involved in bonding with neighboring atoms.
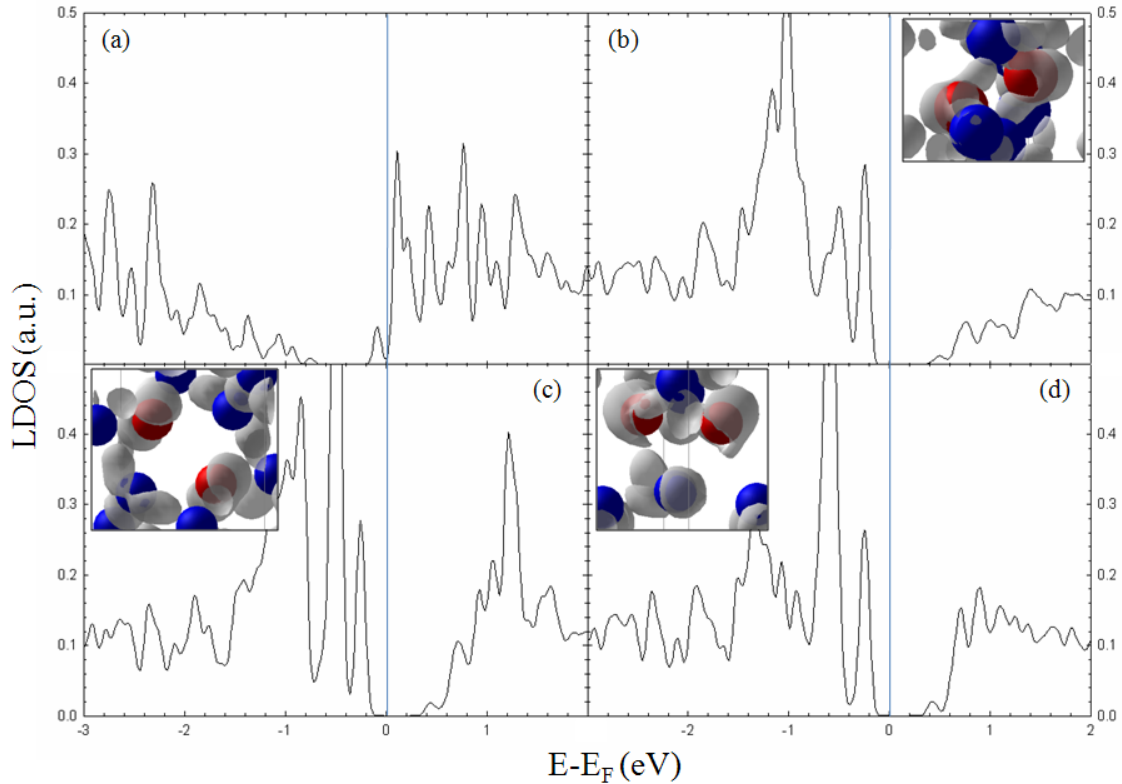
FIGURE 2.8: Local density of states (LDOS) of (a) substitutional As in crystalline Si. LDOS (As_2I_2) of (b) 'Fig. 2.6(a)', (c) 'Fig. 2.6(b)', and (d) 'Fig. 2.6(c)'. The zero in horizontal axis (E-E$_F$) corresponds to the calculated Fermi level associated with the structure. The corresponding decomposed electron densities are displayed in the inset with the ELF isosurface with a value of 0.80. Blue (dark) and Red (light) represent Si and As atoms, respectively.

Next, we consider the local minimum As_2I_2 configurations of '(b)' and '(c)' in Fig. 2.6. The bonding of the Si atoms in 'Fig. 2.6(b)' preserves sp^3-like hybridization, while that of the As atoms starts to deviate from it, resulting in a sharp peak in the LDOS LDOS close to the valence band, with corresponding anti-bonding resonance level in the conduction band, and a total energy increase of 0.17 eV. In the local minimum structure 'Fig. 2.6(c)', which is next highest in energy to structure 'Fig 6(b)', the symmetric bonding is lost for both Si and As atoms, increasing the occupation of non-bonded

states, and the total energy to 0.25 eV above the global minimum structure 'Fig. 2.6(a)'. From the Bader analysis in Table 2.1, the As atoms in the two configurations in 'Fig. 2.6(b)' and 'Fig. 2.6(c)' are locally donating their valence electrons into the neighboring Si atoms.

For the sake of completeness, we estimate the binding energy of the neutral As_2I_2. The ground state 'Fig. 2.6(a)' binding is estimated to be 1.90 eV with respect to the dissociation products of neutral As_2I and I by $E_b(As_2I_2) = E_f(As_2I) + E_f(I) - E_f(As_2I_2)$. We also calculate the binding energy of As_2I_2 with reference to two neutral AsI and find it to be 2.19 eV by $E_b(As_2I_2) = E_f(AsI) + E_f(AsI) - E_f(As_2I_2)$. With the assumption that the dissociation rate of As_2I_2 is highly dependent on both the mobility of the leaving species and the binding energy, dissociation products of two neutral AsI are expected since AsI is highly mobile. In addition, there are four degenerate states (Fig. 2.6(c)), which participate in the reorientation mechanism shown in Fig 9. With an energy barrier of 0.32 eV, As_2I_2 can translate among these four degenerate configurations.

We propose a diffusion pathway for As_2I_2 that occurs through three local minima, labeled as 'A (Fig. 2.6(a))', 'B (Fig. 2.6(b))', and 'C (Fig. 2.6(c))', in Fig. 2.10. The lowest energy structure of As_2I_2 is given by 'A' (and the equivalent 'A†'). In order to reach the first transition state 'T$_{AB}$' from the ground state configuration 'A', $As(I)$ and $As(II)$, which are closely aligned along [110], are slightly rotated around the axis connecting the two As atoms.
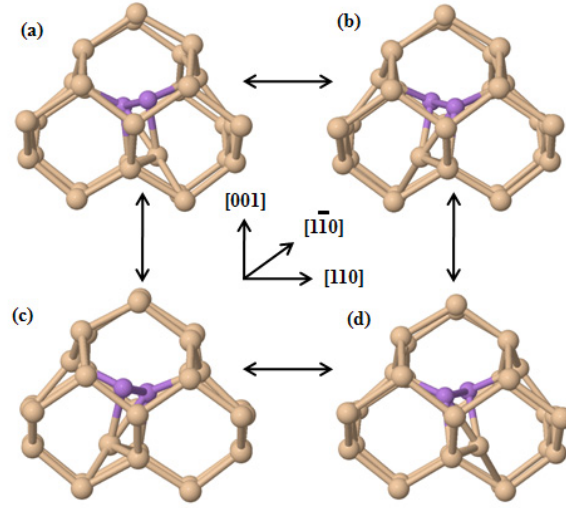
FIGURE 2.9: Reorientation mechanism of As_2I_2 within a lattice site. All four configurations are degenerate in total energy. As is depicted with purple (dark) atom and Si is shown with yellow (light) atom.
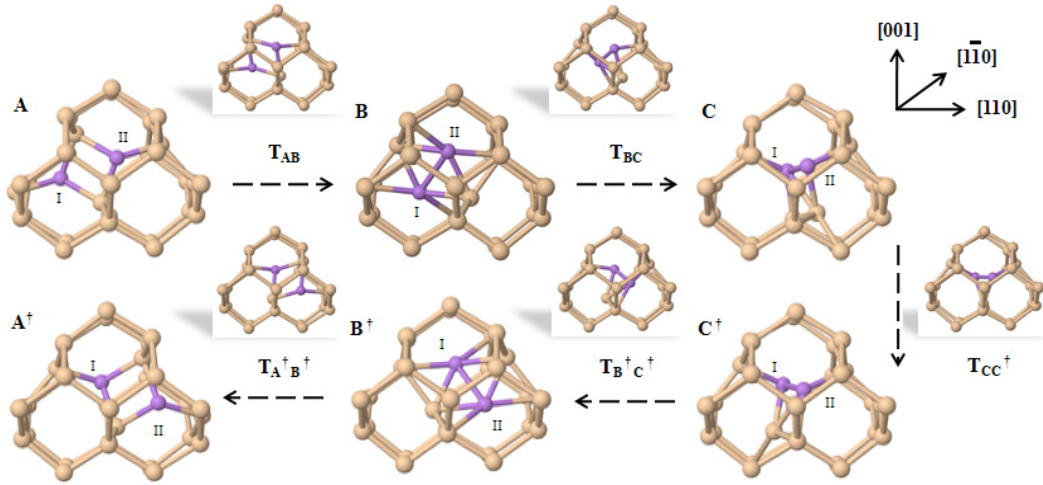
FIGURE 2.10: As_2I_2 diffusion pathway in crystalline Si. 'A' is the ground state while 'B' and 'C' are the local minimum states. Transition states are also shown. The two As atoms are labeled as I and II.

Rotation and translation of the two *As* atoms results in a reduction of the distance between them, from 3.18 Å to 2.62 Å. The final state of this process is the next local minimum 'B' in Fig. 2.10.

To reach the second transition state 'T_{BC}' from the local minimum B, one of two *Si* atoms that are bonded together with two *As* atoms, is shifted into the <111> direction, allowing them to share the lattice site. During the transition of 'T_{BC}', *As* (I) and *As* (II) are rotated into the $[1\bar{1}0]$ direction to form a triangular shape with a *Si* atom in the direction of the displacement. With a transformation into 'B', two *As* atoms are rotated by almost 90 degrees with respect to original ground state position 'A', aligning them in the $[1\bar{1}0]$ direction. In the local minimum 'B', the bond distance of *As* (I) and *As* (II) is 2.41 Å, which is smaller than for any other configuration.

In local minimum 'C', there are four degenerate states as depicted in Fig. 2.9. In order to reach one of these degenerate states, '$C^{\dagger}$', the *Si* atom just below two *As* atoms is required to be shifted into the opposite [110] direction with a slight translational movement of these atoms. Next, *As* (I) and *As* (II) diffuse through '$T^{B\dagger C\dagger}$' (equivalent to 'T^{BC}') to reach the local minimum '$B^{\dagger}$' (equivalent to 'B'). Then they migrate through '$T^{A\dagger B\dagger}$' (equivalent to 'T^{AB}') to get to the global minimum '$A^{\dagger}$'.

The diffusion mechanism of As_2I_2 is identified with translation and rotation in their structures with a migration barrier, as shown in Fig. 2.11. The initial barrier from 'A' to 'B' configurations is calculated as 1.03 eV. The barrier from 'B' to 'C' is 0.42 eV. Then, reorientation occurs with a migration barrier of 0.32 eV. Although the local minimum 'B' has a slightly higher relative energy by 0.16 eV than the ground state 'A', the partial diffusion pathway can be composed of "B" ("$B^{\dagger}$") and "C" ("$C^{\dagger}$") with low energy barrier of 0.42 eV.

28
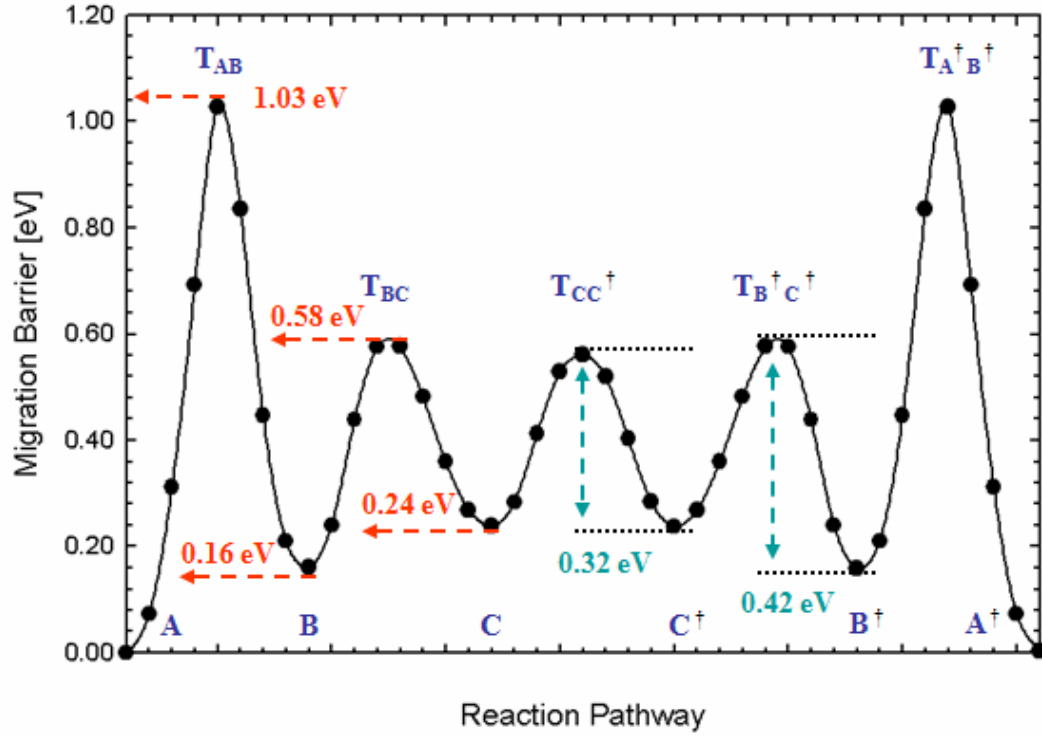
FIGURE 2.11: Migration barrier along the As_2I_2 diffusion pathway in crystalline Si.

2.5 TRI-INTERSTITIALS WITH ONE AND TWO ARSENIC ATOMS

We obtained structural configurations and formation energies for AsI_3 and As_2I_3 clusters. Fig. 2.12 shows that the lowest energy configuration for neutral compact type tri-interstitials with one As atom (AsI_3^c) in crystalline Si [16, 31]. The ground state AsI_3^c AsI_3^c in Fig. 2.12(a) has a bond length of 2.37 Å and 2.43 Å for the Si-Si (III-IV) and As As-Si (III-V) bonds, respectively. The transition state of AsI_3^c, shown in Fig. 2.12(b), has has a similar configuration to I_3^c; with comparable As-Si and Si-Si bond lengths of 2.56 and 2.51 Å respectively. We assessed the formation energy of AsI_3^c to be 6.71 eV in Fig. 2.12(a). The stable AsI_3^c structure is formed by displacing the two silicon atoms in the I_3^c cluster away from the base of equilateral triangle in <111> direction. The binding

29

energy of AsI_3^c is estimated to be 1.96 eV with respect to the dissociation products of neutral I and AsI_2 by $E_b(AsI_3^c) = E_f(I) + E_f(AsI_2) - E_f(AsI_3^c)$.
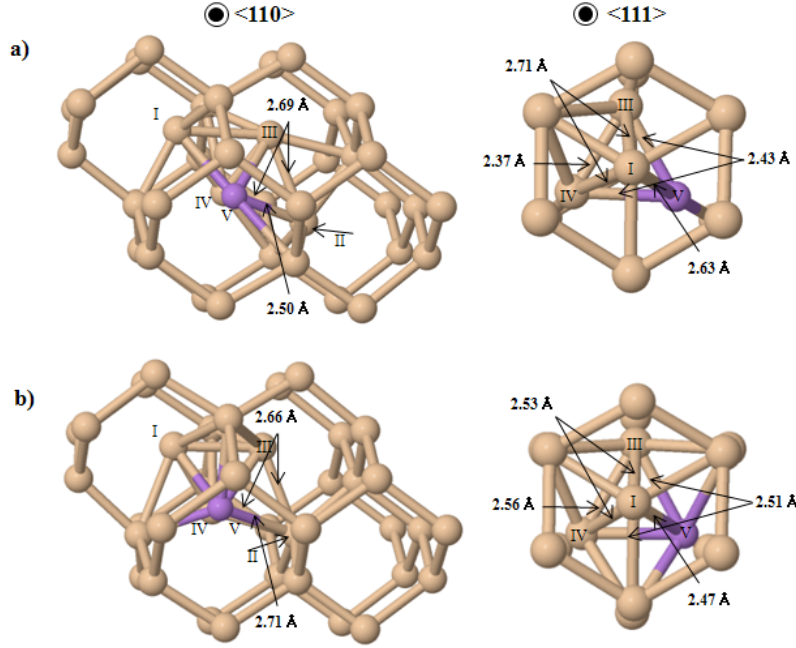
FIGURE 2.12: Atomic configurations and bond lengths of AsI_3^c in <110> and <111> direction: (a) the lowest energy configuration, (b) the transition state configuration. As is depicted with purple (dark) atom and Si is shown with yellow (light) atom.

When an As atom replaces one of the Si interstitial atoms in I_3^c it does not distort the bond configurations significantly, as shown in Fig. 2.12, and AsI_3^c exhibits a similar reorientation behavior as I_3^c, as shown in Fig. 2.13. We find that the rotation barrier for AsI_3^c is 0.39 eV while a reorientation barrier is just 0.10 eV (see Fig. 2.14). The 60 degree rotation of AsI_3^c occurs by a screw motion between two local minima which are labeled 'A' and 'B' in Fig. 2.13. The ground state 'A' and 'B' can move into a nearest neighbor lattice site by the transition state 'R_A' and 'R_B', respectively. However,

As (V) has limited space to reorient its position while maintaining the overall atomic configuration of AsI_3^c, which, unlike I_3^c, implies anisotropic diffusion. Hence our calculations show that the dynamics of compact AsI_3^c will be dominated by dissociation as well as reorientation of the cluster. Next, we consider an extended AsI_3^{ext} configuration. The lowest energy configuration of AsI_3^{ext} is found to have a formation energy of 6.00 eV, as shown in Fig. 2.15(a). The binding energy is calculated to be 2.67 eV with respect to the dissociation products of neutral I and AsI_2 by

$$E_b(AsI_3^{ext}) = E_f(I) + E_f(AsI_2) - E_f(AsI_3^{ext}).$$
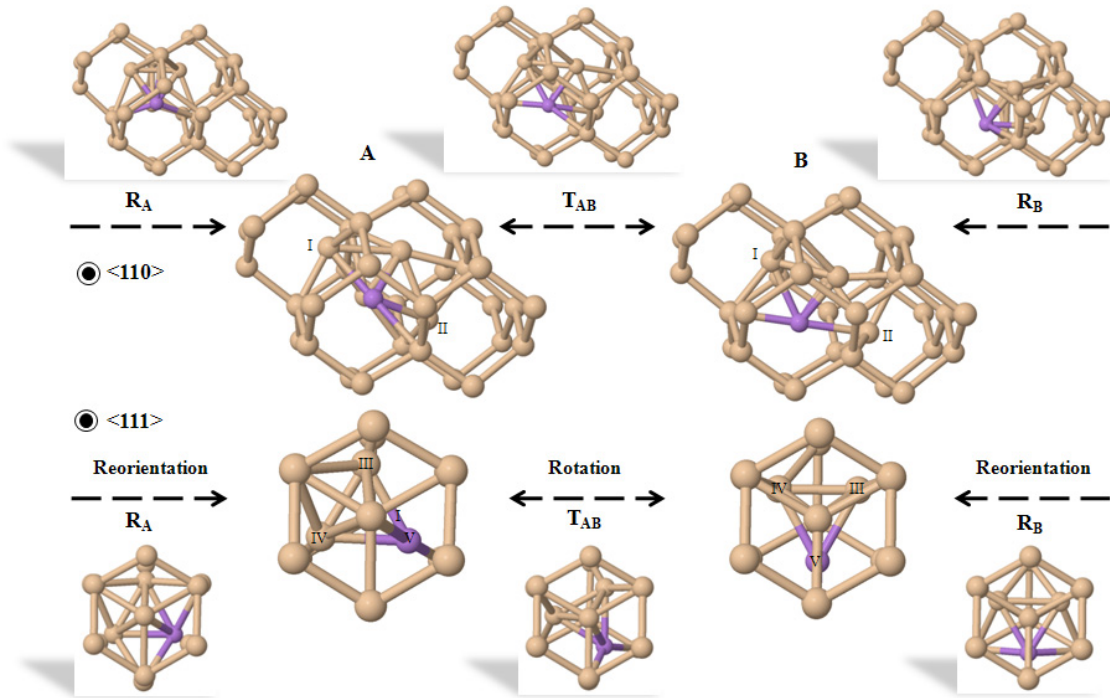
FIGURE 2.13: AsI_3^c diffusion pathway in crystalline Si. The local minimum structures ('A' and 'B') are shown with intermediate transition states.

31
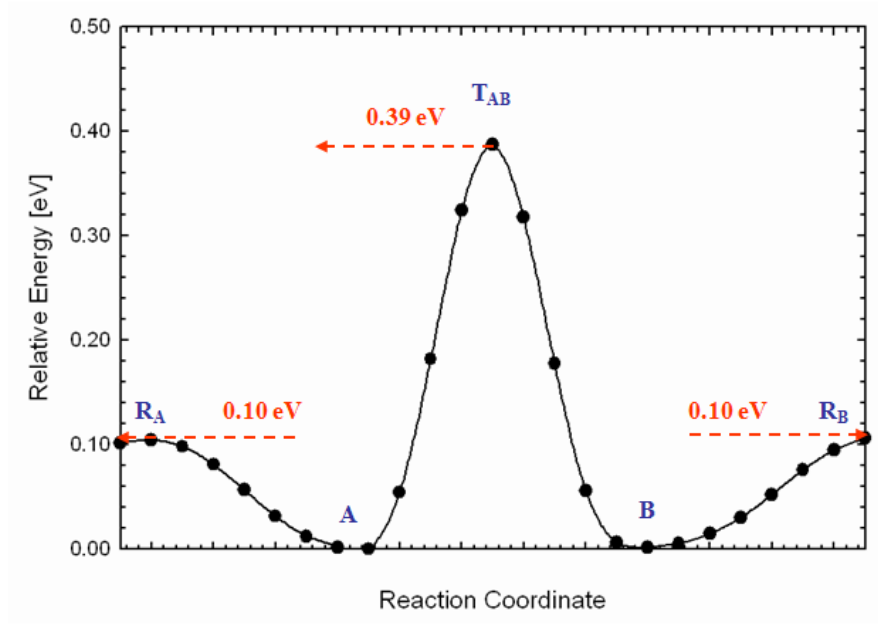
FIGURE 2.14: Migration barrier along with AsI_3^c diffusion pathway in crystalline Si.

Finally, we investigate the relative stability of tri-interstitials with two As atoms within both compact $(As_2I_3^c)$ and extended structures $(As_2I_3^{ext})$. The lowest energy configuration of $As_2I_3^c$ is shown in Fig. 2.16 with a formation energy of 5.95 eV. The binding energy of $As_2I_3^c$ is estimated at 2.05 eV with respect to the dissociation products of neutral AsI and AsI_2. The propensity of $As_2I_3^c$ to easily dissociate is explained by the relatively large distance of 2.98 Å between $As(V)$ and $As(VI)$.
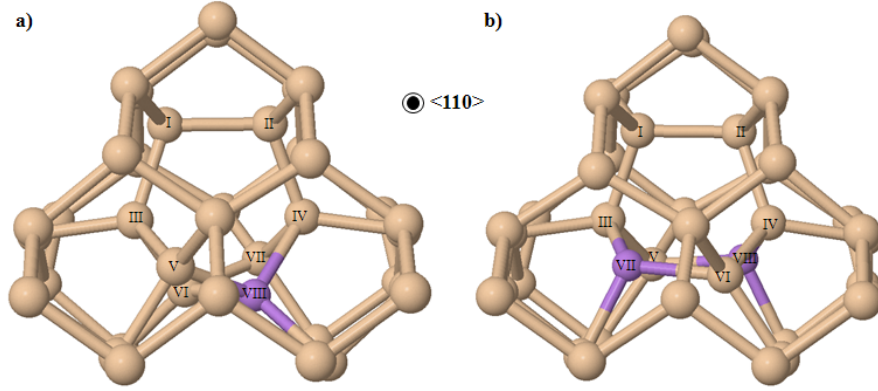
FIGURE 2.15: Lowest energy structure of (a) AsI_3^{ext} and (b) $As_2I_3^{ext}$. As is depicted as purple (dark) atom and Si is shown as yellow (light) atom.
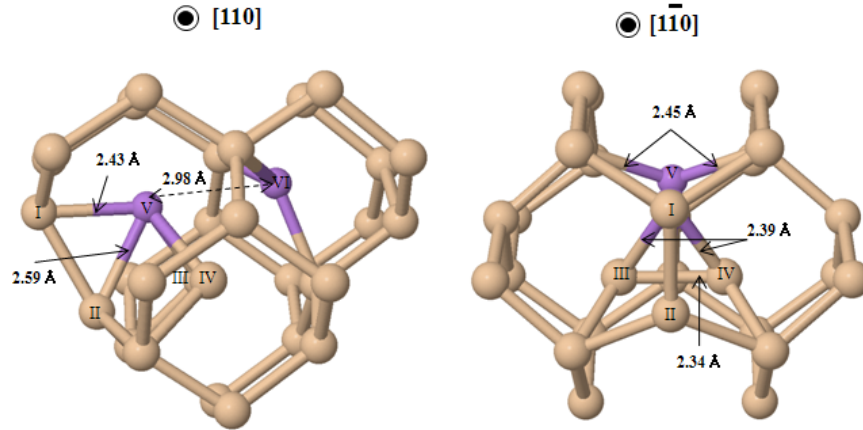
FIGURE 2.16: Lowest energy structure of $As_2I_3^c$. As is depicted as purple atom and Si is shown as yellow atom.

The lowest energy configuration of $As_2I_3^{ext}$ is shown in Fig. 2.15(b) with a formation energy of 5.36 eV. The binding energy of $As_2I_3^{ext}$ is estimated to be 2.64 eV with respect to the dissociation products of neutral AsI and AsI_2. The bond length between the As atom and the three neighboring Si atoms is 2.31 Å, which shows highly highly symmetric bonding characteristics. The As atoms and their neighboring Si atoms

33

atoms have a stable bonding geometry in $As_2I_3^{ext}$, which is similar to the extended type I_3^{ext}.

2.6 IMPLICATIONS ON INTERSTITIAL-MEDIATED ARSENIC DIFFUSION AND CLUSTERING

Harrison et al. have suggested the easy annihilation of arsenic-vacancy complexes due to interstitial-vacancy recombination in the presence of excess interstitials [13]. Depending on which defect is in excess, the relative role of interstitial- and vacancy-mediated diffusion in *As* TED can be determined [8]. Kong et al. suggested that interstitial-mediated *As* diffusion could be dominant with excess *Si* interstitials, controlling initial interstitial and vacancy concentrations [12]. Moreover, Brindos et al. have shown that the number and size of {311} extended defects is reduced as *As* doping concentration is increased, suggesting the existence of stable arsenic-interstitial complexes at $750\,^{\circ}C$ [14].

In order to investigate the implications of arsenic-interstitial complexes for *As* TED and clustering, ab initio density functional theory calculation results for formation, binding, and migration energy of arsenic-interstitial complexes are summarized in Table 2.2. Here, we have calculated the formation energy of each cluster with respect to three reference states; E_{f1} has a reference state of substitutional *As* atoms and a perfect *Si* lattice [32], E_{f2} has a reference state of substitutional *As* and *n* interstitial *Si* atoms in the *Si* lattice [33], and E_{f3} has a reference state of substitutional *As* and *n* interstitial *Si* *Si* atoms in the {311} extended defects whose formation energy per atom is approximately 2 eV [34, 35] . E_{f1} describes the energetic cost to form clusters from a perfect crystal – these energies are very high because of the high cost of forming interstitials. E_{f2} does not include the cost of forming the interstitials, which is appropriate appropriate in the limit where there is a high concentration of interstitials in the lattice. In

this limit, As_nI_m clusters are increasingly stable with cluster size. Since experimental conditions will lie somewhere between these two limits (E_{f1} and E_{f2}), E_{f3} considers the energetic cost of available interstitials from {311} extended defects which are formed by excess Si interstitials under non-equilibrium conditions during thermal annealing.

Even though As_nI_m clusters are energetically stable in the presence of excess interstitials, there is an entropic cost to forming these clusters. At high temperatures and low As and/or interstitial concentrations, entropy will favor smaller clusters. This configurational entropy can be estimated from the equilibrium concentration of Si free interstitials (C_I^*), taken to be $7.95 \times 10^{27} \exp(-4.002/kT)\, cm^{-3}$) [36]. Because the defect concentrations in Si after ion implantation are not explicitly known and they highly depend on implant process conditions, the equilibrium concentrations are assumed as an extreme case in order to demonstrate a configurational entropy effect in the clusters. Here, we are assuming that the As concentration is higher than that of the Si interstitials under the high As dose ($> 5 \times 10^{14}\, cm^{-2}$) conditions used for junction formation. Then, the configurational entropy (S) of bringing each additional interstitial into a cluster will be dominated by $k\ln(C_I^*/C_{Si})$. At 1000K, this configurational entropy increases the free energy of formation of the clusters by 1.22 eV per interstitial; the values ($E_{f3} - TS$) are shown in Table 2.2. Therefore, larger clusters are less favorable due to the configurational entropy.

The compact configurations of AsI_3^c and $As_2I_3^c$ are expected to dissociate instead instead of diffuse as a cluster. The neutral AsI_2 can be easily formed with excess Si interstitials and high As concentrations, and AsI has a low migration barrier of (< 0.2 eV) [37]. The relative contribution of AsI_2 and AsI to As TED can be found by evaluating $D(AsI_2)C(AsI_2)/D(AsI)C(AsI)$, where C is the defect concentration [38]. Using $D = D_0 \exp(-E_m/kT)$ with $E_m(AsI)$=0.15 eV and $E_m(AsI_2)$=0.36 eV, $D(AsI)$ is

35

approximately one order of magnitude greater than $D(AsI_2)$ at 1200 K. If $C(AsI_2)$ is greater in magnitude than $C(AsI)$ at 1200 K with excess Si interstitials under non-equilibrium conditions after ion-implantation, AsI_2 (and AsI) could be expected to make make a large contribution to As TED. For As_nI_m clustering, the most likely key intermediate states are As_2I_2 and As_2I_3. Since the migration barrier of AsI is extremely extremely low (< 0.2 eV) [37], neutral As_2I_2 can be easily formed under excess Si interstitials and high As concentrations. While neutral As_2I_2 is highly mobile and has relatively strong binding energy, it can also evolve into the larger As_2I_3 by reacting with an additional Si interstitial.

Neutral $As_2I_3^{ext}$ has a formation energy of 5.36 eV (E_{f1}) and a strong binding energy of 2.64 eV when there are three additional atoms (Table 2.2). This result implies that the neutral $As_2I_3^{ext}$ is a very stable configuration and a likely key nucleation state for larger arsenic-interstitial clusters. The high migration barrier of $As_2I_3^{ext}$ is required to support it. Unfortunately the diffusion pathway and barrier of $As_2I_3^{ext}$ is hard to determine determine explicitly due to its complex structure. To exclude the possibility of a low diffusion barrier for neutral $As_2I_3^{ext}$ we performed ab initio molecular dynamics (MD) with a 2 fs time step for 50 ps, using a Nose-Hoover thermostat to maintain the temperature at 1000 K. We did not observe a single diffusion event for the entire duration of MD run. In contrast, Estreicher et al. have shown by ab initio MD simulation [17] that the diffusion event for I_2 and I_3 can happen within few ps at 1000 K. In addition, an adaptive kinetic Monte Carlo simulation (aKMC) [39] was used to extensively search for low energy saddle points, find possible diffusion pathway for $As_2I_3^{ext}$, and calculate the dynamics of this cluster over long time scales. In our aKMC dynamics, $As_2I_3^{ext}$ is seen to exchange rapidly between conformers, crossing a low migration barrier (< 1eV), before breaking up into '$AsI_2 + AsI$' by crossing a higher

barrier (> 1eV). Thus, $As_2I_3^{ext}$ is unlikely to diffuse with low migration barrier less than 1eV and the energy cost of breaking its bond network configuration should be high.

TABLE 2.2: Formation energy (E_{f1}, E_{f2}, and E_{f3}), formation free energy ($E_{f3} - TS$) at 1000K, binding energy (E_b), and migration energy (E_m) of neutral mono-, di-, and tri- interstitials with arsenic-interstitial complexes. E_{f1} describes the energetic cost to form clusters from a perfect crystal while E_{f2} does not include the cost of forming the interstitials. E_{f3} considers the energetic cost of available interstitials from {311} extended defects which are formed by excess Si interstitials under non-equilibrium conditions during thermal annealing. Energy unit is [eV]. All of them are calculated in [216+n] atom supercell [15-18, 29, 31, 37, 38].

[216+n] atoms	Clusters	E_{f1}	E_{f2}	E_{f3}	$E_{f3} - TS$	E_b	E_m
	I	3.74					0.29
n=1	AsI	3.07	-0.67	1.33	1.33	0.67	0.15
	As_2I	2.00	-1.63	2.37	2.37	1.07	1.33
	I_2	5.49	-1.97	2.03	3.25	1.99	0.30
n=2	AsI_2	4.91	-2.50	1.50	2.72	1.88	0.36
	As_2I_2	3.90	3.51	0.49	1.71	2.19	1.03/0.42
	I_3^c	6.93	-4.25	1.75	4.18	2.30	0.49
	I_3^{ext}	6.28	-4.91	1.09	3.53	2.95	
n=3	AsI_3^c	6.71	-4.50	1.50	3.93	1.96	0.39
	AsI_3^{ext}	6.00	-5.21	0.79	3.22	2.67	
	$As_2I_3^c$	5.95	-5.27	0.73	3.17	2.05	
	$As_2I_3^{ext}$	5.36	-5.85	0.15	2.58	2.64	

2.7 SUMMARY

We presented a first-principles study of the structure and dynamics of small As-interstitial complexes (AsI_2, As_2I_2, AsI_3, and As_2I_3) in Si. The compact type configurations of AsI_3^c and $As_2I_3^c$ are expected to dissociate easily and the extended configuration, $As_2I_3^{ext}$, forms a stable bonding network and has a strong binding energy of 2.64 eV. In presence of excess Si interstitials and high As concentration, As_2I_2 could be a key intermediate state and $As_2I_3^{ext}$ could provide a key nucleation site in the formation of larger As-interstitial clusters. A diffusion mechanism for neutral AsI_2 is proposed with an overall migration barrier of 0.36 eV. Our results show that AsI_2 may significantly contribute to As TED for excess Si interstitials. A novel diffusion mechanism for neutral As_2I_2 is suggested with an overall migration barrier of 1.03 eV and an intermediate, reoriented configuration with an energy of 0.42 eV. This detailed understanding of the relative roles of small As-interstitial complexes can provide valuable guidance for ultrashallow junction engineering.

2.8 REFERENCE

[1] International Technology Roadmap for Semiconductors: 2007 Edition.

[2] A. Ural, P. Griffin, and J Plummer, J. Appl. Phys. 85, 6440 (1999).

[3] R. Kim, T. Hirose, T. Shano, H. Tsuji, and K. Taniguchi, Jpn. J. Appl. Phys., Part I 41, 227 (2002).

[4] S. Solmi, M. Ferri, M. Bersani, D. Giubertoni, and V. Soncini, J. Appl. Phys. 94, 4950 (2003).

[5] D. Mathiot and J. C. Pfister, Appl. Phys. Lett. 42, 1043 (1983).

[6] M. Ramanoorthy and S. Pantelides, Phys. Rev. Lett. 76, 4753 (1996).

[7] J. Xie and S. Chen, Phys. Rev. Lett. 83, 1795 (1999).

[8] P. M. Fahey, P. B. Griffin, and J. D. Plummer, Rev. Mod. Phys. 61, 289 (1989).

[9] P. M. Rousseau, P. B. Griffin, and J. D. Plummer, Appl. Phys. Lett. 65, 578 (1994).

[10] D. W. Lawther, U. Myler, P. J. Simpson, P. M. Rousseau, P. B. Griffin, and J. D. Plummer, Appl. Phys. Lett. 67, 3575 (1995).

[11] D. C. Muller, E. Alonso, and W. Fichtner, Phys. Rev. B 68, 045208 (2003).

[12] N. Kong, S. K. Banerjee, T. Kirichenko, S. Anderson, and M. Foisy, Appl. Phys. Lett. 90, 62107 (2007).

[13] S. A. Harrison, T. F. Edgar, and G. S. Hwang, Appl. Phys. Lett. 85, 4935 (2004).

[14] R. Brindos, P. Keys, K. Jones, and M. Law, Appl. Phys. Lett. 75, 229 (1999).

[15] Y. A. Du, R. G. Hennig, and J. W. Wilkins, Phys. Rev. B 73, 245203 (2006).

[16] Y. A. Du, S. A. Barr, K. R. A. Hazzard, T. J. Lenosky, R. G. Hennig, and J. W. Wilkins, Phys. Rev. B 72, 241306 (2005).

[17] S. K. Estreicher, M. Gharaibeh, P. A. Fedders, and P. Ordejon, Phys. Rev. Lett. 86, 1247 (2001).

[18] S. A. Harrison, T. F. Edgar, and G. S. Hwang, Electrochem. and Solid State Lett. 9, G354 (2006).

[19] P. Hohenberg and W.Kohn, Phys. Rev. 136, B864 (1964).

[20] W. Kohn and L. J. Sham, Phys. Rev. 140, A1133 (1965).

[21] G. Kresse and J. Furthmuller, VASP the Guide, Vienna Univ. of Technology, (2001); G. Kresse and J. Hafner, Phys. Rev. B, 47, RC558 (1993).

[22] J. Perdew and Y. Wang, Phys. Rev. B 45, 13244 (1992).

[23] H. Monkhorst and J. Pack, Phys. Rev. B 13, 5188 (1976).

[24] G. Henkelman, B. Uberuaga, and H. Jónsson, J. Chem. Phys. 113, 9901 (2000).

[25] G. Henkelman, A. Arnaldsson, and H. Jónsson, , Comput. Mater. Sci. 36, 254 (2006).

[26] A. D. Becke and K. E. Edgecombe, J. Chem. Phys. 92, 5397, 1990.

[27] J. Jeong and A. Oshiyama, Phys. Rev. B 64, 235204 (2001).

[28] The formation energy is defined by $E_f = E[Si_{217}As] - 217\mu_{Si} - \mu_{As}$, where $E[Si_{217}As]$ is the total energy of As-interstitial complexes in the 216 atom supercell, μ_{Si} is the energy per atom ($= E[Si_{216}/216]$) in bulk Si, and μ_{As} is the relative energy per substitutional As atom in defect-free bulk Si ($= E[Si_{215}As] - 215\mu_{Si}]$).

[29] D. Richie, J. Kim, S. Barr, K. Hazzard, R. Hennig, and J. Wilkins, Phys. Rev. Lett. 92, 45501 (2004).

[30] The formation energy is defined by $E_f = E[Si_{216}As_2] - 216\mu_{Si} - 2\mu_{As}$, where $E[Si_{216}As_2]$ is the total energy of arsenic interstitial complexes in the 216 atom supercell.

[31] A. Carvalho, R. Jones, J. Coutinho, and P. R. Briddon, Phys. Rev. B 72, 155208 (2005).

[32] $E_{f1}(As_nI_m) = E[As_nI_m] - (216 + m - n) \times \mu_{Si} - n \times \mu_{As}$.

[33] $E_{f2}(As_nI_m) = E[As_nI_m] - (216 - n) \times \mu_{Si} - m \times \mu_I - n \times \mu_{As}, \mu_I = E(Si_{217} = I) - 216 \times \mu_{Si}$.

[34] $E_{f3}(As_nI_m) = E_{f2}(As_nI_m) + E_f(\{311\})$ *per atom*,

[35] J. Kim, J. W. Wilkins, F. Khan, and A. Canning, Phys. Rev. B 55, 16186 (1997),

[36] Synopsys Sentaurus Advanced Calibration User Guide, Version A-2008.09, p76 (2008).

[37] S. A. Harrison, T. F. Edgar, and G. S. Hwang, Appl. Phys. Lett. 87, 231905 (2005).

[38] S. A. Harrison, T. F. Edgar, and G. S. Hwang, Phys. Rev. B 72, 195414 (2005).

[39] L. Xu and G. Henkelman, J. Chem. Phys (in press).

CHAPTER 3: INTERSTITIAL-MEDIATED ARSENIC DIFFUSION IN STRAINED SILICON

3.1 INTRODUCTION

By the year 2012, it is predicted by the 2007 International Technology Roadmap for Semiconductor (ITRS) that shallow junctions less than 5 nm in depth will be necessary to produce the next generation of silicon transistors [1]. To create ultra-shallow junctions (USJ), dopants are implanted into silicon, which damages the silicon and creates a large number of defects. Following dopant implantation, the silicon is thermally annealed in order to re-crystallize the silicon and electrically activate the dopants. However, it is difficult to obtain shallow junction depths and high dopant activation as the interaction of silicon defects and dopants during annealing results in enhanced dopant diffusion as well as dopant deactivation. In order to form sub-10 nm junctions with high dopant activation, a detailed atomic-level understanding of dopant-defect interactions during USJ formation is necessary. Dopant deactivation and dopant transient enhanced diffusion (TED) both present obstacles for meeting USJ requirements in the coming years. Electrical deactivation of As is believed to be due to the formation of As-vacancy complexes [2,3], while As TED is thought to be mediated by both vacancy and interstitial defects in crystalline silicon [4]. Although vacancies are thought to play a large role in diffusion and clustering processes, it is silicon interstitials that exist in excess at the onset of annealing following dopant implantation [5].

Recently, the strain effect on junction processing has received much attention due to the enhanced mobility of carriers for developing high performance strained-silicon metal oxide semiconductor field effect transistors (MOSFETs). At high concentrations ($>10^{20}$ atoms/cm^3), implanted arsenic (As) atoms may undergo electrical deactivation and

TED during post-implantation thermal annealing [6-11]. While experimental studies have focused on As deactivation and TED in strained Si on $Si_{1-x}Ge_x$ substrates, they showed that As diffusivity shows little change under a certain range of tensile strain and there is no evidence for a difference in electrically-active As concentration a as function of tensile strain [12, 13]. However, the effect of strain on As diffusion and activation/deactivation is relatively unstudied theoretically [14]. A detailed understanding of the strain effect on As TED and deactivation would provide valuable guidance to efforts to minimize the impact of strain on junction depth and dopant activation in MOSFET ultrashallow junctions.

3.2 COMPUTATIONAL DETAILS

All calculations were performed with the Vienna Ab-initio Simulation Package (VASP) which performs first principles calculations based on density functional theory (DFT) [15-17]. The exchange-correlation energy functional is represented using the generalized gradient approximation (GGA) form of Perdew and Wang [18]. The simulations were performed on a uniform grid of k points equivalent to a 2×2×2 Monkhorst and Pack grid in the diamond cubic cell [19]. A 216-atom supercell is used here. The optimized Si lattice constant for our system is 5.457 Å. We used a cutoff energy of 12 Ry for plane-wave expansion. All atoms are fully relaxed using conjugate gradient method to minimize the total energy until all residual forces on the atom are less than 5×10^{-2} eV/Å. We calculate the diffusion barriers under the static approximation using the climbing nudged elastic band method [20].

In order to induce a biaxial strain in Si, we applied the lattice constant ($a_\parallel$) of relaxed $Si_{1-x}Ge_x$ to the two crystallographic directions on the (001) plane. Then we

(1)

optimized the lattice constant ($a_\perp$) in the other direction perpendicular to the strain plane in a 216-atom supercell. According to elastic theory, the "in-plane" biaxial strain $\varepsilon_\parallel$ can change the "out-of-plane" strain $\varepsilon_\perp$ by the equation

$$\varepsilon_\perp / \varepsilon_\parallel = -2(C_{12} / C_{11})$$

(3.1)

where C_{11} (167 GPa) and C_{12} (65 GPa) are elastic constants of Si [21]. We used a "in-plane" lattice constant of 5.500 Å and a "out-of-plane" lattice constant of 5.426 Å in order to induce a 0.79 % biaxial tensile strain (equivalent to the relaxed "in-plane" lattice constant of $Si_{80}Ge_{20}$). The calculated $\varepsilon_\perp / \varepsilon_\parallel$ are in excellent agreement with the experimental values obtained from (3.1).

3.3 ARSENIC DEACTIVATION IN STRAINED SILICON

We investigated the thermodynamic energetics of As-vacancy complexes in unstrained and strained Si in order to understand how a biaxial tensile strain can affect the stability of As-vacancy complexes. It is widely accepted that the deactivation of As is due to the formation of As_nV_m clusters [9-11]. At concentrations greater than 3×10^{20} atoms/cm^2, arsenic (As) impurities have been observed to deactivate at temperatures as low as 400 °C [10]. Theoretical studies have suggested that AsV, As_2V, As_3V, As_4V, As_2V_2, and As_3V_2 all may play a role in As deactivation. This deactivation model has been supported by results from positron annihilation and Hall effect experiments [22-24].

We calculated the formation energies and binding energies of small clusters of As vacancy complexes, as shown in Table 3.1 [25]. When the isolated impurities As and V are considered as reference, the formation energy of a cluster is given by

44

$$E_{formation} = E_{As_n V_m} - n(E_{As} - E_{Si}) - E_{Si} \frac{N-m}{N},$$

$$(3.2)$$

where E_{Si} has N atoms, E_V has (N-1) atoms, and $E_{As_n V_m}$ has (N-m) atoms in the supercell. The binding energies are given by

$$E_{binding} = \frac{E_{formation}(As_n V_m) - E_{formation}(V_m)}{n}.$$

$$(3.3)$$

The formation energies of vacancy and di-vacancy are slightly increased under 0.79% biaxial tensile strain. Although a biaxial tensile strain ("in-plane" direction) is given, the stress would be released by the compressive strain ("out-of plane" direction), which shows a small change in formation energy of vacancy and di-vacancy. There are small differences in the formation energies of As-vacancy and As-divacancy complexes between unstrained and 0.79% strained Si. Thus, it appears that a biaxial tensile strain will have a very little effect on the stability of these complexes.

3.4 INTERSTITIAL-MEDIATED ARSENIC DIFFUSION IN STRAINED SILICON

Density functional theory calculations were used to examine the interaction of interstitials and various As-vacancy complexes [26]. Harrison *et. al.* have shown that silicon interstitials can easily annihilate existing As-vacancy complexes in silicon with little kinetic barrier to interstitial recombination with the vacancies, $As_m V$ (m=1-4) and $As_m V_2$ (m=2-3) [27]. The energy gain from the interstitial-vacancy recombination turns out to be significant, implying that As would remain more favorably as As_m (or $As_m I_n$) complexes, rather than as $As_m V_n$ in the presence of a large amount of excess interstitials [26,27].

TABLE 3.1: Formation energy and binding energies (in eV) of AsnVm complexes. The values are calculated for electrically neutral complexes.

	Unstrained Si		Strained Si (0.79 % strain)	
	$E_{formation}$	$E_{binding}$ per As atom	$E_{formation}$	$E_{binding}$ per As atom
As_2	0.07	0.03	0.09	0.04
As_3	0.18	0.06	0.20	0.07
As_4	-0.49	-0.12	-0.44	-0.11
V	3.67		3.71	
AsV	2.27	1.39	2.33	1.37
As_2V	0.62	1.52	0.71	1.50
As_3V	-0.64	1.44	-0.52	1.41
As_4V	-2.30	1.49	-2.15	1.46
V_2	5.48		5.53	
As_2V_2	2.32	1.58	2.32	1.60
As_3V_2	1.07	1.47	1.23	1.43

Moreover, the formation of a highly mobile As-silicon interstitial pair that can exist in positive, neutral, negative charge state can be explained by experimentally observed As TED mediated by interstitials [6-8]. This suggests the importance that interstitials may play in As TED.

The lowest energy As-Si$_i$ structures were identified in the negative, neutral, and positive charge state [26]. In the negatively charged As-Si$_i^-$ structure, the As atom bridges two approximate lattice Si atoms, as depicted in Fig. 3.1(a). For As-Si$_i^0$ and As-Si$_i^+$, the lowest energy structure is comprised of As and Si$_i$ atom that are aligned in the [110] direction while sharing a lattice site [Figs 2.1(a) and 2.3(a)]. These findings suggest that under intrinsic conditions the diffusion of neutral As-Si$_i$ pairs dominate, while under n-type extrinsic conditions the neutral and negatively charge pairs will both contribute to arsenic diffusion. These results clearly support that the interstitials can contribute significantly to As transient enhanced diffusion, particularly in regions where interstitials exist in excess

We investigated the stability and diffusion of arsenic-interstitial pair under 0.79 % biaxial tensile strain. We assessed the relative stability of these neutral and charged As-Si$_i$ pairs by computing defect ionization levels (μ_i). At a given Fermi level (ε_F), the relative formation energy of a charged defect in charge state q=±1 to a neutral is given by

$$E_f^q - E_f^0 = q(\varepsilon_F - \mu_i),$$

(3.4)

where ε_F is given relative to the valence band maximum (E_V). Thus, the defect levels can be approximated by

$$E_D^q + q(E_V^q + \mu_i) = E_D^0,$$

(3.5)

where E_D^q and E_D^0 are the total energies of the defects in q and neutral charge states, and E_V^q is the position of the valence band maximum in supercell E_D^q. In calculating a charged defect, a homogeneous background charge is included to maintain the overall charge neutrality in the periodic supercell. To account for the Coulomb energy between the charged defect and background charge, a monopole correction is made to the total energy of the charged system. Assuming a pointlike +1 charge defect in the 216-atom supercell, the monopole correction is estimated to be approximately 0.11 eV [28]. This correction may overestimate the required adjustment if the charge on the defect is significantly delocalized [29].
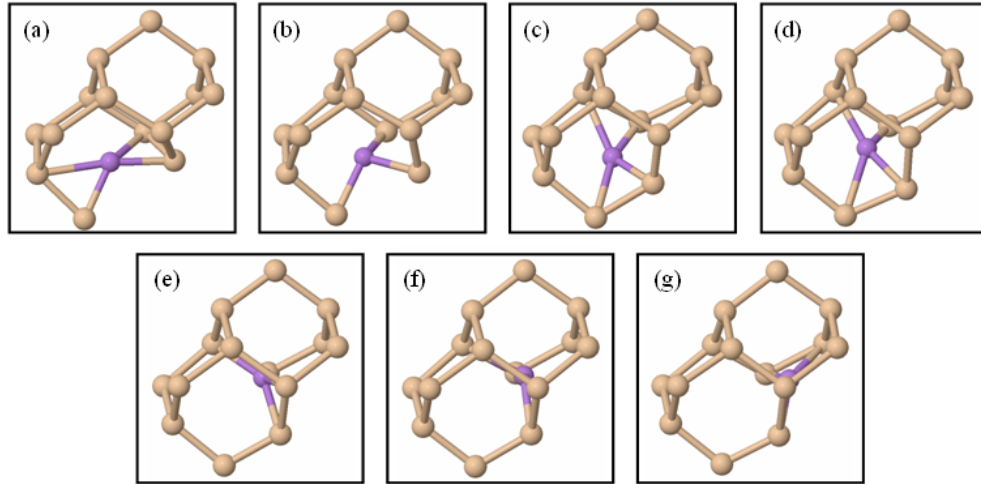
FIGURE 3.1: The negatively charged As-Si$_i$ pair diffusion pathway in unstrained and strained structure.
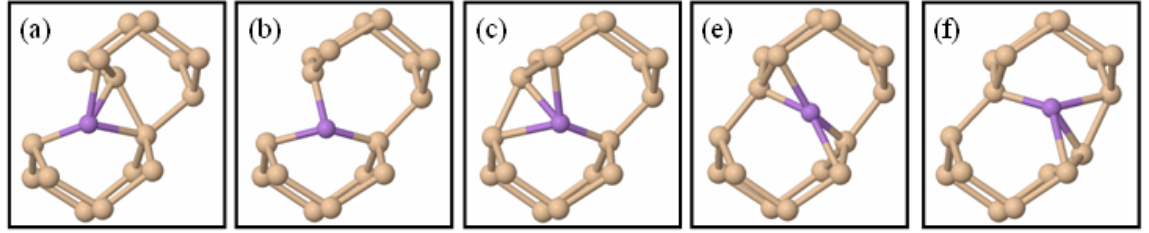
FIGURE 3.2: The As-Si$_i$ pair diffusion pathway for mechanism "A" in unstrained and strained Si.
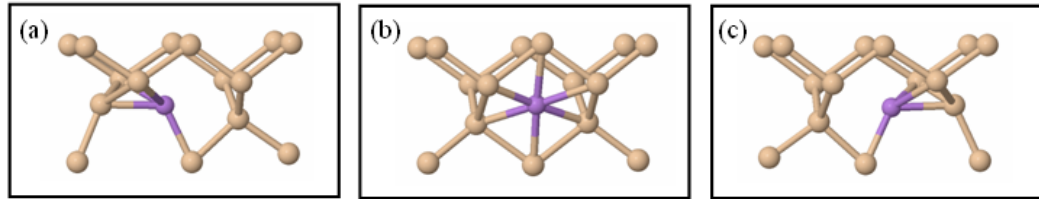
FIGURE 3.3: The As-Si$_i$ pair diffusion pathway for mechanism "B" in unstrained and strained Si.

Note that these relative formation energy is determined using computed Si band gap of 0.63 eV and 0.50 eV in unstrained and strained Si, respectively From the calculations, we determined the positions of As-Si$_i^0$ acceptor and donor levels at E_V+0.22 eV and E_V+0.11 eV, respectively for the computed Si band gap of 0.63 eV in unstrained Si. For 0.79% biaxial strain Si, we determined the positions of As-Si$_i^0$ acceptor and donor levels at E_V+0.14 eV and E_V+0.16 eV, respectively, for the computed Si band gap of 0.50 eV.

We adopt the same As diffusion mechanism as in [26] to study As diffusion in strained Si as shown Fig. 3.1, Fig. 3.2 and Fig. 3.3. The formation energies, migration barriers, activation energies are shown in the Table 3.2. When the biaxial strain is induced on the As-Si$_i$ pair in a 216-atom supercell by the [110], [101], and [001] direction, there is no directional dependence on the formation energy of As-Si$_i$ pair. The formation energy of As-Si$_i^0$ in strained Si is calculated to be 2.96 eV (= E[AsSi$_{216}$]-

E(AsSi$_{215}$]-E[Si$_{216}$]/216), where E[AsSi$_{216}$], and E(AsSi$_{215}$], E[Si$_{216}$] are the total energies of As-Si$_i^0$, substitutional As$_0$, and crystalline Si). This leads to formation energies of 2.87 eV and 3.07 eV in strained Si, respectively for As-Si$_i^-$ and As-Si$_i^+$ in intrinsic regions. Under intrinsic condition, the binding energies of As-Si$_i^0$ As-Si$_i^-$, and As-Si$_i^+$ are approximated to be 0.72 eV, 0.81 eV, and 0.61 eV, respectively, relative to the dissociation products of substitutional As^0 and (110)-split Si$_i^0$.

Under intrinsic conditions, the neutral and positively charged As-Si$_i$ pair are about 0.1 eV more favorable in strained Si than they are in unstrained Si. For the negatively charged As-Si$_i$ pair, there is almost no difference on the stability in unstrained and strained Si under intrinsic conditions. However, the formation energy of negatively charged As-Si$_i$ pair in strained Si is slightly higher than that in unstrained Si under extrinsic conditions, even though the formation energies of neutral and positively charged As-Si$_i$ pairs in strained Si are lower than they are in unstrained Si. The diffusion barrier is obtained by [110], [101], [001] directions of biaxial tensile strain. The diffusion anisotropy of the migration barrier (ex. [110]$\rightarrow$ [101]) is insignificant.

Based on the activation energies of As-Si$_i$ pair diffusion in Table 3.2, we can evaluate the strain effect on the diffusivity of As-Si$_i$ pair. While the activation energies of neutral and positively charged As-Si$_i$ pair in strained Si are lower in both intrinsic and extrinsic regions, as compared to their activation energies in unstrained Si, the activation energies of the negatively charged As-Si$_i$ in unstrained and strained Si are very comparable. For biaxial tensile strain, As will diffuse similarly in unstrained and strained Si under TED conditions as the negatively charged As-Si$_i$ pair will dominate in the case of heavily As-doped Si. [12,13].

TABLE 3.2: Formation energies (E_F) of As-Si$_I$ pairs as well as migration (E_M) and activation energies (E_A) for their diffusion (in eV). E_F(INT) and E_F(EXT) are the formation energies under intrinsic and extrinsic conditions, respectively. E_A(INT) and E_A(EXT) are the activation energy of As-Si$_I$ under intrinsic and extrinsic condition, respectively, where E_A(INT) = E_F(INT) + E_M and E_A(INT) = E_F(INT) + E_M. Extrinsic conditions are taken to occur at the computed conduction band edge.

	$E_f(int)$	$E_f(ext)$	E_m	$E_a(int)$	$E_a(ext)$
Unstrained Si					
As-Si$_i^-$	2.88	2.57	0.51	3.39	3.08
As-Si$_i^0$	3.09	3.09	0.15	3.24	3.24
As-Si$_i^+$	3.18	3.72	0.12	3.30	3.84
Strained Si (0.79 % strain)					
As-Si$_i^-$	2.87	2.62	0.41	3.28	3.03
As-Si$_i^0$	2.96	2.96	0.14	3.10	3.10
As-Si$_i^+$	3.07	3.32	0.10	3.17	3.42

3.5 SUMMARY

We have studied As-vacancy and interstitial-mediated As diffusion in strained Si by using DFT calculations. First, biaxial tensile strain was found not to significantly affect As deactivation. Second, tensile strain increases the stability of As-Si$_i$ pairs. Finally, an interstitial-mediated As diffusion in heavily As-doped Si will not be significantly affected by induced biaxial tensile strain.

3.6 REFERENCE

[1] International Technology Roadmap for Semiconductors: 2007.

[2] K.C. Pandey, A. Erbil, G.S. Cargill III, R.F. Boehme, and D. Vanderbilt, Phys. Rev. Lett. **61**, 1282 (1988).

[3] P.M. Rousseau, P.B. Griffin, and J.D. Plummer, Appl. Phys. Lett. **65**, 578 (1994).

[4] P.M. Fahey, P.B. Griffin, and J.D. Plummer, Rev. Mod. Phys. **61**, 289 (1989).

[5] M.D. Giles, J. Electrochem. Soc. **138**, 1160 (1991).

[6] A. Ural, P. Griffin, and J Plummer, J. Appl. Phys. **85**, 6440 (1999).

[7] R. Kim, T. Hirose, T. Shano, H. Tsuji, and K. Taniguchi, Jpn. J. Appl. Phys., Part I **41**, 227 (2002).

[8] S. Solmi, M. Ferri, M. Bersani, D. Giubertoni, and V. Soncini, J. Appl. Phys. **94**, 4950 (2003).

[9] D. Mathiot and J. C. Pfister, Appl. Phys. Lett. **42**, 1043 (1983).

[10] M. Ramanoorthy and S. Pantelides, Phys. Rev. Lett. **76**, 4753 (1996).

[11] J. Xie and S. Chen, Phys. Rev. Lett. **83**, 1795 (1999).

[12] N. Sugii, S. Irieda, J. Morioka, and T. Inada, J. Appl. Phys. **96**, 261 (2004).

[13] G. Dilliway, A. Smith, J. Hamilton, J. Benson, L. Xu, P. McNally, G. Cooke, H. Kheyrandish, N. Cowern, Nucl. Instr. And Meth. in Phys. Res. B **237**, 131 (2005).

[14] S. T. Dunham, M. Diebel, C. Ahn, and C. L. Shih, J. Va. Sci. Technol. B **24**, 456 (2006).

[15] P.Hohenberg and W.Kohn, Phys. Rev. **136**, B864 (1964).

[16] W. Kohn and L.J. Sham, Phys. Rev. **140**, A1133 (1965).

[17] G. Kresse and J. Furthmuller, VASP the Guide, Vienna Univ. of Technology, (2001); G. Kresse and J. Hafner, Phys. Rev. B, **47**, RC558 (1993).

[18] J. Perdew and Y. Wang, Phys. Rev. B **45**, 13244 (1992).

[19] H. Monkhorst and J. Pack, Phys. Rev. B **13**, 5188 (1976).

[20] G. Henkelman, B. Uberuaga, and H. Jónsson, J. Chem. Phys. **113**, 9901 (2000).

[21] L. Lin, T. Kirichenko, B. Sahu, G. S. Hwang, and S. K. Banerjee, Phys. Rev. B **72**, 205206 (2005).

[22] D. W. Lawther, U. Myler, P. J. Simpson, P. M. Rousseau, P. B. Griffin, and J. D. Plummer, Appl. Phys. Lett., **67** 3575 (1995).

[23] V. Ranki, J. Nissilä, and K. Saarinen, Phys. Rev. Lett. **88**, 105506 (2002).

[24] V. Ranki, K. Saarinen, J. Fage-Pedersen, J. Lundsgaard Hansen, and A. Nylandsted Larsen, Phys. Rev. B **67**, 041201(R), (2003).

[25] D. Mueller, E. Alonso, and W. Fichtner, Phys. Rev. B **68** , 045208 (2003).

[26] S. A. Harrison, T. F. Edgar, and G. S. Hwang, Appl. Phys. Lett. **87**, 231905 (2005).

[27] S.A. Harrison, T.F. Edgar, and G.S. Hwang, Appl. Phys. Lett. **85**, 4935 (2004).

[28] G. Makov and M. Payne, Phys. Rev. B 51, 4014 (1995).

[29] D. Segev and S. H. Wei, Phys. Rev. Lett. **91**, 126406 (2003).

CHAPTER 4: BORON DIFFUSION RETARDATION IN SILICON-GERMANIUM

4.1 INTRODUCTION

Scaling of complementary metal oxide semiconductor (CMOS) devices below sub-100 nm is challenging. This aggressive scaling will not be possible without incorporation of new materials and adoption of novel device structures [1]. Channel and junction engineering using $Si_{1-x}Ge_x$ layers in bipolar and CMOS transistors has been employed extensively due to potential performance enhancement with higher carrier mobility due to low effective mass and relative ease of integration with conventional silicon processing [1-6]. When n-type and p-type dopants are introduced into $Si_{1-x}Ge_x$ by low energy ion implantation, suppression of transient enhanced diffusion (TED) of boron, a common p-type dopant, is one of the major challenges for sub-100nm transistors, highlighting the need to better understand the underlying mechanism of defect-dopant diffusion in $Si_{1-x}Ge_x$ [1, 7-9].

Despite many experimental and theoretical studies have been performed there is no consensus on the identity and the physical mechanism of boron diffusion retardation in $Si_{1-x}Ge_x$. Experimental studies have shown that boron diffusivity in $Si_{1-x}Ge_x$ is decreased at low Ge concentrations [10] and increased again at high Ge concentrations [11, 12]. The two key factors that affect boron diffusion retardation in $Si_{1-x}Ge_x$ system at low Ge concentrations are biaxial stress effect and Ge chemical effect. In perspective study of the strain effect, Cowern *et. al.* showed that slower boron diffusion is originated from the effect of compressive strain in $Si_{1-x}Ge_x$ grown on Si substrate [13] while Kuo *et. al.* found that it may even exist in relaxed $Si_{1-x}Ge_x$, demonstrating a weak strain dependence [14].

In regards to Ge chemical effect, Moriya *et. al.* proposed that the bandgap narrowing from higher Ge concentrations may affect the concentrations of positively charged interstitials thus reducing the boron diffusivity [15]. However, other diffusion studies showed the bandgap narrowing by higher Ge concentration may not be a major factor affecting boron diffusion retardation [16]. Recent density functional theory (DFT) study by Wang *et. al.* showed that the boron diffusion is reduced by increase of the formation energy of Si interstitial in the presence of Ge and hence decrease in the number of interstitials and, in turn, BI pairs [17].

The relative role of self-interstitials and the underlying mechanisms of boron diffusion in $Si_{1-x}Ge_x$, are investigated using first principles DFT study. First, we discuss the structure and relative stability of Si interstitial (Si^I) and Ge interstitial (Ge^I) in the neutral and charged state. Second, we investigate a relative concentration of Si-B pair and Ge-B pair which can contribute to boron diffusion in $Si_{1-x}Ge_x$. Third, we propose that Ge^I play an important role in the initial nucleation of the small clusters, resulting in the localization of Si clustering. Finally, the mechanism of boron diffusion retardation is proposed while relative contributions of local strain effect and chemical effect due to germanium are addressed.

We investigate the structure and energies of Si^I and Ge^I using the plane-wave pseudopotential method within the density functional theory (DFT) as implemented in the Vienna *Ab initio* Simulation Package (VASP) [18]. The exchange-correlation energy functional is represented using the generalized gradient approximation (GGA) in the Perdew and Wang form (PW91) [19]. The planewave cutoff energy is 16 Ry. The optimized Si lattice constant for GGA in our system is 5.457 Å. A 64-atom supercell is used and it is also checked in a 216-atom supercell. All atoms are fully relaxed using conjugate gradient method to minimize the total energy until all residual forces on each

55

constituent atom become smaller than 5×10^{-2} eV/Å. The simulation is performed on a uniform grid of k points equivalent to a $4\times4\times4$ Monkhorst and Pack grid in the diamond cubic cell. We calculate the diffusion barriers using the nudged elastic band method (NEBM) and the climbing NEBM. In a charged defect, a homogeneous background charge is included to maintain the overall charge neutrality. To compensate for the electrostatic energy between the charged defect and the background charge, a monopole correction, (+1) charged defect and (+2) charged defect have 0.11 eV and 0.43 eV respectively, is made to the total energy of the charged system for 216 supercell.

4.2 GERMANIUM EFFECT ON B-INTERSTITIAL PAIR DIFFUSION

Germanium[I] can be introduced into the system either during Ge-preamorphization of Si or during ion implantation in Si$_{1-x}$Ge$_x$. In both cases, it would be able to be an important diffusion mediator of boron TED. In order to evaluate the Ge effects for dopant interactions, we present the structure and energetics of Ge[I] and Si[I] in a Si matrix at first. The formation energy of point defects with charge Q is evaluated as

$$E_f^Q = (E_D^Q - E_D^0) + Q(\varepsilon_F + \varepsilon_v) - \sum_s n_s \mu_s$$

(4.1)

where E_D^Q is the calculated total energy of the supercell containing the defect D, E_X^0 is the total energy of the bulk Si with the same number of atoms as in the defect supercell; ε_F is the Fermi level, and $\varepsilon_v = (E_X^0 - E_X^{+1})$ is the valence band top. n_s and μ_s are the chemical potential and the number of the atomic species, respectively [20].
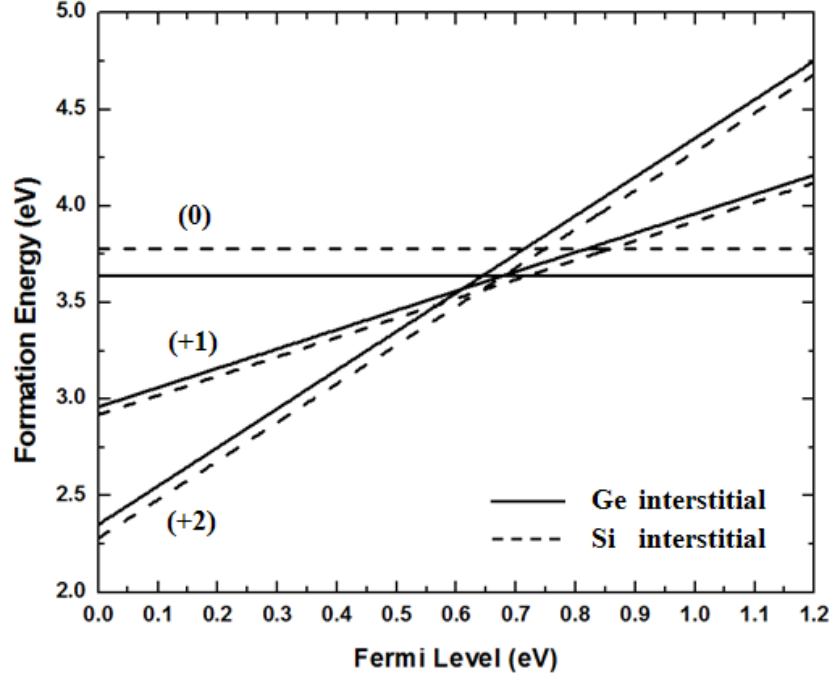
FIGURE 4.1: The formation energies of the most stable Si interstitial (dashed line) and Ge interstitial (solid line) at different charge states with respect to the Fermi level. For the neutral state, Si-Ge split-(110) structure is more stable compared to Si-Si split-(110) by 0.1 eV. For the positively charged state, Si^T and Ge^T exist comparably even though the formation energy of Si^T is slightly lower than that of Ge^T.

By Eq. (4.1), we derive a relative stability of Si^I and Ge^I in the neutral and charged state, which can give an important physical insight needed to understand the key interactions between interstitials and dopants. In Table 4.1, we provide the formation energies of Ge^I and Si^I in the neutral state. Our calculations show that $Ge^I Si_S$, which is split-(110) interstitial, has the lowest formation energy by 3.64 eV compared to other interstitial configurations in the presence of Ge. It means that the local strain by Ge atom in the system is released sufficiently when Ge atom is placed into split-(100) interstitial position. However, even though Ge split-(100) is quite favorable, Ge^I is supposed to have

a lower mobility than Si^I due to a higher energy barrier between split-(110) and hexagonal site.

TABLE 4.1: The formation energy of the interstitial and substitutional positions of Ge atom in the neutral state which show local strain effect and chemical effect due to Ge atom. Si-Ge split-(110) is the most stable structure and Ge atom gives a local strain effect only for the 1st nearest neighbor, showing relative stability of point defects in presence of Ge atom.

	Split-(110) I	Hexagonal I	Tetrahedral I
$Si^I Ge_S{}^{1NN}$	3.80	3.91	3.84 (unstable)
$Si^I Ge_S{}^{2NN}$	3.74	3.83	4.02 (unstable)
$Si^I Ge_S{}^{3NN}$	3.73	3.84	4.11
$Si^I Si_S$	3.73	3.84	4.10
$Ge^I Si_S$	3.64	4.10	4.12

We also found that strain effect induced by Ge atom in the lattice is limited by 1st nearest neighbor (NN) from Si^I. As Ge atom moves away from the 1st NN to the 3rd NN, the formation energies of $Si^I Ge_S{}^{1NN}$ is higher than those of $Si^I Si_S$, but the formation energies of $Si^I Ge_S{}^{2,3NN}$ are same as those of $Si^I Si_S$. As a result, the strain effect is localized into the 1st NN in the lattice and is almost eliminated from Si^I when Ge atom exists far away from 1st NN, showing the same formation energies of the $Si^I Ge_S{}^{2,3NN}$ and $Si^I Si_S$. In the meanwhile, Si^I shows unstable tetrahedral structures in the 1st NN and 2nd NN and seems to be more sensitive to Ge atom.

Next we compare the relative stability of the Si^I and Ge^I in the positively charged state. Fig. 4.1 shows the formation energies of positively charged interstitials in the most stable tetrahedral structures, which are a $Si^{T+} Si_S$ and $Ge^{T+} Si_S$, respectively. The formation

energies of $Si^{T+}Si_S$ ($Si^{T++}Si_S$) and $Ge^{T+}Si_S$ ($Ge^{T++}Si_S$) with Fermi level at valence band edge are, correspondingly 2.92 eV (2.28 eV) and 2.96 eV (2.35 eV), respectively. The migration barrier energy for Ge^{T+} (Ge^{T++}) and Si^{T+} (Si^{T++}) through hexagonal site is calculated 0.6 eV (1.38 eV) and 0.42 eV (1.20 eV), respectively. Although Ge^T has a slightly higher formation energy than Si^T in the charged state, it is an almost same formation energy in the whole Fermi level. Therefore, we conclude that Ge^I co-exists with Si^I in the neutral and (+1) charged states.

Based on the assumption of equivalent chances for interstitial-mediated boron diffusion by Si^I and Ge^I, we investigate the relative concentration of BI pairs (Si^IB_s and Ge^IB_s) with the relative stability and diffusion pathway. Fig. 4.2 shows the atomic configurations of BI pairs with different species. For neutral case, the formation energies of Ge^TB_s [Fig. 4.2 (a)] and Si^TB_s [Fig. 4.2 (c) and (d)] have 2.94 eV and 2.70 eV, respectively. For (+1) charge case, the formation energies of $Ge^{T+}B_s$ [Fig. 2 (a)] and $Si^{T+}B_s$ [Fig. 4.2 (c) and (d)] have 2.67 eV and 2.44 eV in the midgap (E_F=0.6 eV), respectively. The formation energy of B-Ge pair has around 0.2 eV higher than that of B-Si pair.

In neutral state we found binding energy of Ge^TB_S is equal to 0.46 eV with respect to the dissociation products, Ge^{T+} and B_S^- while that of Si^TB_S is 0.71 eV with respect to the dissociation products, Si^{T+} and B_S^-. In (+1) charge state, the binding energy of $Ge^{T+}B_S$ is 0.67 eV with respect to the dissociation products, Ge^{T++} and B_S^-, while that of $Si^{T+}B_S$ is 0.91 eV with respect to the dissociation products, Si^{T++} and B_S^-.
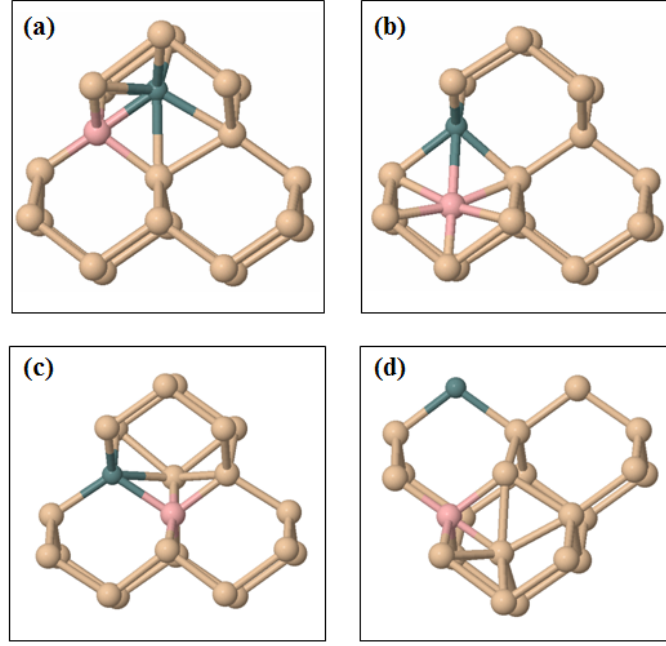
FIGURE 4.2: Atomic Ge-B configuration involved in boron diffusion. The yellow, green, and purple balls are Si, Ge, and B atoms respectively. (a) Ge^TB_S (tetrahedral), (b) B^H (hexagonal), (c) Si^TB^S (tetrahedral) near Ge, (d) Si^TB^S (tetrahedral) away from Ge.

We compare the relative concentration of BI pair in the perspective of Si^I and Ge^I. The basis of the model is that an interstitial in BI pair may spontaneously escape at a rate given by interstitial hopping frequency and binding energy to BI pair, while the BI pairs are formed whenever diffusing interstitials are trapped by a boron [21]. The overall equation governing a BI kinetics is then given by Eq (4.2);

$$\frac{\partial C_{BI}}{\partial t} = 4\pi\alpha a D_I C_I C_B - C_{BI}\frac{D_I}{a^2}\exp(-E_b/kT)$$

(4.2)

where $D_I = D_0\exp(-E_m/kT)$ is the interstitial diffusivity, a is the interatomic spacing, α is the capture radius expressed in units of a, while $C_{BI}(x,t)$ is the concentration of

overall BI pairs, $C_I(x,t)$ is the concentration of free interstitials, E_b is the binding energy of BI pair, and T is the annealing temperature [21].

In the neutral case, $E_m(Ge)$ and $E_m(Si)$, defined by the most limiting case between split-(110) and hexagonal site, is 0.42 eV and 0.11 eV, respectively. In (+1) charge case, $E_m(Ge)$ and $E_m(Si)$, defined by energy difference between tetrahedral and hexagonal site, is 0.6 eV and 0.42 eV, respectively. In both neutral and charged case, $C_{BI}(Ge)$ should be lower than $C_{BI}(Si)$ because $D_I(Ge)$ is smaller than $D_I(Si)$. As a result, the probability of Ge^I to approach into a substitutional boron will be also lowered because the diffusivity of Ge^I is low.

From the latter part of Eq. (2), dissociation rate of B-Ge complex is higher than that of B-Si complex because B-Ge pair has a lower binding energy by 0.25 eV than B-Si pair in the neutral and charged case. Therefore, Ge-B pair becomes easily dissociated compared to Si-B pair even if Ge-B pair is formed because the binding energy of Ge-B pair is smaller than that of Si-B pair.
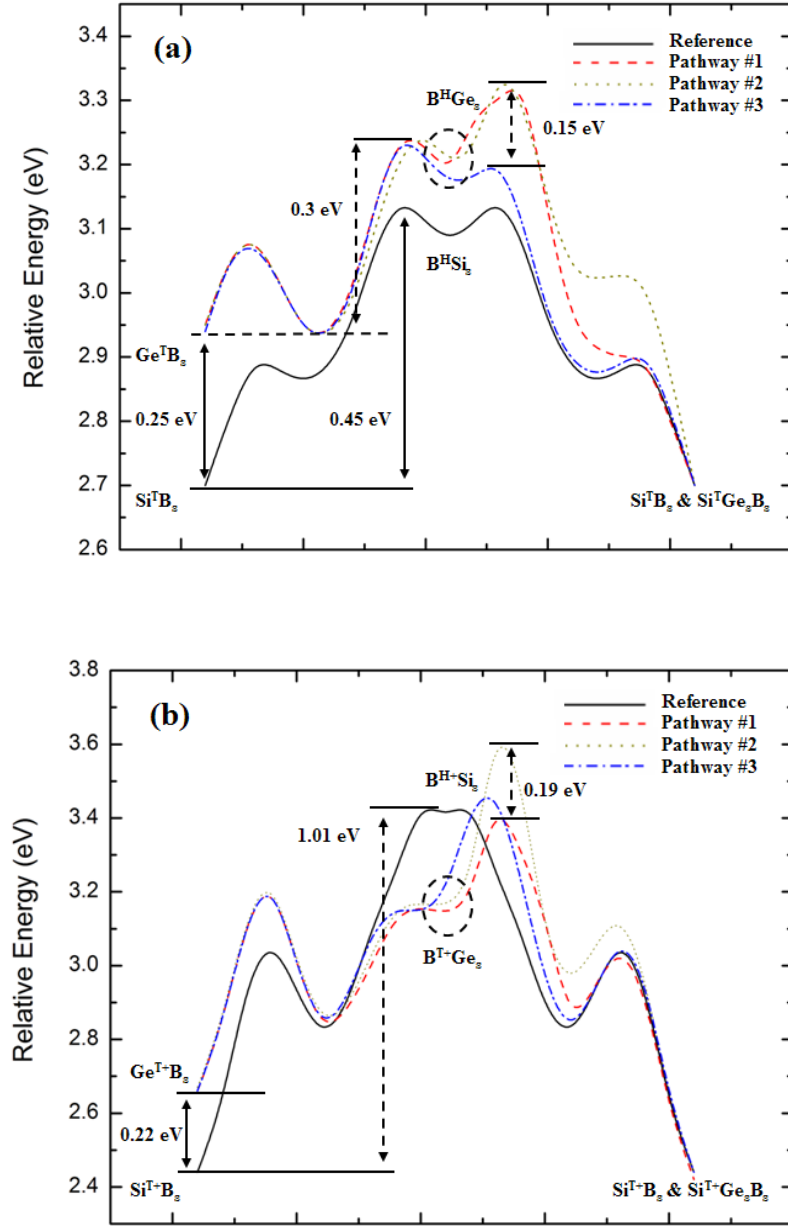
FIGURE 4.3: The diffusion barriers of boron interstitial in the presence of Ge in the neutral and charged state. The reference pathway is for Si-B pair in the neutral and charged state. Pathway #1 and #2 depends on the kick-in direction of B^H for split-(100) Si-B pair. In the split-(100) of Si-B pair, Ge atom has a direct bonding with Si atom in the pathway #1 but Ge atom has a direct bonding with B atom in the pathway #2. The pathway #3 shows B^H kicks into Si atom far away from Ge atom.

Moreover, the actual number of Si^I to mediate a boron is decreased compared to the case of no Ge because Ge^I is also energetically favorable due to either Ge-preamorphization or ion implantation of $Si_{1-x}Ge_x$. In addition, a slower diffusion process will be shown, if any, in case of boron and germanium interaction because Ge atom moves very slowly compared to boron in a Si matrix due to its size effect. Therefore, it would be one of the possible explanations for boron retardation in the presence of Ge because overall $C_{BI}(Ge)$ is decreased and then Ge^I would not be able to mediate a substitutional boron.

In the perspective of B-interstitial (B^I), we have shown the three possible diffusion pathways in Fig. 4.3; 1) diffusion pathway which boron kicks out Ge atom [Fig. 4.2 (b) → Fig. 4.2(a)], 2) diffusion pathway which boron kicks out Si near Ge atom [Fig. 4.2(b) → Fig. 4.2(c)], and 3) diffusion pathway which boron kicks out Si away from Ge atom [Fig. 4.2(b) → Fig. 4.2(d)].

Supposed that a mobile B^I travels through the Si-matrix and then makes a kick-out event in the neutral state, B^H should select either the diffusion pathway of Si^TB_S or the diffusion pathway of Ge^TB_S in Fig 4.3(a). Once B^H choose the diffusion pathway of Ge^TB_S, Ge-B pair would be easily dissociated due to lower binding energy than Si-B pair or it would be back into B^H due to the higher formation energy by around 0.25 eV than Si^TB^S. The former explains that Ge will leave behind the boron into the lattice, inducing the boron retardation in the lattice.

The migration barrier of Si^TB_S should be also influenced by nearby Ge atom when B^H kicks out the Si atom because the formation energy of B^HGe_S is increased in the presence of Ge, The diffusion pathway which jumps into 1st NN Si atom of Ge atom [pathway #1 and #2 in Fig. 4.3(a)] has higher migration energy by 0.15 eV than the diffusion pathway which jumps into 3rd NN Si atom of Ge atom [pathway #3 in Fig.

63

4.3(a)]. The diffusing direction of Si-B pair will prefer to the directions escaping from substitutional Ge atom, resulting in a slow diffusion process of Si-B pair with higher Ge concentrations.

In the charged state in Fig. 4.3(b), B^I is a significantly deviated due to Ge atom from hexagonal site and is likely to move into tetrahedral site. The formation energy of B^I is lowered in the presence of Ge and in turn migration uphill is generated when B^I kicks out Si atom in the charged state. In Fig. 4.3(b), the pathway #1 has a lower energy barrier 0.19 eV than the pathway #2 because it depends on the kick-in directions into Si atom by B atom ([010] and [001]) in the transition state of split-(100) for the charged state. However, the charged state doesn't show a migration energy difference when B^I chooses the diffusion pathway of $Si^T B_S$.

We propose that Ge^I play an important role on an initial nucleation of the small clustering, resulting in the localization of Si clustering and reducing the density of Si extended defects. Fig. 4.4 shows the most stable compact and extended structure of Si-clustering from I to I_4 [22-24]. From the energetic study of Ge^I, Ge-Si dumbbell is energetically favorable but Ge^I is relatively immobile due to higher migration barrier into hexagonal site. It suggests a possibility that Si-Ge dumbbell can grow into a larger clustering rather than Ge^I travels through the Si-lattice.
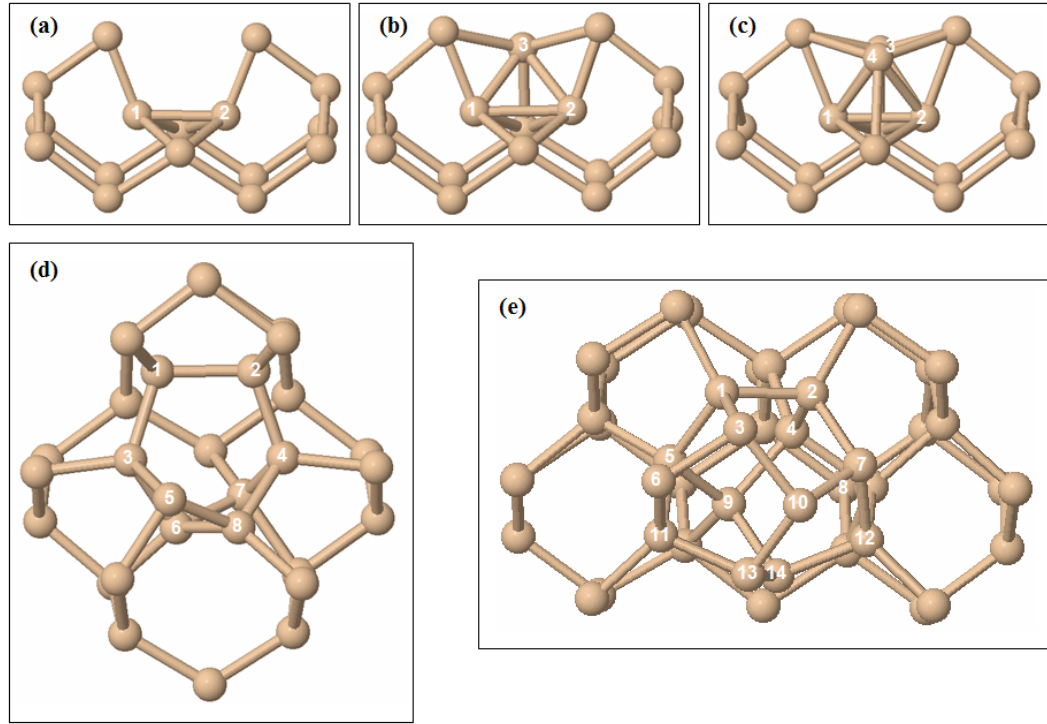
FIGURE 4.4: The most stable atomic configuration of Si cluster in the compact and extended structure: (a) I (split-110)) (b) compact I_2 (c) compact I_3 (d) extended I_3 (e) extended I_4.

In order to verify it, we present the formation energy of clustering in Fig. 4.5 based on the atomic clustering structure of Fig. 4.4. With introducing an additional Ge atom into the Si matrix, we have investigated whether Ge atom will agglomerate into the clustering or Ge atom will move into substitutional site. Because there are a lot of possible combinations of Ge positions, we have only shown two extreme cases in this paper in Fig. 4.5; 1) Si clustering in presence of substitutional Ge and 2) Si and Ge complex clustering with no substitutional Ge atom.

In the compact clustering structure, the formation energy of Si and Ge complex clustering is lower than that of Si clustering with a substitutional Ge atom (not shown

compact I_3 in Fig 4.5). However, because Ge^I is relatively immobile in Si matrix, Si-Ge dumbbell would collect either a mobile Si^I or available nearby Ge^I to form a larger compact clustering (I_2 and I_3). In the extended clustering structure, Ge atom prefers to move into substitutional site because the energy increase by breaking the symmetry of clustering is higher than the strain reduction of Ge atom in the clustering position.
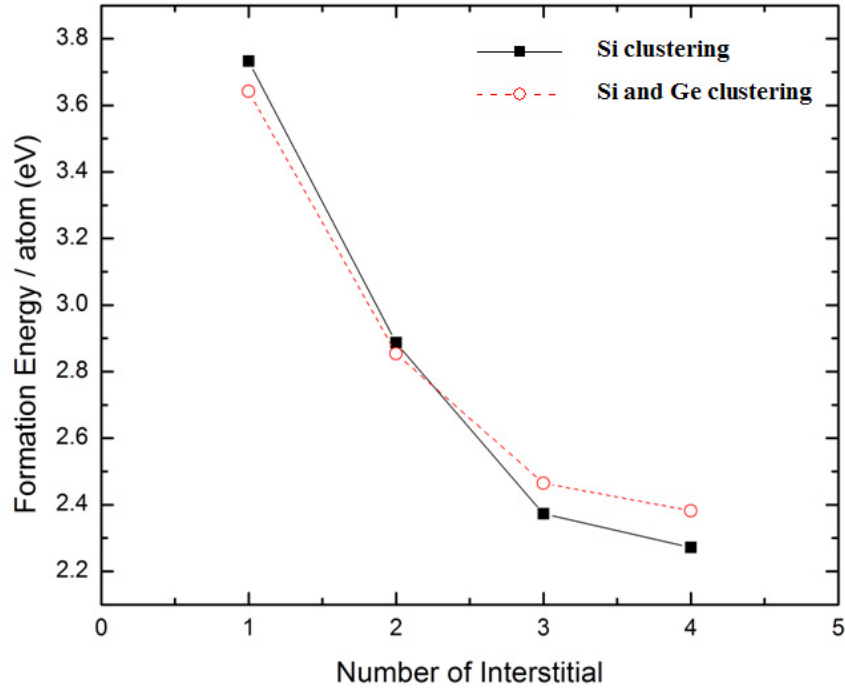
FIGURE 4.5: The formation energy per atom in the cluster (not shown in compact I_3). These are two extreme cases where additional Ge atoms are placed in the system. Solid black line shows a Si cluster with a substitutional Ge. Dashed red line shows a Si-Ge complex clustering with no substitutional Ge.

Si-clustering without Ge atom is favorable in the extended configuration while Si-Ge complex clustering prefers to the compact configuration. As a result, Si-Ge dumbbell will trap a mobile Si^I available for {311} extended defects or dislocation loops and in turn reduce the overall density of Si extended defects. In addition, the localization of Si^I

by a small clustering will open a possibility to sink into the interface during damage annealing. From the above discussion, we have shown one of possible explanations for a boron retardation by small clustering effects in the presence of Ge.

4.3 SUMMARY

In summary, a DFT-based first principles calculation to investigate the boron diffusion retardation in the presence of Ge was performed. First, the concentration of Ge-B pair is smaller than that of Si-B pair due to a lower binding energy of BI pair and higher migration energy of Ge^I. Second, the diffusing direction of Si-B pair will prefer to be in the directions where substitutional Ge atom doesn't exist, resulting in a slow diffusion process of Si-B pair with higher Ge concentrations. Third, Si-Ge dumbbell will trap mobile Si^I available for {311} extended defects or dislocation loops and in turn reduce the overall density of Si extended defects. Moreover, the localization of Si^I by small clusters will open a possibility to segregate at the interface during damage annealing. The underlying mechanism we present in this work should contribute to developing an improved physical model for highly p-type ultrashallow junction transistors.

4.4 REFERENCE

[1] The International Technology Roadmap for Semiconductors (ITRS 2003)

[2] K. Ismail, S. F. Nelson, J. O. Chu, and B. S. Meyerson, Appl. Phys. Lett., **63**, 660 (1993).

[3] Y. Yeo, Q. Lu, T. King, C. Hu, T. Kawashima, M. Oishi, S. Mashiro, and S. Sakai, Proc of IEDM, p32.5.1 (2000).

[4] K. Rim, J. Chu, H. Chen, K. Jenkins, T. Kanarsky, K. Lee, A. Mocuta, H. Zhu, R. Roy, J. Newbury, J. Ott, K. Petrarca, P. Mooney, D. Lacey, S. Koester, K. Chan, D. Boyd, M. Ieong, and H. Wong, Symp. on VLSI Tech. Dig., 98 (2002).

[5] S. Olsen, A. O'Neill, L. Driscoll, K. Kwa, S. Chattopadhyay, A. Waite, Y. Tang, A. Evans, D. Norris, A. Cullis, D. Paul, D. Robbins, IEEE Trans. Electron Devices, **50**, 1961 (2003).

[6] J. Fossum and W. Zhang, IEEE Trans. Electron Devices, **50**, 1042 (2003).

[7] P. Thompson and R. Crosby, J. Vac. Sci. Technol. B, **22**, 2333 (2004).

[8] A. Satta, E. Simoen, T. Clarysse, T. Janssens, A. Benedetti, B. De Jaeger, M. Meuris, and W. Vandervorst, Appl. Phys. Lett., **87**, 172109 (2005).

[9] V. Moroz, Y. Oh, D. Pramanik, H. Graoul, and M Foad, Appl. Phys. Lett., **87**, 051908 (2005).

[10] A. Paine, M. Morookz, A. Willoughby, J. Bonar, P. Phyillps, M. Dowsett, and G. Cooke, Mater. Sci. Forum 196-201, 345 (1995).

[11] P. Kuo, J. Hoyt, J. Gibbons, J. Turner, R. Jacowitz, and D. Lefforge, Mater. Res. Soc. Symp. Proc., **379**, 373 (1995).

[12] S. Uppal, A. Willoughby, J. Bonar, A. Evans, N. Cowern, R. Morris, and M. Dowsett, Physica B, 308-310, 525 (2001).

[13] N. Cowern, P. Zalm, P. Sluis, D. Gravesteijn, and W. Boer, Phys. Rev. Lett., **72**, 2585 (1994).

[14] P. Kuo, J. Hoyt, J. Gibbons, J Turner, and D. Lefforge, Appl. Phys. Lett., **66**, 580 (1995).

[15] N. Moriya, L. Feldman, H. Luftman, C. King, J. Bevk, and B. Freer, Phys. Rev. Lett., **71**, 883 (1993).

[16] A. Willoughby, A. Evans, P. Champ, K. Yallup, D. Godfrey, and M. Dowsett, J. Appl. Phys.,. **59**, 2392 (1986).

[17] L. Wang, P. Clancy, and C. Murthy, Phys. Rev. B, **70**, 165206 (2004).

[18] G. Kresse and J. Hafner, Phys. Lett. Rev., **47**, 558 (1993).

[19] J. Perdew, K. Burke, and M Ernzerhof, Phys. Rev. Lett., **77**, 3865 (1996).

[20] J. Jeong and A. Oshiyama, Phys. Rev. B, **64**, 235204 (2001).

[21] C. Rafferty, G. Gilmer, M. Jaraiz, D. Eaglesham, and H. Gossmann, Appl. Phys. Lett., **68**, 2395 (1996).

[22] N. Arai, S. Takeda, and M. Kohyama, Phys. Rev. Lett., **78**, 4265 (1997).

[23] J. Kim, F. Kirchhoff, J. Wilkins, and F. Khan, Phys. Rev. Lett., **84**, 503 (2000).

[24] G. Lopez and V. Fiorentini, Phys. Rev. B, **69**, 155206 (2004).

CHAPTER 5: ROLE OF BORON TED AND SERIES RESISTANCE IN HIGH-K METAL GATE SILICON-GERMANIUM PMOSFETS

5.1 INTRODUCTION

Since high-k/metal gate stacks have been successfully implemented in CMOS technology, alternative channels, such as SiGe and GaAs, have gained attention as a way to overcome roadblocks to performance enhancement [1-4]. SiGe devices are widely accepted as a performance booster in pMOSFETs because of their high hole mobility and good Si-based process compatibility.

So far, however, few systematic studies have been reported that address the physical mechanisms of boron diffusion in strained SiGe/Si heterojunction layers with different SiGe layer thicknesses and Ge content (>50%), especially with high temperature annealing [5-7]. In addition, the effects of fluorine incorporated during BF_2 implant on boron diffusion should be investigated to provide more insight into short channel device design. In this study, we investigate how short channel margins are affected by Ge mole fraction and SiGe layer thickness in a compressively strained SiGe/Si heterojunction PMOS during high temperature annealing. The role of fluorine in the short channel performance and reliability are also addressed.

5.2 EXPERIMENTAL DETAILS

A compressively strained SiGe/Si channel and source/drain (S/D) PMOS was fabricated by a standard 45nm gate-first CMOS flow (Fig.5.1) in collaboration with SEMATECH. A silicon capping layer was used for the compressively strained SiGe/Si channel and S/D PMOS. A control PMOS with a Si channel was also fabricated. To study Ge effects on boron diffusion, epitaxial SiGe was grown by ultrahigh vacuum chemical

vapor deposition (UHVCVD) using Si_2H_6 and GeH_4 on an n-type Si substrate with shallow trench isolation [8,9]. The thickness of the epitaxial SiGe layers ranged from 5nm~30nm and the Ge concentration ranged from 0~50%; the layers deposited were based on the critical thickness to control defects such as misfit dislocations as well as to minimize strain relaxation [10]. The implanted B profiles were characterized using secondary ion mass spectroscopy (SIMS).

In designing short channel pMOSFETs, devices with and without Ge PAI were fabricated with a BF_2 or B lightly doped drain (LDD). Detailed split conditions are summarized in Table 5.1. All samples received the same spike anneal at 1070^oC to maintain compatibility with Si CMOS processing.
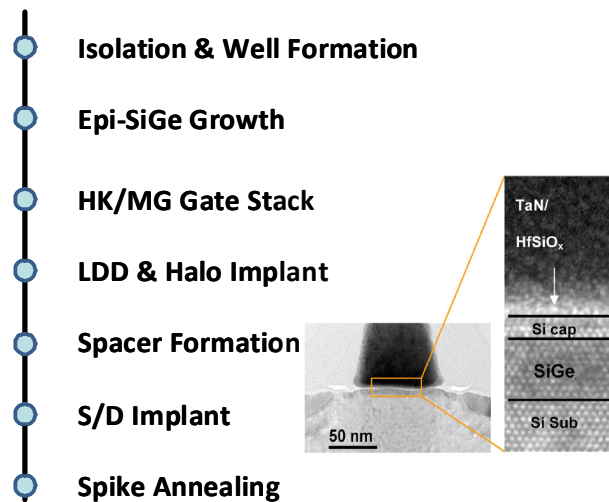
FIGURE 5.1: Process flow for SiGe pMOS fabrication and TEM image of a final device structure

TABLE 5.1: Sample split conditions

	t_{SiGe}	Ge %	Ge PAI	LDD
CON	x	x	x	
Group1	5nm ~ 30nm	25% ~ 50%	X	BF$_2$
Group2	5nm	25%	X	BF$_2$
				B
			O	BF$_2$
				B

5.3 EFFECTS OF SILICON-GERMANIUM THICKNESS AND GERMANIUM CONCENTRATION

Fig. 5.2 shows boron profiles in the Si and SiGe/Si substrates. For as-implanted profiles, both samples exhibit similar profiles and junction depths. For a longer annealing time at the same temperature, the B profile in the SiGe/Si become deeper, which is attributed to enhanced boron diffusion because B is less soluble in SiGe. Simulated boron profiles and junction depths using our calibrated simulation model matched the boron profiles and junction depths from SIMS analysis well (Fig. 5.3 and 5.4).

When the Ge concentration is increased, the threshold voltage (V_{th}) roll-off and drain-induced barrier leakage (DIBL) become more significant as shown in Fig. 5.5. For different SiGe thicknesses, V_{th} roll-off and DIBL degrade when t_{SiGe} increases (Fig. 5.6).

Table 5.2 and Fig. 5.7 exhibit simulated doping profiles and junction depths for different Ge concentrations and SiGe thicknesses. When the SiGe is thicker, the junction depth becomes deeper and the lateral diffusion of boron in the Si layer increases. The x_j and lateral diffusion are more significant when the Ge concentration increases. The

72

reason for these deeper x_j and increased later diffusion is that the solubility of B in SiGe is less soluble. The dopant concentration beyond the solubility limit can be ejected from the SiGe layer and enhance boron diffusion in Si. Therefore, a thicker SiGe layer can release more boron, resulting in deeper x_j. A greater Ge concentration also accelerates boron diffusion in Si because the boron is less soluble. These results can explain the V_{th} roll-off and DIBL in Fig. 5.5 and 5.6. Therefore, the optimum SiGe layer thickness and Ge concentration for short channel designs is <5nm and 25%, respectively. In terms of thermal stability, 25% SiGe is compatible with Si-based CMOS processes.
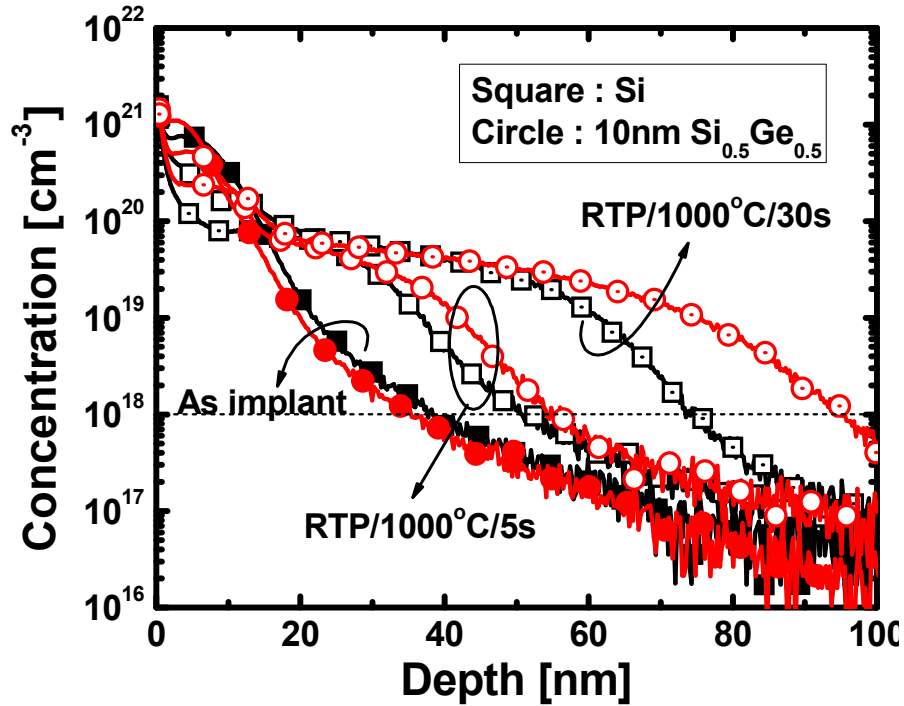
FIGURE 5.2: Boron profile in Si and SiGe/Si substrate
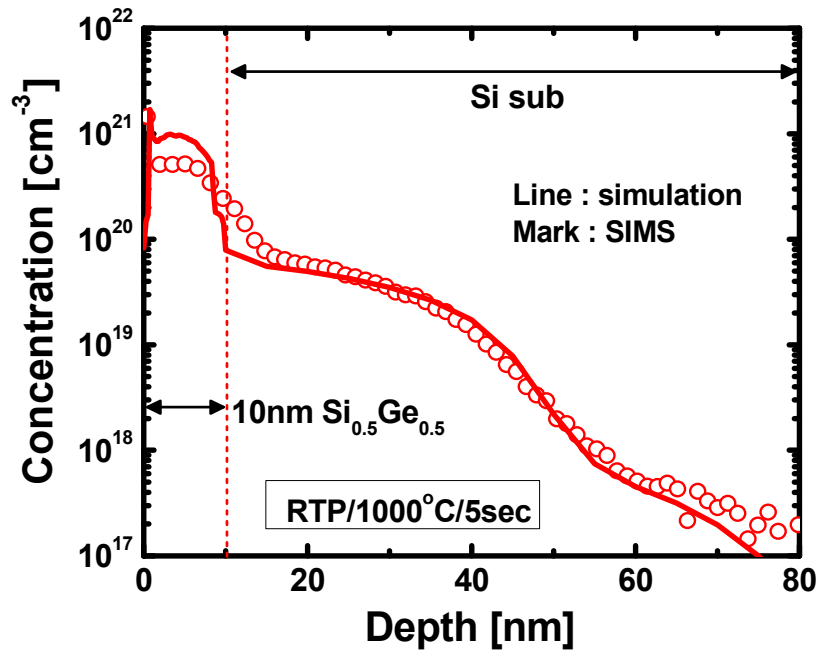
FIGURE 5.3: Process simulation compared to experimental SIMS profile.
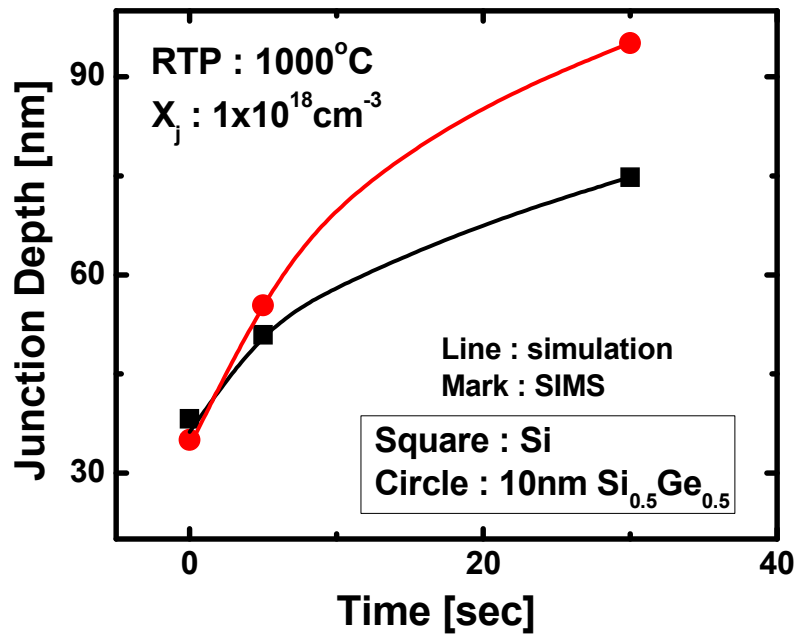
FIGURE 5.4: Simulated and measured junction depth as a function of anneal time.
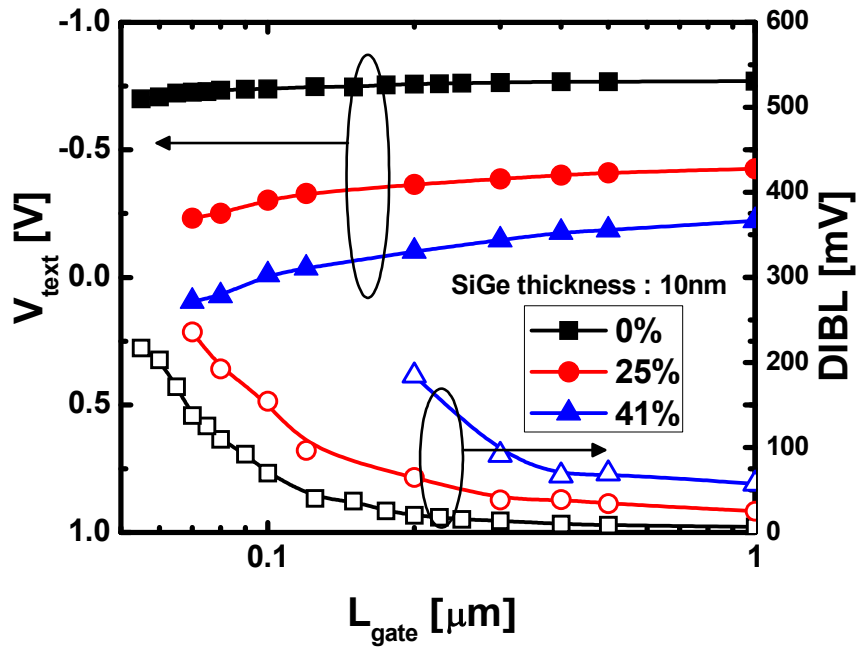
FIGURE 5.5: V_{th} and DIBL for various Ge concentration. With increasing Ge %, short channel margin become smaller.
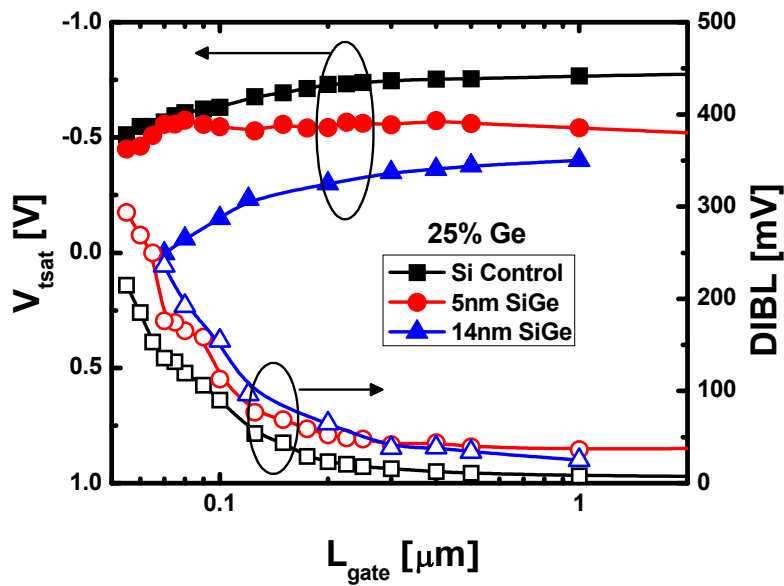
FIGURE 5.6: Effect of SiGe thickness on V_{th} and DIBL. With increasing SiGe layer, V_{th} roll-off and DIBL become worse.
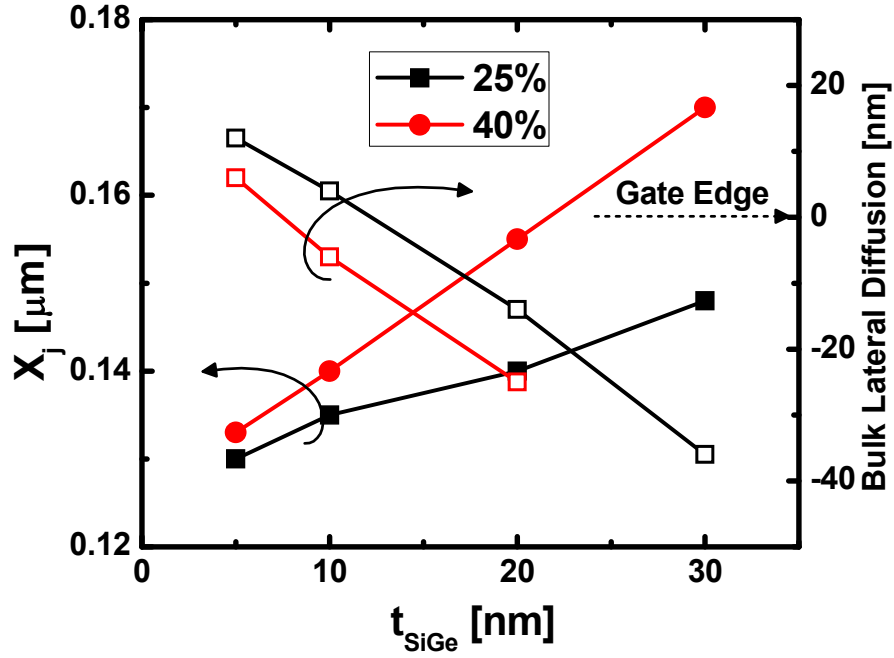
FIGURE 5.7: With increasing SiGe thickness and Ge concentration, X_j and bulk boron lateral diffusion become greater due to transient boron diffusion.

5.4 EFFECTS OF BORON DIFFUSION AND GERMANIUM PAI

For better short channel margins, we need to pay more attention to controlling the LDD boron profile because the 5nm thickness SiGe layer exhibits greater DIBL than the Si control devices. Ge PAI and different dopant splits (BF_2 and B) were used for device fabrication (Table 5.1). All split conditions show a similar range of equivalent oxide thickness (EOT) and interface trap density (N_{it}) (Fig. 5.8, and 5.9). Hole mobility improved 2.5x in all SiGe devices as shown in Fig. 5.10. For short channel device margins, Ge PAI devices exhibit better DIBL than devices without PAI (Fig. 5.11). Devices with a B LDD and Ge PAI show the best short channel margins among the split conditions. For devices with Ge PAI, improved drain breakdown voltage (BVDSS) was

76

observed because of the better short channel margin (Fig. 5.12). These improved short channel margins resulted in better I_{on} at given DIBL and I_{on}-I_{off} characteristics (Fig. 5.13 and 5.14).

While the Ge PAI technique is effective with both BF_2 and B implants, the reason for the better short channel margin in B LDD devices both with and without Ge PAI is fluorine effect. A previous study found fluorine can enhance boron diffusion within amorphous Si when the F implant was performed separately [11]. Thereby, fluorine-induced B diffusion is mitigated for BF_2 implanted sample.

In terms of reliability, SiGe devices show less V_{th} shift at a given negative bias temperature instability (NBTI) stress while all samples show similar power-law dependence as seen in Fig. 5.15 and 16. Fluorine from the BF_2 implant helps improve NBTI immunity. The BF_2 LDD with Ge PAI structures exhibit better NBTI immunity (less ΔV_{th} and ΔG_{mmax}), which suggests that Ge PAI may help retain more residual fluorine.

TABLE 5.2: 2D doping profile of various SiGe thickness and Ge concentration

C_{Ge}\t_{SiGe}	5nm	10nm	20nm
25%			
40%			
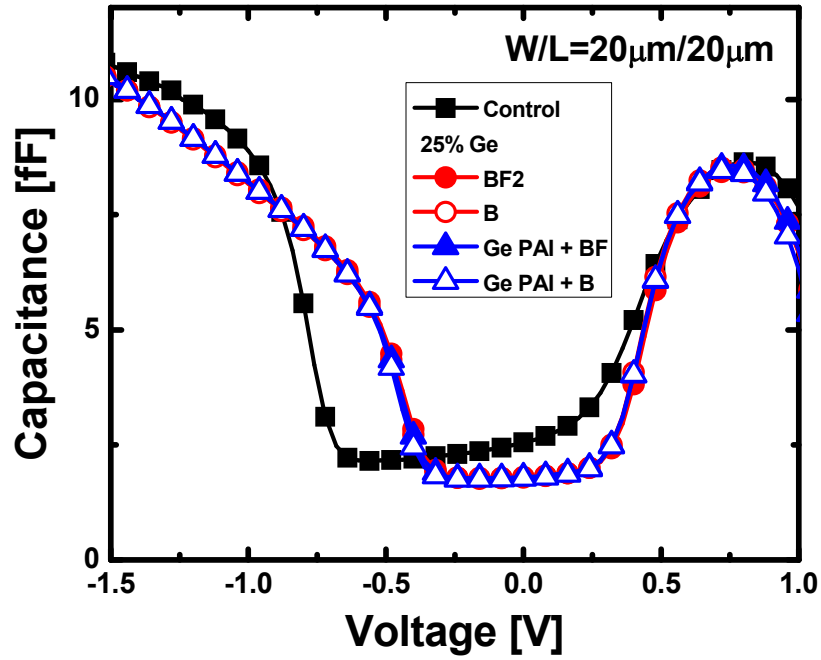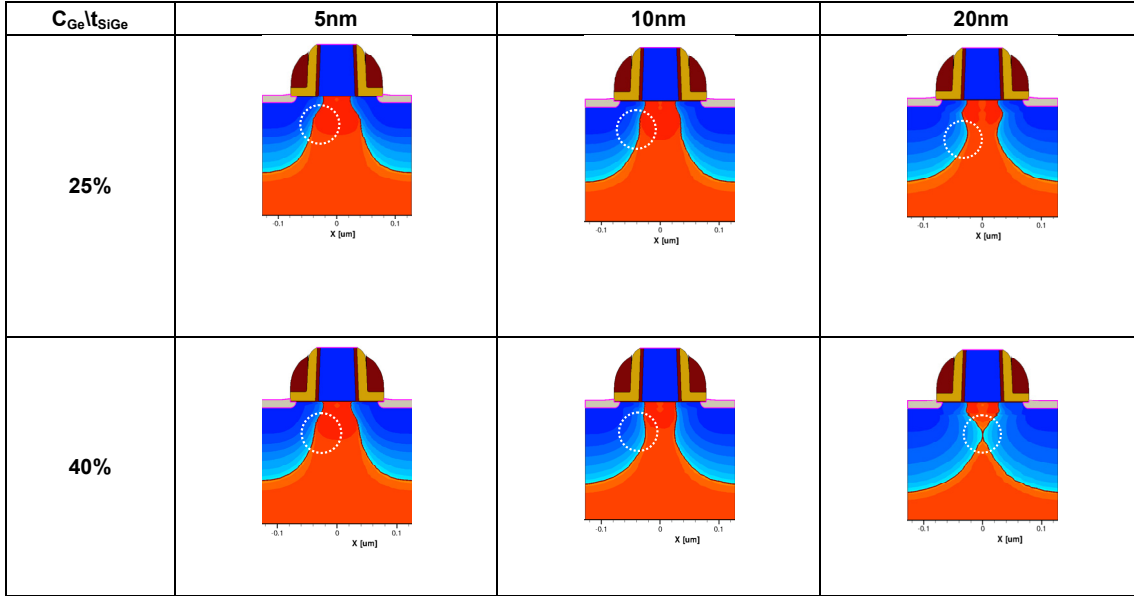
FIGURE 5.8: All sample devices show similar EOT (=1.1nm).
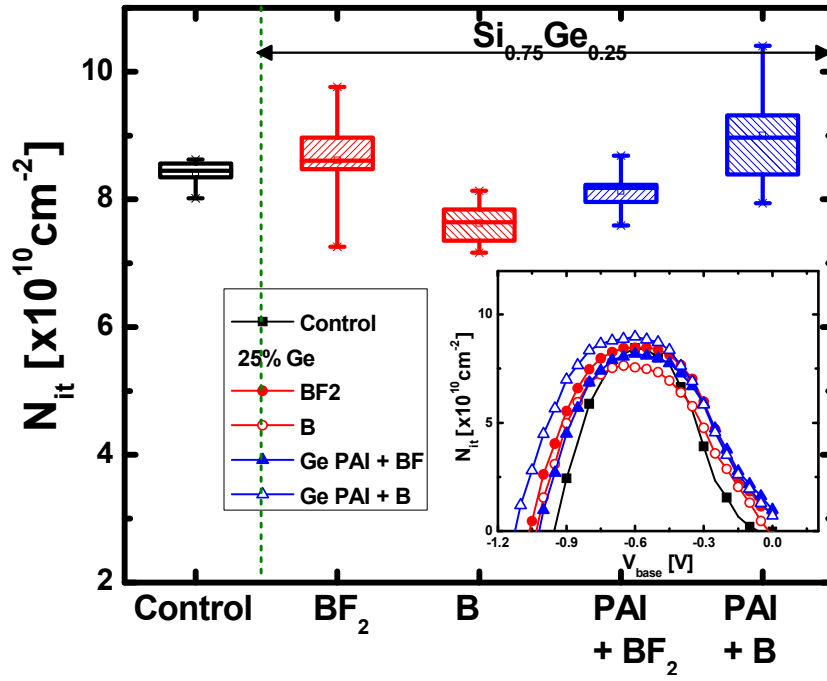
FIGURE 5.9: All sample device exhibit similar N_{it}.
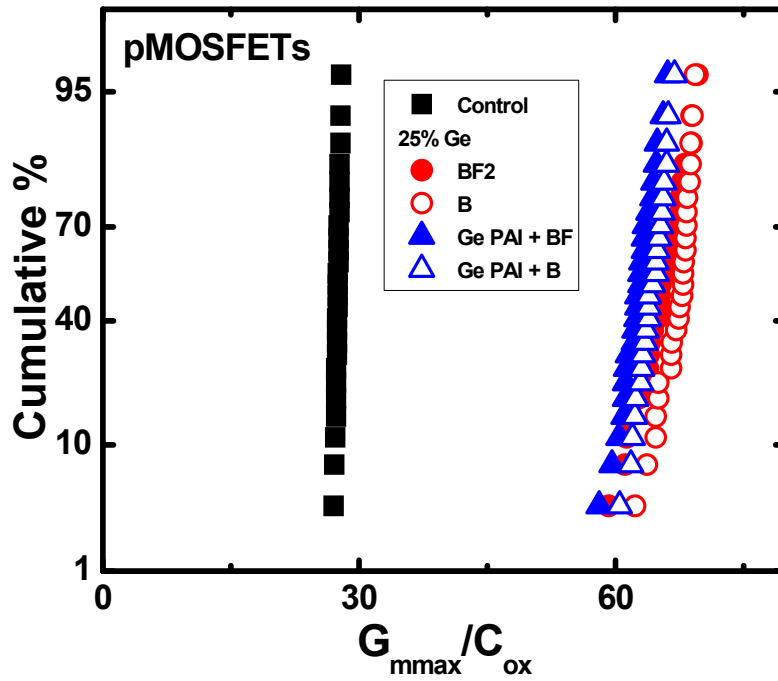
FIGURE 5.10: 2.5x mobility enhancement for SiGe devices compared to the Si control devices.
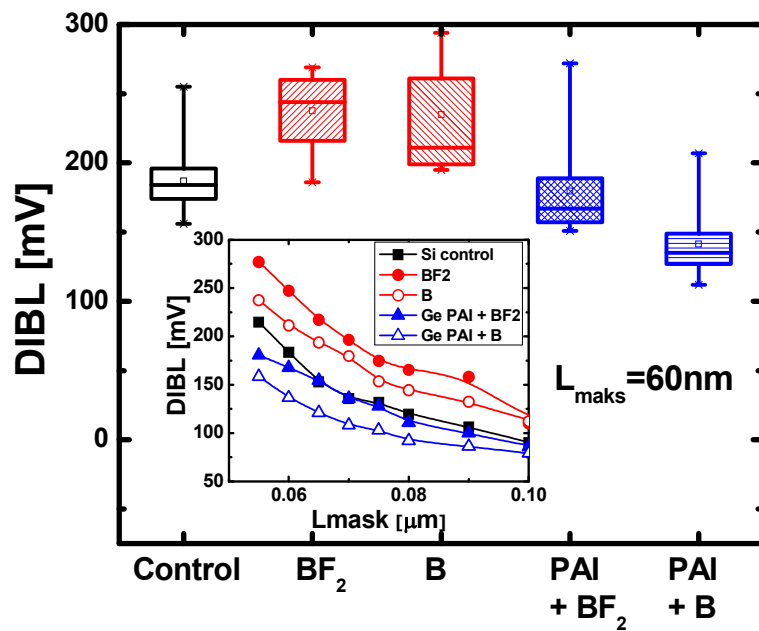
FIGURE 5.11: With Ge PAI, DIBL become less compared to w/o Ge PAI. Boron LDD exhibits lower DIBL indicating improved short channel margin.
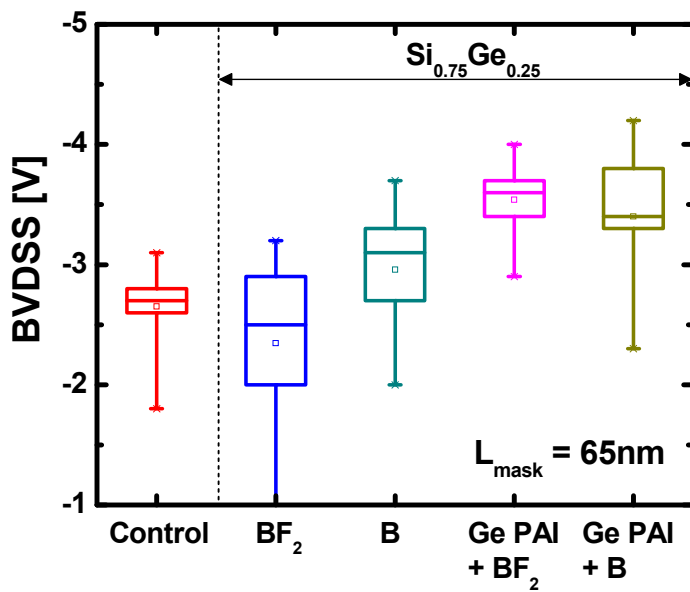
FIGURE 5.12: Germanium PAI samples show improved BVDSS compared to the control and w/o PAI devices.
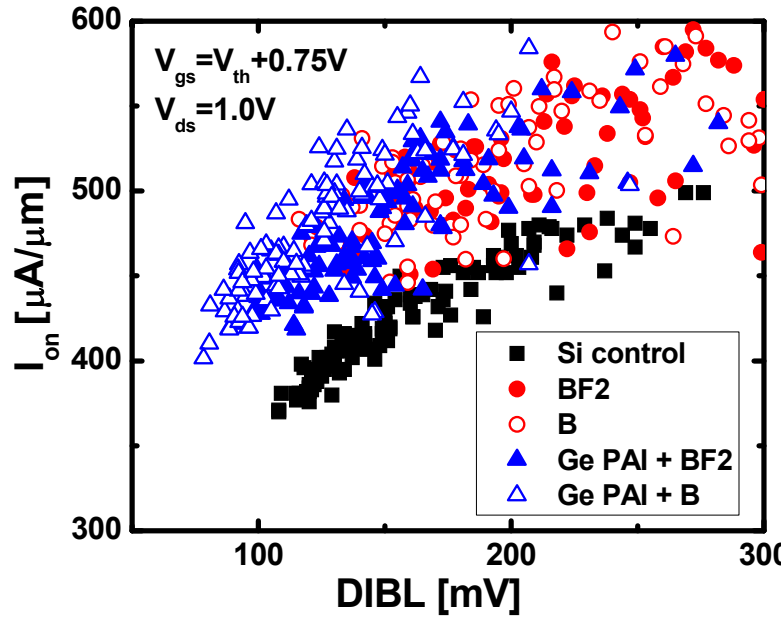
FIGURE 5.13: SiGe devices exhibit improved output characteristics at a given DIBL. PAI + B LDD show the best result.
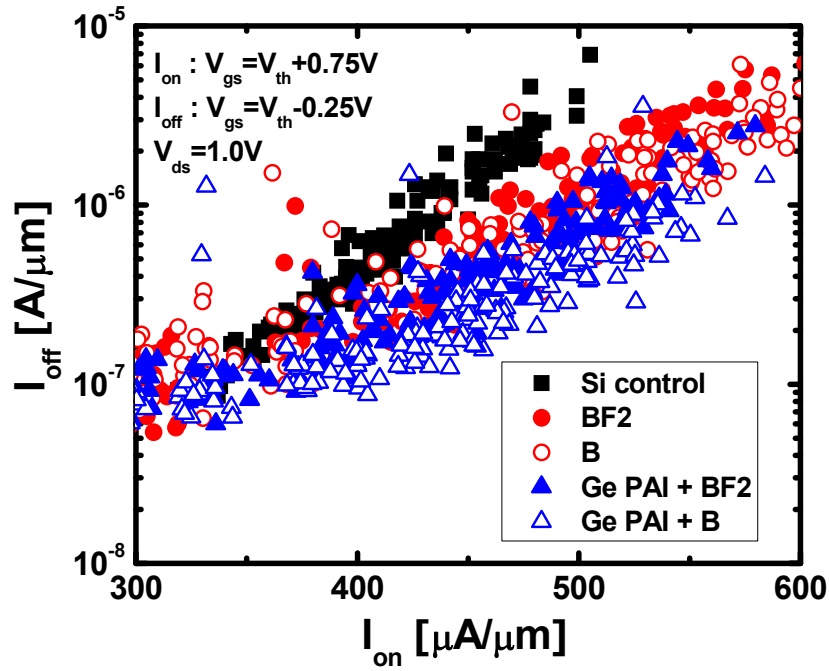
FIGURE 5.14: Due to improved short channel margin, Ge PAI devices exhibit highest Ion at I_{off}=200nA/μm.
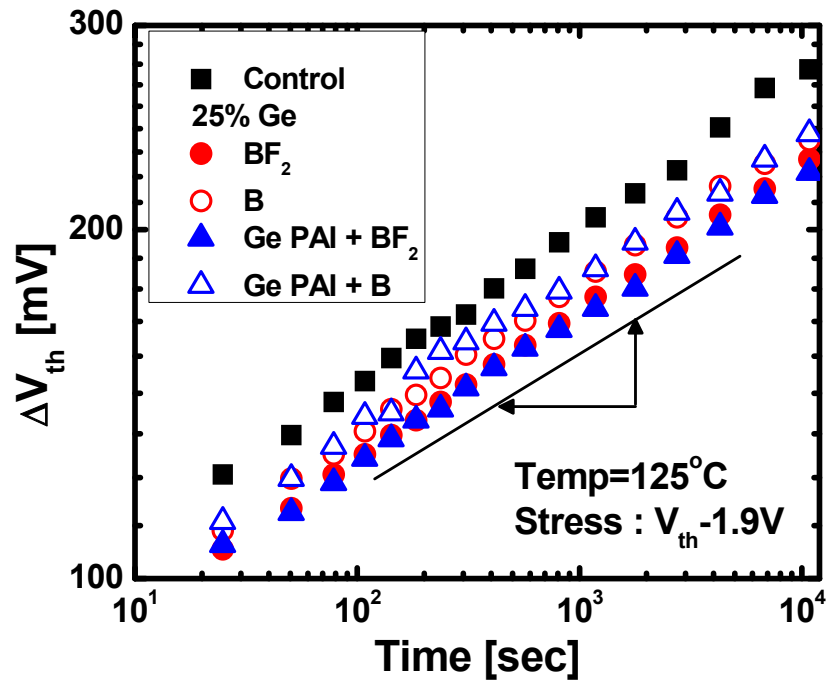
FIGURE 5.15: All BF$_2$ implanted samples show less V$_{th}$ shift due to fluorine effect. All samples show a similar slope.
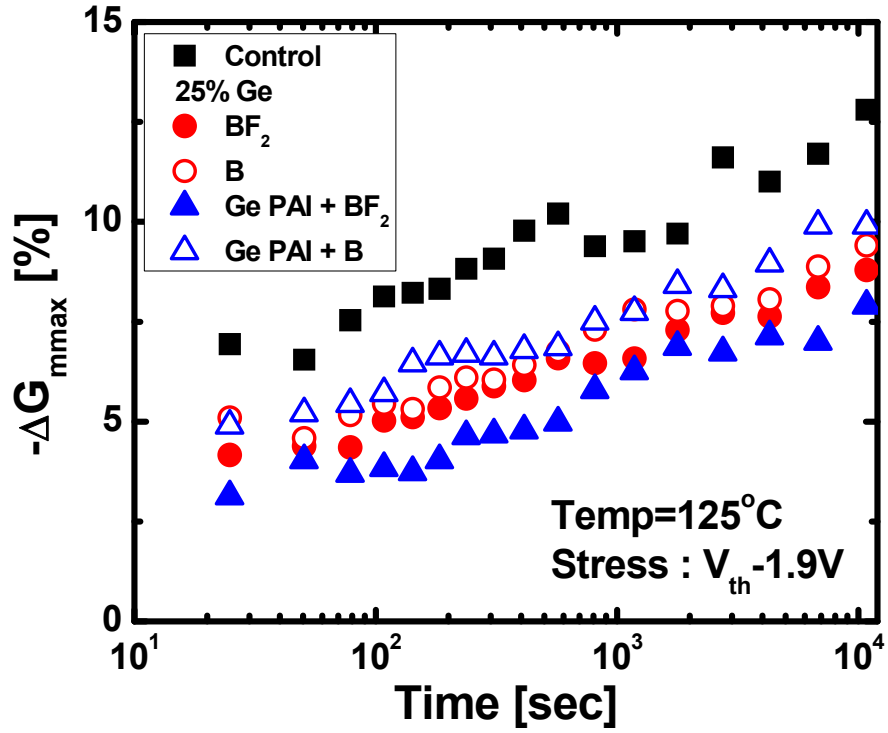
FIGURE 5.16: Germanium PAI may help retain more residual fluorine resulting in less G_m degradation.

5.5 SUMMARY

A systematic study was performed to understand the mechanism of boron diffusion in SiGe/Si substrates. To improve the short channel margins, SiGe thickness and Ge concentration should be carefully selected. In a given SiGe/Si substrate, Ge PAI can improve the short channel behavior because boron diffusion is mitigated. There is a trade-off in terms of fluorine effects on short channel behavior and reliability characteristics.

5.6 Reference

[1] T. Ghani, et al., in IEDM Tech. Dig., 1161 (2003)

[2] A. G. O'Neill et al., IEEE Trans. Electron Devices 43, 911 (1996)

[3] K. Rim, et al., IEEE Trans. Electron Devices **47**, 1406 (2000)

[4] S. Lee, et al., IEEE Electron Device Lett. **29**, 1017 (2008)

[5] J. Park, et al., Appl. Phys. Lett. **74**, 1248 (1999)

[6] N. E. B. Cowern, et al., Appl. Phys. Lett. **86**, 101905 (2005)

[7] G. Impellizzeri, et al., Appl. Phys. Lett. **91**, 132101 (2007)

[8] B. Anthony, et al., Elec. Mat. **19**, 1027 (1990)

[9] C. Li, S. John, et al., J. Vac. Sci. Tech. A **14**, 170 (1996)

[10] R. People et al., Appl. Phys. Lett. **47**, 322 (1985)

[11] J. M. Jacques, et al., Appl. Phys. Lett., **82**, No. 20 p. 3469, (2003)

CHAPTER 6: ANALYSIS FOR PERFORMANCE DEGRADATION FACTORS IN SILICON-GERMANIUM AND GERMANIUM NMOSFETS

6.1 INTRODUCTION

High mobility materials to replace Si channels have increasingly been studied to realize high performance metal oxide-semiconductor field effect transistors (MOSFETs) for the next generation CMOS technology [1]. Germanium has been considered as a promising candidate for an alternative channel material because of its lower effective conductivity mass for both electron and hole compared to silicon as well as a higher source injection velocity for alleviating the problem of MOSFET drain current saturation [2-5]. However, Ge MOSFETs have not been widely deployed because high quality Ge native oxide for gate dielectric materials and surface passivation is not successfully implemented [6]. The degraded carrier mobility has been one of the major challenges that have postponed the implementation of high-k gate dielectrics to replace SiO_2 for the scaled Si CMOS technology [7, 8].

Recently, Ge p-channel MOSFET (pMOSFETs) with various high-k dielectric materials and surface passivation methods has been demonstrated with improved hole mobility over SiO_2/Si counterpart [9, 10]. Either Si passivation or thin GeO_2 passivation makes it possible to be about three times peak hole mobility over SiO_2/Si universal mobility [9, 10]. However, Ge n-channel MOSFETs (nMOSFETs) with high-k gate dielectrics still show much lower electron mobility than SiO_2/Si universal mobility curve [3, 10-13]. It is still not fully understood why Ge nMOSFETs suffer from this severe mobility degradation; Coulomb scattering, remote phonon scattering, and charge trapping have been proposed to be primarily responsible [14-17], but in order to achieve high

performance SiGe and Ge nMOSFETs, it is evident that interface traps should be minimized in a high-k gate stack on SiGe and Ge.

A clear correlation between the interface trap density and inversion layer mobility for Ge nMOSFETs has not been necessarily observed. A good interface quality was reported with highest recorded hole mobility, however, Ge nMOSFETs still exhibit low electron mobility. Even in a relatively low interface trap density D_{it} value of $4.5x10^{11}$ cm^{-2} eV^{-1}, electron mobility with less than half of SiO_2/Si universal value was reported [18]. One possible explanation is that although D_{it} is relatively low at midgap of germanium, a high density of interface traps might be present in the upper half of the Ge bandgap near the conduction band and behave like Coulomb scattering centers when the device is under strong inversion. This kind of asymmetric D_{it} distribution for high-k/Ge interface has been reported based on Ge MOS capacitors by using conductance method under low temperatures [19-23]. However, there is still no direct evidence that either symmetric or asymmetric interface trap distributions in valence and conduction band affect the performance degradation; otherwise, high average concentrations of interface traps in the bandgap are a dominant factor for Ge nMOSFETs.

Moreover, for conventional self-aligned Ge MOSFETs fabrication, the gate stack must maintain its integrity throughout the source/drain (S/D) junction which is required to have high dopant activation and less dopant diffusion without a significant amount of defects in the depletion region. Ge nMOSFETs pose a particular fabrication challenge. There is relatively small process window to achieve both a stable gate stack and a well-activated n$^+$ S/D because of the low dopant solubility in Ge and fast dopant diffusion during activation. In order to achieve a high performance Ge nMOSFET, it is required that the impact on electrical characteristics due to high interface traps originated from

high-k dielectrics and surface passivation as well as junction properties such as the S/D series resistance and band-to-band tunneling should be investigated.

In this work, we investigate the interface traps with charge pumping measurements at room temperature for Si, SiGe, and Ge MOSFETs. TCAD device simulation is also performed to evaluate which distributions of interface traps will significantly affect the electrical characteristics such as flatband voltage (V_{FB}) shift and threshold voltage (V_{th}) shift based on capacitance-voltage (CV) and current-voltage (IV) curves [24]. n^+/p and p^+/n diodes are studied in order to decouple the electrical characteristics from the gated-diode (GD) MOSFETs. With an extraction of S/D series resistance from various channel lengths, we propose the possible reasons for performance degradation in SiGe and Ge nMOSFET together with simulation results.

6.2 DEVICE FABRICATION

Si, SiGe, and Ge MOSFETs are fabricated by a standard gate-first CMOS flow. Shallow trench isolation (STI) is first formed on Si (100) substrate. Well implant is done for n- and p-type well formation on Si substrate with a conventional activation annealing. SiGe (Ge 40%) and Ge epitaxial layers are selectively grown on STI-formed Si substrates using rapid thermal chemical vapor deposition. With a high selectivity, SiGe and Ge layers are selectively grown on Si substrates with no nucleation on STI regions. The thickness for SiGe and Ge epitaxial layers is greater than the critical thickness and the strain in the epitaxial film is fully relaxed [25]. The SiGe and Ge channel is undoped to reduce Coulomb scattering. To improve the interface characteristics and thermal stability of the gate stack, a 5 nm epitaxial Si cap layer is deposited on the Ge epitaxial layer for surface passivation in Ge MOSFETs. A 50 Å HfO_2 gate oxide is then deposited using

atomic layer deposition followed by sputtering of the 700 Å TaN metal gate. After gate formation, S/D regions are implanted with BF_2 into SiGe-on-Si and Ge-on-Si. The SiGe and Ge epitaxial layers are partially amorphized with BF_2 implant. Dopants are activated by rapid thermal annealing. The control process flow for Si MOSFETs is same with that for SiGe and Ge MOSFET except for the epitaxial film.

6.3 ELECTRICAL RESULTS

Normalized I_dV_g characteristics for both n- and pMOSFETs at $L_{gate}=1\mu m$ are shown in Fig. 6.1. Due to the different V_{th}, V_g-V_{th} is used for x-axis. Key transistor parameters are summarized in Table 6.1. The physical reason of V_{th} shift in both n- and pMOSFETs is attributed to valence band-offset and Ge-induced negative charges. The subthreshold slope is increased for SiGe and Ge devices, which indicates the increased interface states due to Ge. Transconductance (G_m) is increased in SiGe and Ge pMOSFETs as expected, while the G_ms for their counterparts (nMOSFETs) were decreased as reported [2, 18]. One possible explanation is asymmetric interface state distributions across the energy bandgap as proposed the previous study [13, 20-22], but their study was done by conductance measurement in MOS capacitors. Charge pumping method is known to be more straightforward way for studying the interface states. In addition, TCAD device simulation which includes various distributions of interface states is demonstrated to verify our measurement results.

88
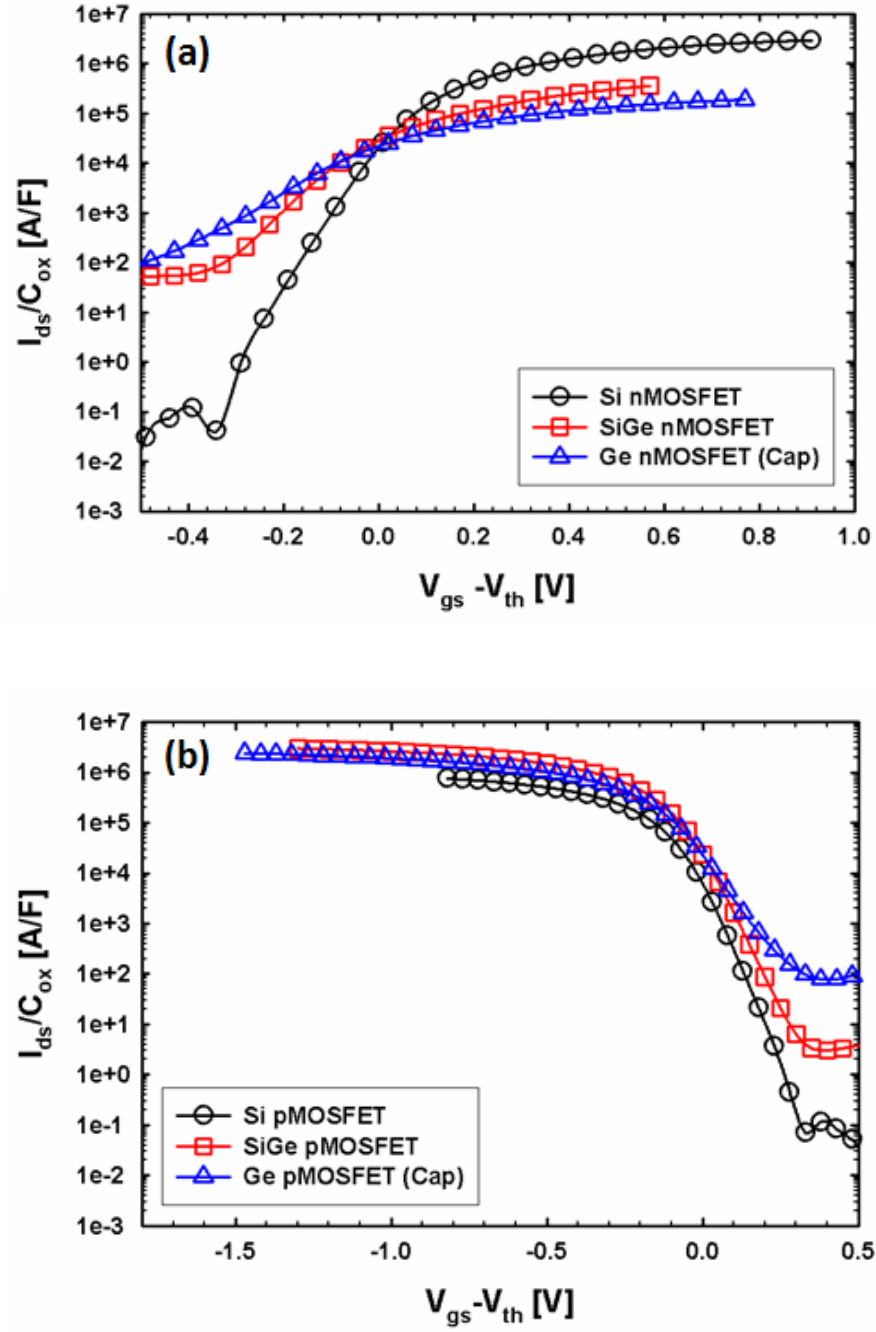
FIGURE 6.1: IdVg characteristics for 1μm channel length and 10μm width for (a) nMOSFETs and (b) pMOSFETs.

6.4 Charge Pumping Characteristics

The charge pumping (CP) technique in MOSFET has been extensively used to order to characterize the interface traps in Si/SiO$_2$ and obtain the energy distributions in the bandgap [19, 26-29]. The detailed schematic diagram for CP measurements is shown in Fig. 6.2. This technique consists in measuring the DC current due to recombination processes at the interface defects when the base level (V_{base}) with constant amplitude (V_{amp}) gate pulse from accumulation to inversion is ramped up. By measuring the charge pumping current (I_{cp}) in either substrate and drain region with variable fall and rise times with S/D regions grounded, the energy distribution of interface traps can be obtained in a relatively large part of the forbidden energy gap on both sides of midgap as shown in Eq. (6.1).

$$\frac{I_{cp}}{f} = 2qD_{it}AkT \left\{ ln\sqrt{t_f t_r} + ln\frac{|V_{fb} - V_{th}|}{|V_{amp}|} v_{th} n_i \sqrt{\sigma_n \sigma_p} \right\}, \qquad (6.1)$$

where f [Hz] is the frequency, D_{it} [cm^{-2}eV^{-1}] is interface traps, A [cm^2] is the area, v_{th} [cm/s] is thermal velocity, n_i [cm^{-3}] is the intrinsic carrier concentration , t_r [s] is rise time, t_f [s] is fall time, and σ_n [cm^2] and σ_p [cm^2] are capture cross-sections for electrons and holes, respectively.

The energy is specifically swept through the electron emission energy level ($E_{em,e}$) above midgap by changing t_f of the gate pulse while keeping t_r fixed as shown in Eq. (2) and (4) [26]. Similarly, the energy is gradually swept through the hole emission energy level ($E_{em,h}$) below midgap by changing t_r while keeping t_f fixed as shown in Eq. (3) and (5) [26].
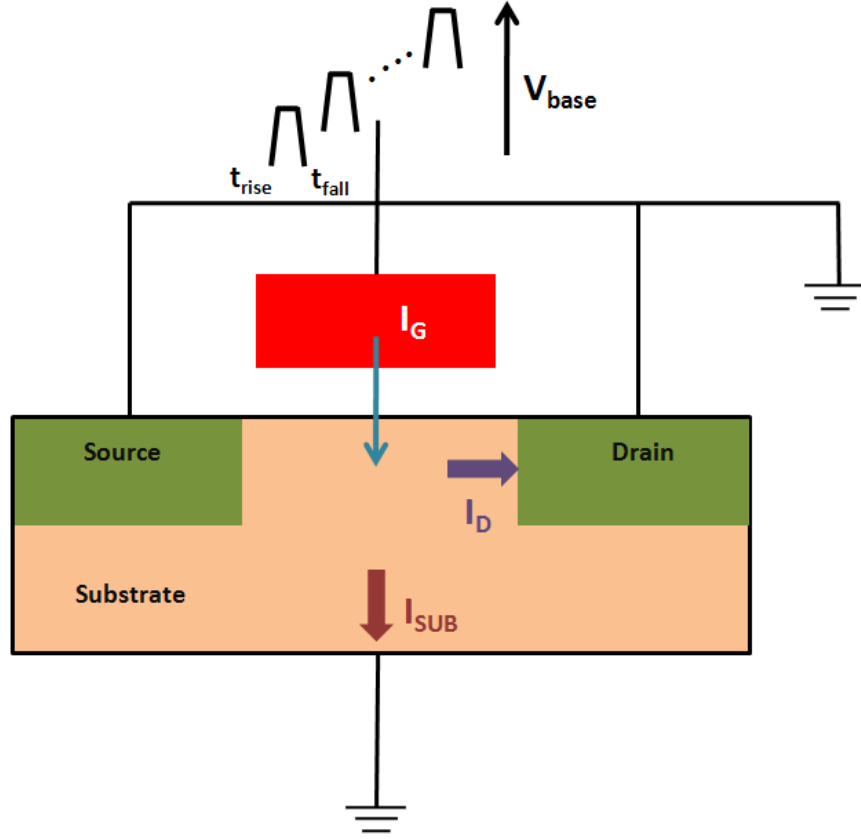
FIGURE 6.2: Schematic diagram for charge pumping technique. Square pulse with variable rise and fall time is generated with constant voltage amplitude (1V). The base voltage (V_base) is swept from accumulation region to inversion region. The recombination current due to interface traps is measured in both substrate and drain. The definition for rise and fall is shown in the schematic diagram for nMOSFETs.

$$E_{em,e} - E_i = -kTln\left(v_{th}n_i\sigma_n \frac{|V_{fb} - V_{th}|}{|V_{amp}|} t_f\right), \qquad (6.2)$$

$$E_{em,h} - E_i = -kTln\left(v_{th}n_i\sigma_p \frac{|V_{fb} - V_{th}|}{|V_{amp}|} t_r\right), \qquad (6.3)$$

$$D_{it}(E_2) = -\frac{t_f}{qAkTf}\frac{dI_{cp}}{dt_f} \quad (t_r \ constant), \qquad (6.4)$$

$$D_{it}(E_1) = -\frac{t_r}{qAkTf}\frac{dI_{cp}}{dt_r} \quad (t_f \ constant), \qquad (6.5)$$

91

It should be noted that the interface traps include all electrically active defects or charge centers such as Si interlayer/Ge heterojunctions that can respond to charge pumping signals [30, 31]. The rise/fall time dependence of charge pumping curves and the plot of I_{cp}/f vs $in[(t_r*t_f)]^{1/2}$ for Si nMOSFETs as shown in Fig. 6.3(a) and 6.3(b), respectively. The mean capture cross-section of electrons and holes $[(\sigma_n\sigma_p)^{1/2}=6.6\times10^{15}$ cm^{-2}] is obtained. The mean value of D_{it} is extracted to be 7.1×10^{10} cm^{-2}eV^{-1}. In Fig. 6.4(a) and 6.4(b), a mean cross-section of electrons and hole is 5.3×10^{16} cm^{-2} and the mean value of D_{it} is 1.2×10^{13} cm^{-2}eV^{-1} for Ge nMOSFETs.

Fig. 6.5(a) and 6(a) show a weak dependence of I_{cp} on the rise time by varying the rise time from 10ns to 1μm and keeping the fall time constant at 100ns for Si and Ge nMOSFETs. However, Fig. 6.5(b) and 6.6(b) show a strong dependence of I_{cp} on the fall time by varying the fall time from 10 ns to 1μm and keeping the rise time constant at 100ns for Si and Ge nMOSFETs. The amounts of I_{cp} dependence on variable rise and fall time indicate that the densities of interface traps can be asymmetric between the upper half and the lower half of midgap.

Fig. 6.7 shows the densities of interface traps as a function of energy in the Si bandgap as extracted from Fig. 6.5 and Fig. 6.6. The capture cross-sections for electrons and holes are assumed to be equal to extract the energy distribution. In fact, the numerical error is expected to be not significant because both of them are inside the logarithmic function in Eq. (1). The energy distribution in Ge nMOSFETs is relatively symmetric with high average value (~10^{13} cm^{-2}eV^{-1}) near midgap while higher D_{it} is obtained near conduction band edge compared to valence band edge in Si and SiGe nMOSFETs.
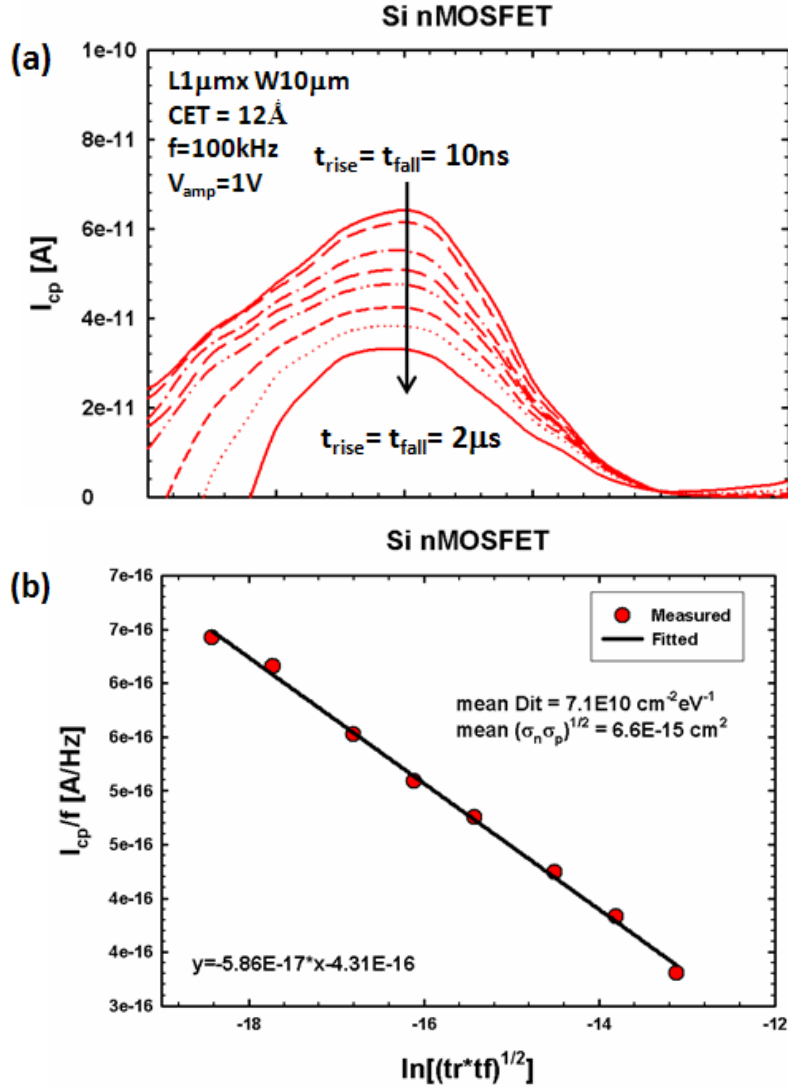
FIGURE 6.3: (a) Rise and fall time dependence of charge pumping current (Icp) for Si nMOSFETs. (b) Qcp (=Icp/f) as a function of $\ln[(tr*tf)1/2]$ in order to extract mean capture cross-section for electrons and holes as well as mean interface traps (Dit).
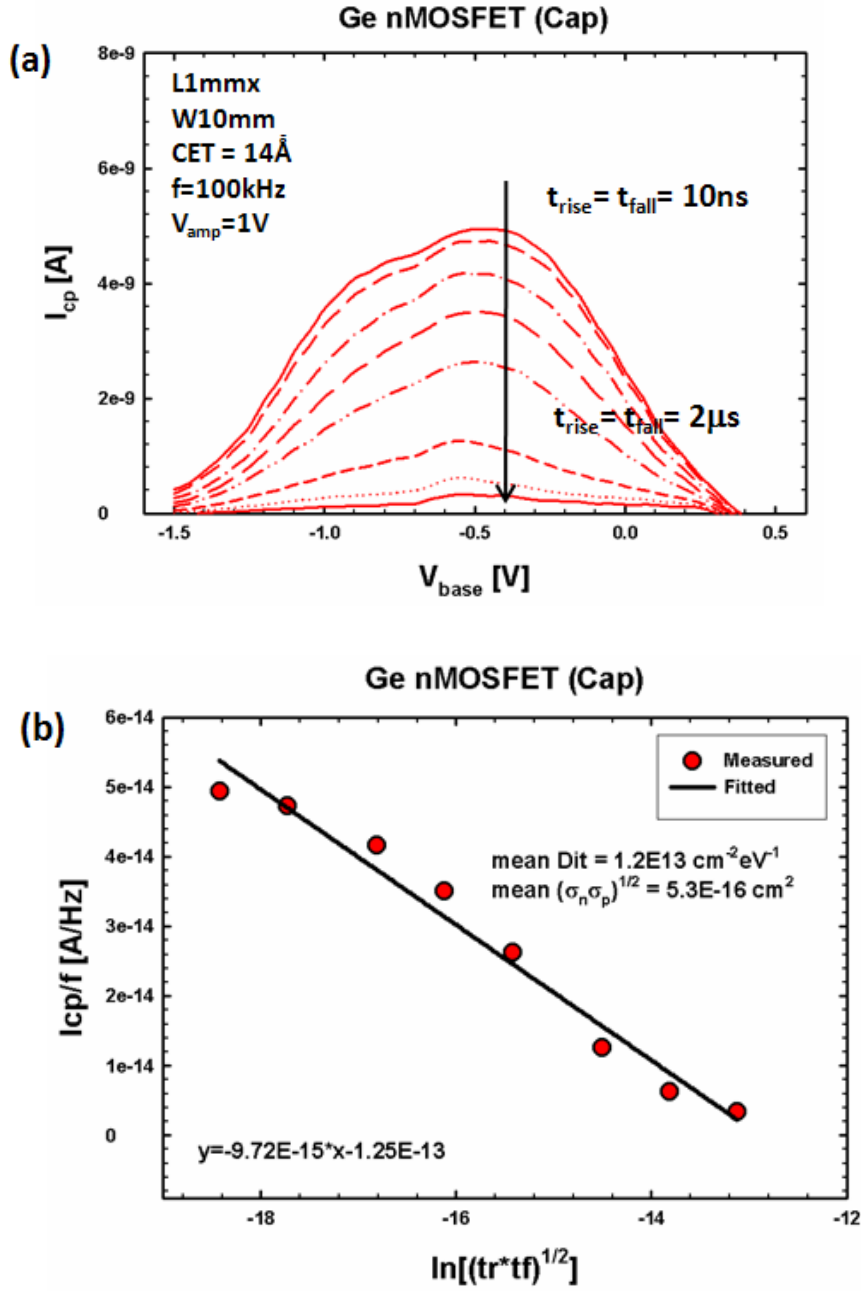
FIGURE 6.4: (a) Rise and fall time dependence of charge pumping current (Icp) for Ge nMOSFETs. (b) Qcp (=Icp/f) as a function of $\ln[(tr*tf)1/2]$ in order to extract mean capture cross-section for electrons and holes as well as mean interface traps (Dit).

94
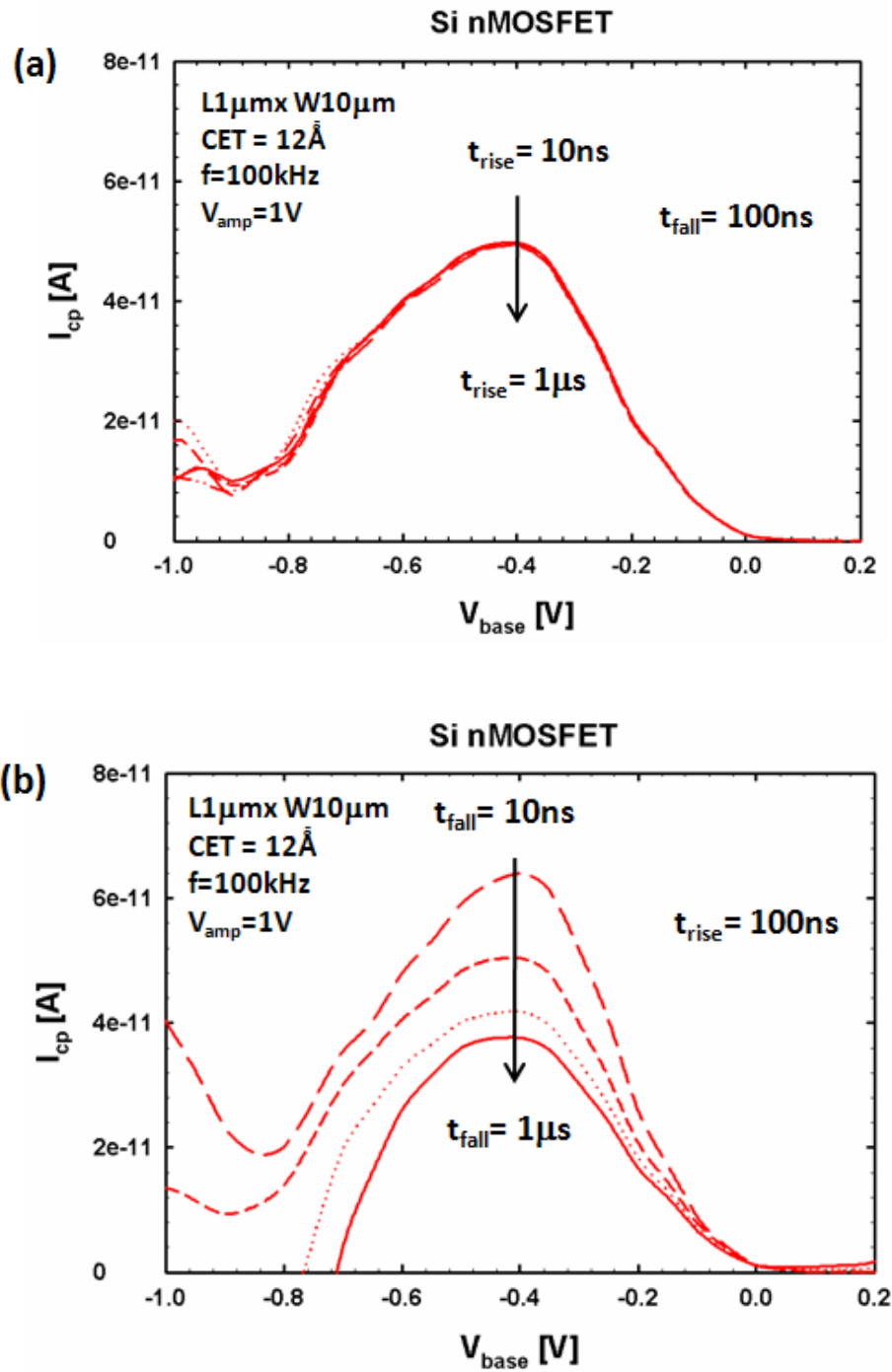
FIGURE 6.5: (a) Weak rise time dependence of charge pumping current curves and (b) Strong fall time dependence of charge pumping current curves in Si nMOSFETs.
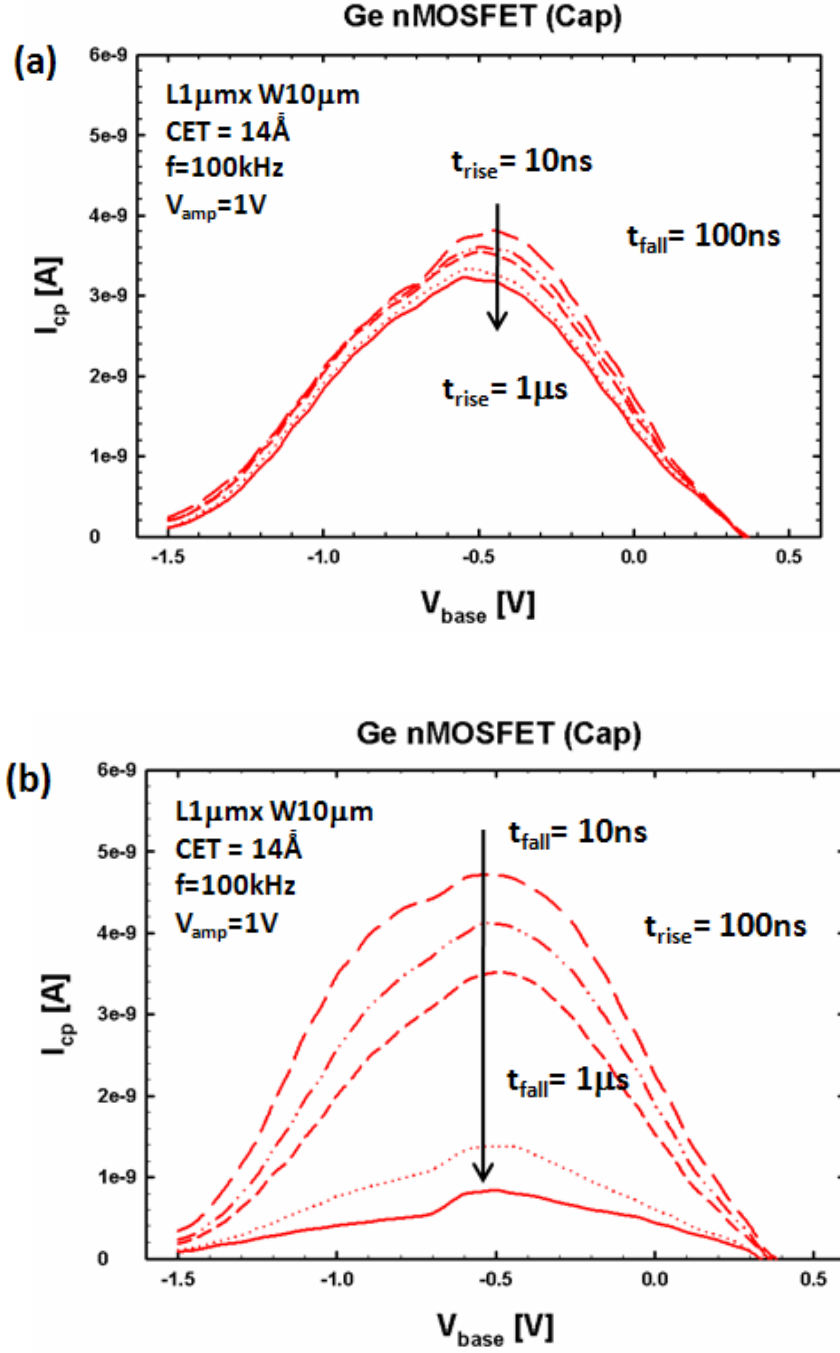
FIGURE 6.6: (a) Weak rise time dependence of charge pumping current curves and (b) Strong fall time dependence of charge pumping current curves in Ge nMOSFETs.

It should be noted that room-temperature charge pumping data do not allow for extracting D_{it} closer to the band edges because of thermal emission. D_{it} value for Ge nMOFSETs might be underestimated because Ge has a smaller bandgap than Si and interface-trap time constant for Ge are much shorter. In the meanwhile, conductance method at low temperature reported that D_{it} is to be an order of ~10^{13} cm^{-2}eV^{-1} near conduction band. However, a relatively low interface trap value of 4.5×10^{11} cm^{-2}eV^{-1} was reported for Ge nMOSFETs, but electron mobility with less than half of Si/SiO$_2$ universal was observed [18]. Considering the similar D_{it} for the Si control and the SiGe device, the G_m degradation of nMOSFETs cannot be solely explained by the interface states.
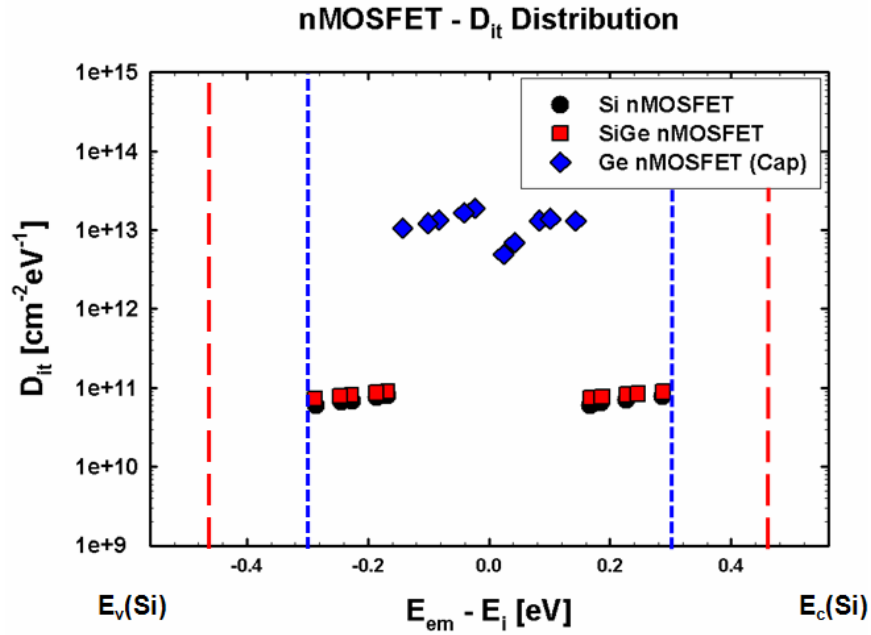
FIGURE 6.7: Energy distribution of interface traps as determined by variable rise and fall time dependence of charge pumping currents for Si, SiGe, and Ge nMOSFETs. Dotted lines (blue) and dashed lines (red) from intrinsic Fermi level are meant for valence and conduction band edges, respectively.

97
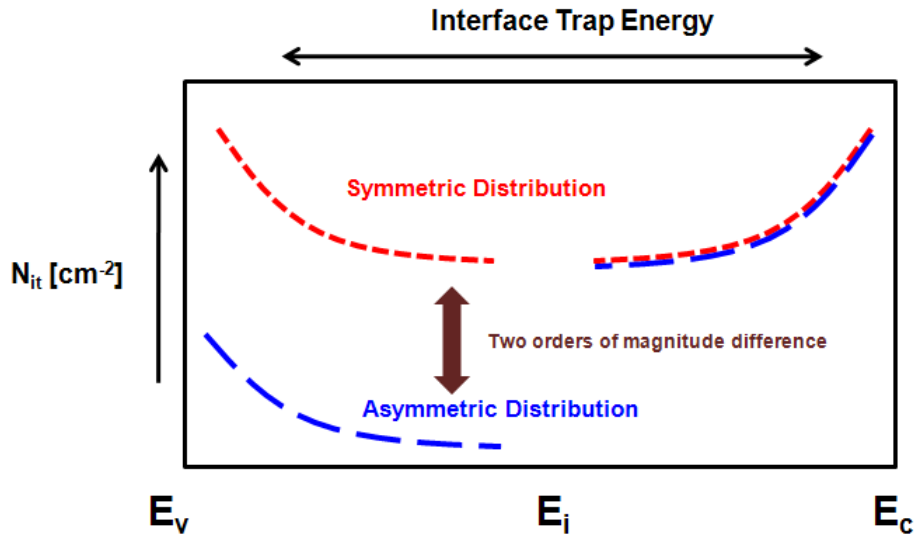
FIGURE 6.8: Schematic diagram for symmetric and asymmetric Nit distributions which are used for trap distribution inputs in TCAD device simulation. U-shaped trap distributions with a logarithmic function are assumed to have high concentrations near the band edges.

Fig. 6.8 shows a schematic diagram for interface traps in the upper half and the lower half of midgap. Interface traps are supposed to be incorporated as a logarithmic function with high densities near the band edges. TCAD device simulation is performed to obtain capacitance-voltage (CV) results for symmetric and asymmetric N_{it} distribution in SiGe n- and pMOSFETs in Fig. 6.9 and 6.10. For the symmetric N_{it} distribution, CV is stretched out in both accumulation and inversion region, while only the inversion CV in nMOSFETs and the accumulation CV in pMOSFETs is stretched out for the asymmetric interface state cases. However, the interface states in the upper band, i.e., inversion of nMOSFETs and accumulation of pMOSFETs, appear to more distort CV curves due to the energy band offset. With increasing N_{it}, V_{th} for n- and pMOSFETs is increased and

inversion charge density becomes less, which can affect transistor output characteristics. From the greater CV stretch-out in inversion of nMOSFETs, higher N_{it} is expected for Ge. Simulated transistor I_dV_g characteristics are shown in Fig. 6.11 and 6.12. As expected from CV simulation, greater S_f and high V_{th} were observed with increasing N_{it}. However, G_{mmax} did not change that much comparing to the measurement results, which cannot be explained by N_{it} alone (if this is true, SiGe & Ge n- and pMOFETs should show degraded G_m.) and indicates that there is another factor of G_{mmax} degradation, such as parasitic resistance. How the parasitic resistance affects nMOSFEFs IV simulations are performed as shown in Fig. 6.13. With increasing parasitic S/D resistance, the output characteristics were significantly degraded even at 1 μm.
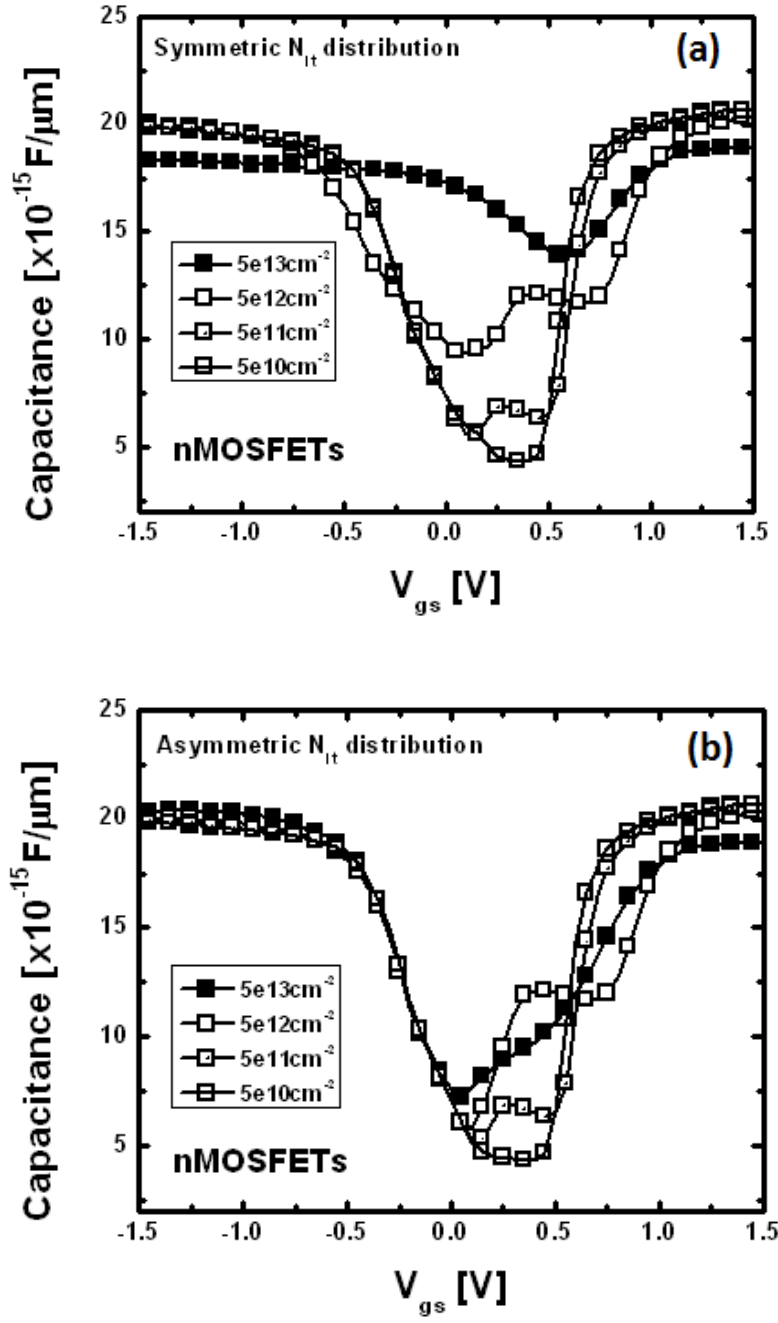
FIGURE 6.9: Capacitance-Voltage (CV) results for (a) symmetric and (b) asymmetric N_{it} distribution in SiGe nMOSFETs by TCAD device simulation.
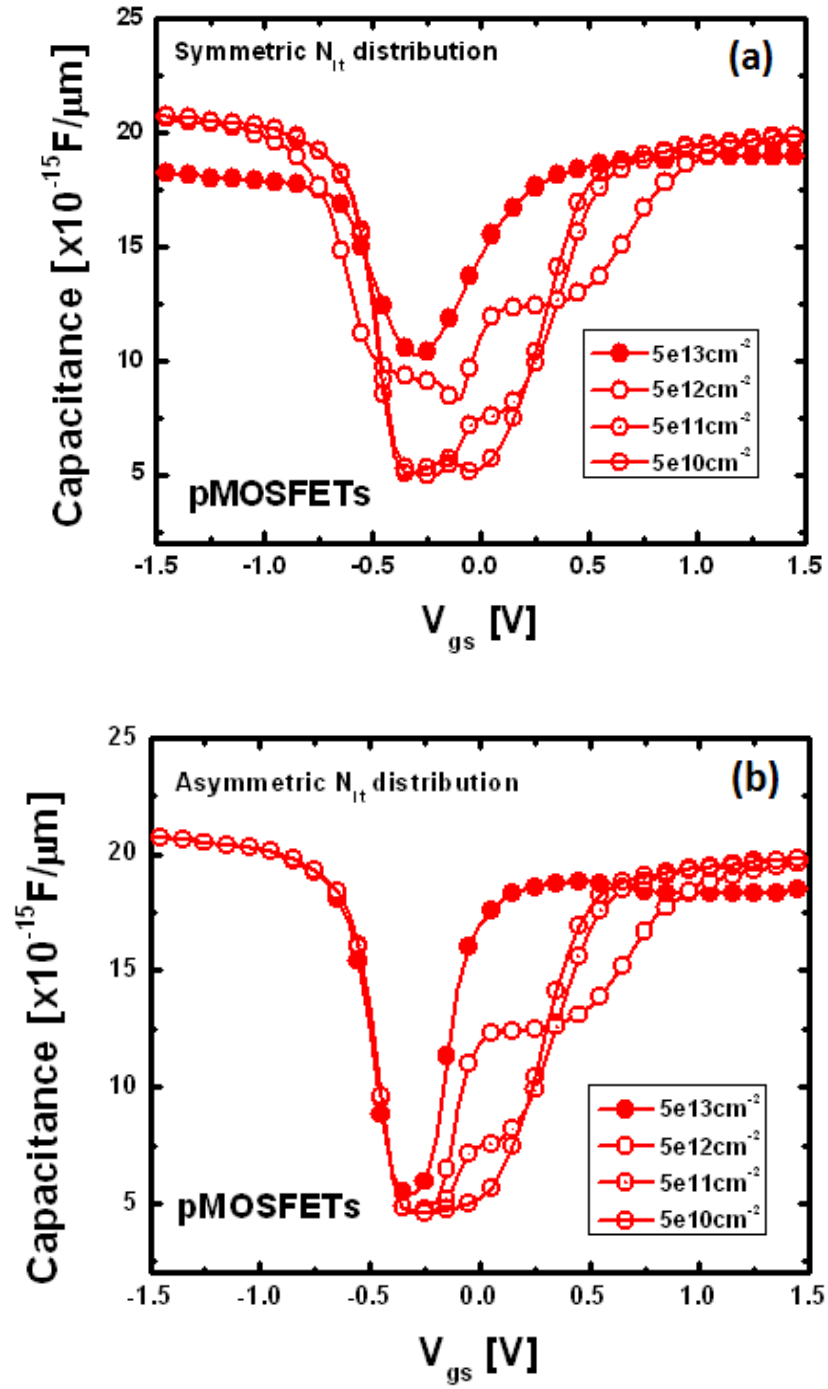
FIGURE 6.10: Capacitance-Voltage (CV) results for (a) symmetric and (b) asymmetric N_{it} distribution in SiGe pMOSFETs by TCAD device simulation.
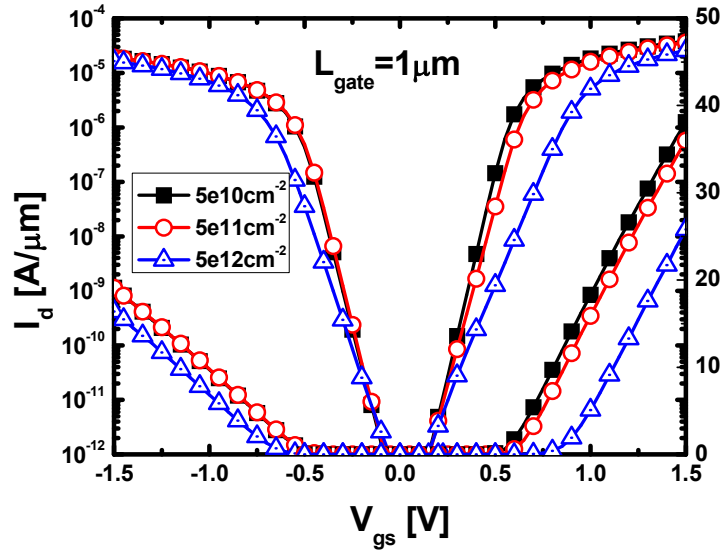
FIGURE 6.11: Simulated transistor $I_d V_g$ characteristics for SiGe n- and pMOSFETs with interface traps (N_{it}).
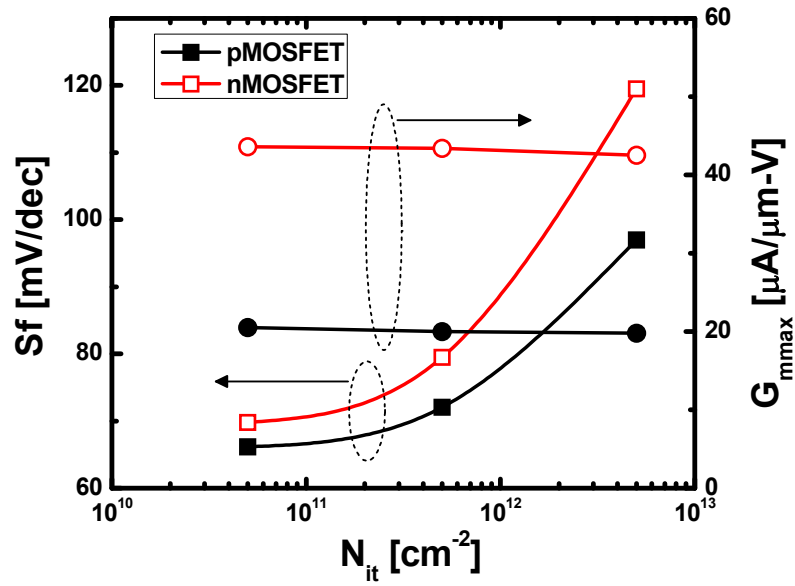
FIGURE 6.12: Simulated transistor S_f and G_{mmax} characteristics for SiGe n- and pMOSFETs with interface traps (N_{it}).
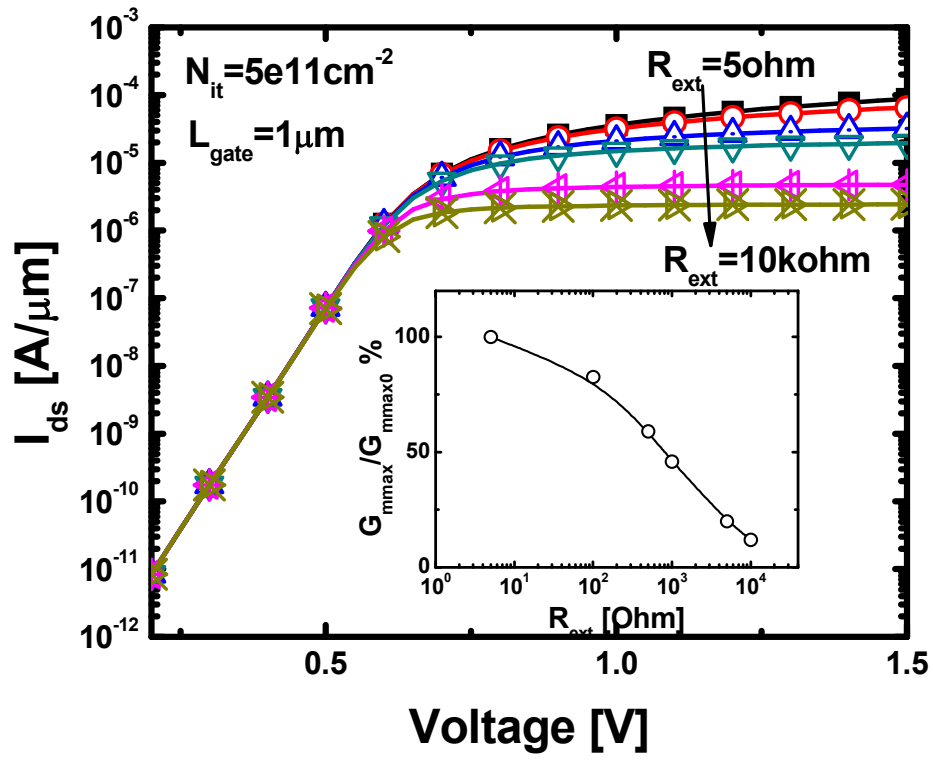
FIGURE 6.13: Simulated I_dV_g curve with parasitic resistance (R_{ext})

6.5 S/D SERIES RESISTANCE CHARACTERISTICS

External S/D series resistance (R_{ext}) for Si nMOSFETs and Ge nMOSFETs is extracted by the amount of channel resistance (R_{chan}) from total resistance (R_m) in Fig. 6.14. R_m can be obtained from Eq. (6).

$$R_m = \frac{V_{DS}}{I_{DS}} = \frac{L_{eff}}{\mu_s C_{ox} W_{eff}(V_{GS} - V_{th} - \frac{1}{2}V_{DS})}, \qquad (6)$$

$$R_m = \frac{V_{DS}}{I_{DS}} = R_{ds} + R_{chan} = R_{ds} + A(L_{mask} - \Delta L), \qquad (7)$$

$$A = (\mu_s C_{ox} W_{eff}(V_{GS} - V_{th} - \frac{1}{2}V_{DS})V_{DS})^{-1}$$
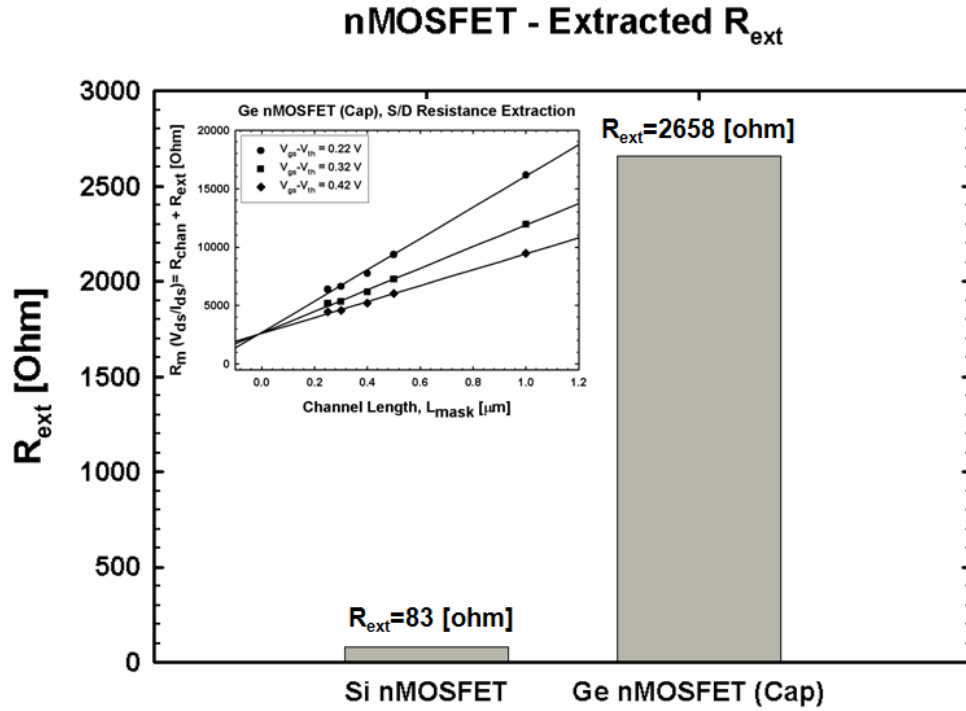
FIGURE 6.14: External S/D series resistance (R_{ext}) for Si nMOSFET and Ge nMOSFET. Rext is decoupled by the amount of channel resistance (R_{chan}) from total resistance (R_m). Rext is extracted from linear curves which are dependent on both gate biases and channel lengths. The inset is for Ge nMOSFET.
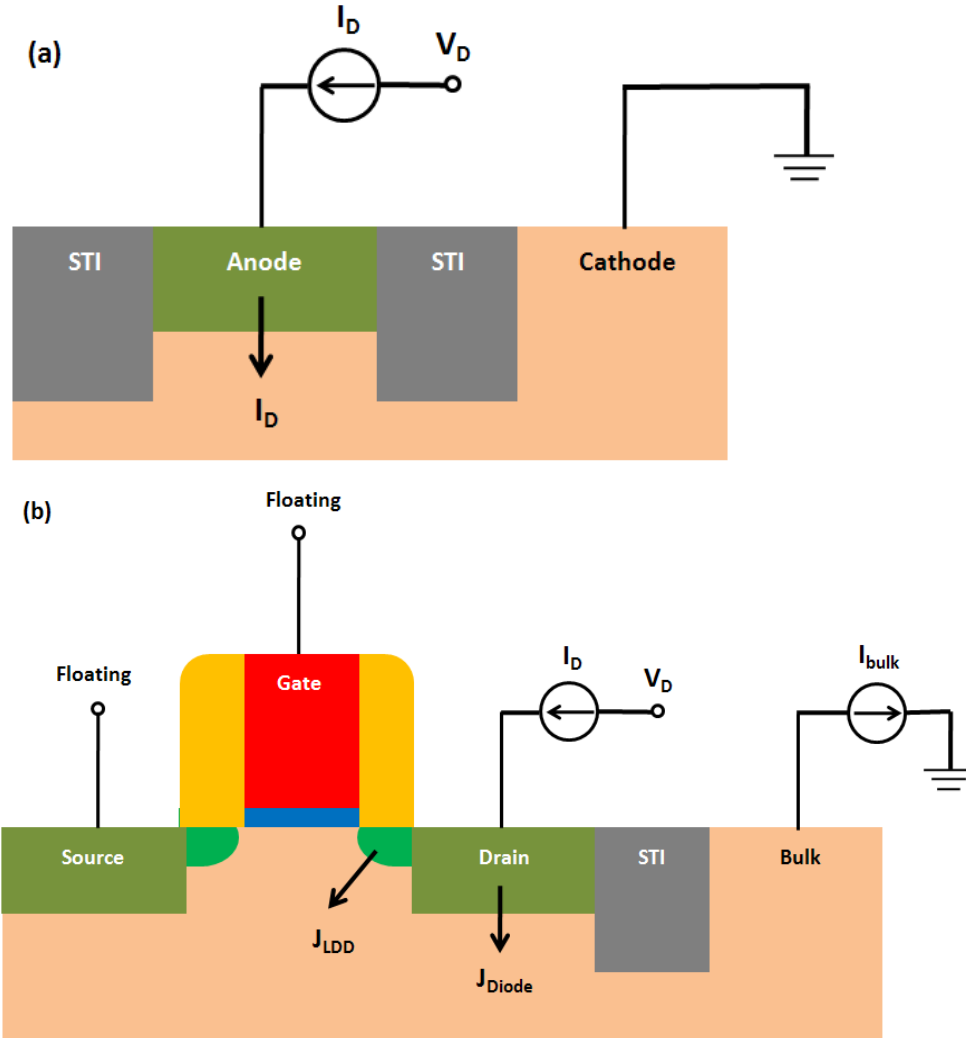
FIGURE 6.15: (a) Schematic diagram for diode structure and its current meansurement. (b) Schematic diagram for diode current measurement from drain to bulk in MOSFET.

R_{ext} is extracted from linear curves which are dependent on both gate biases and channel lengths in Eq. (7). Ge nMOSFETs has a significant high value for R_{ext} compared to Si nMOSFET. The extracted R_{ext} values for each sample devices are summarized in

Table 6.2. Considering the simulation results and the R_{ext} measurement, the primary cause of nMOSFETs G_m degradation is abnormal parasitic resistance rather than the high interface states. To indentify where this parasitic resistance is originated from, diode characteristics are monitored using n^+/p & p^+/n diode for areal characteristics and gated diode for extension diode characteristics.

The schematic diagram for diode structure and its current measurement is shown in Fig. 6.15 (a). Current-voltage (IV) characteristics in forward and reverse bias in Si, SiGe, and Ge p^+/n diode as well as n^+/p diode are shown in Fig. 6.16(a) and 6.16(b), respectively. In the reverse bias regions, SiGe p^+/n and n^+/p diode has a higher leakage current compared to Si and Ge p^+/n diode. In the forward bias regions, effective on-resistance (R_{diode}) is extracted from the slope. The detailed extracted values are summarized in Table 6.2. As a result, R_{diode} in Ge n^+/p and p^+/n diode has higher values than that in Si and SiGe n^+/p and p^+/n diode. R_{diode} in Ge n^+/p has 502 Ohm which is the highest value among the samples.
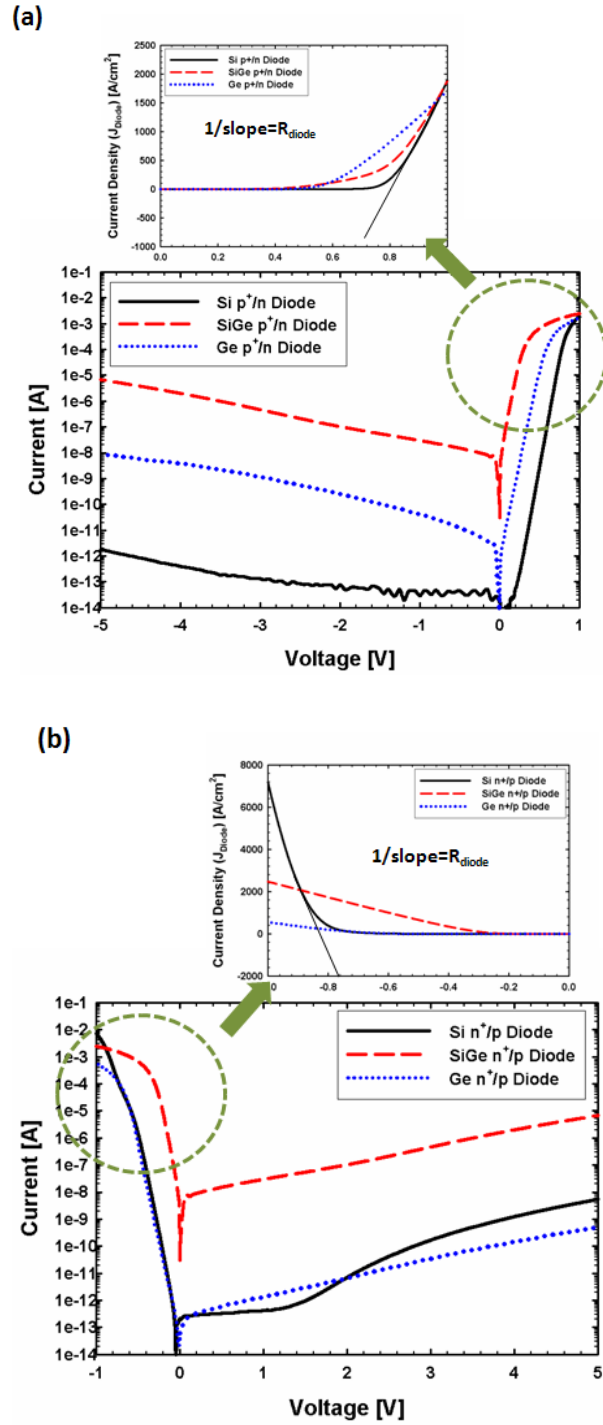
FIGURE 6.16: (a) IV characteristics in forward and reverse bias in Si, SiGe, and Ge p+/n diode. (b) IV characteristics in forward and reverse bias in Si, SiGe, and Ge n+/p diode. Effective on-resistance (Rdiode) is extracted from the slope in forward bias region.
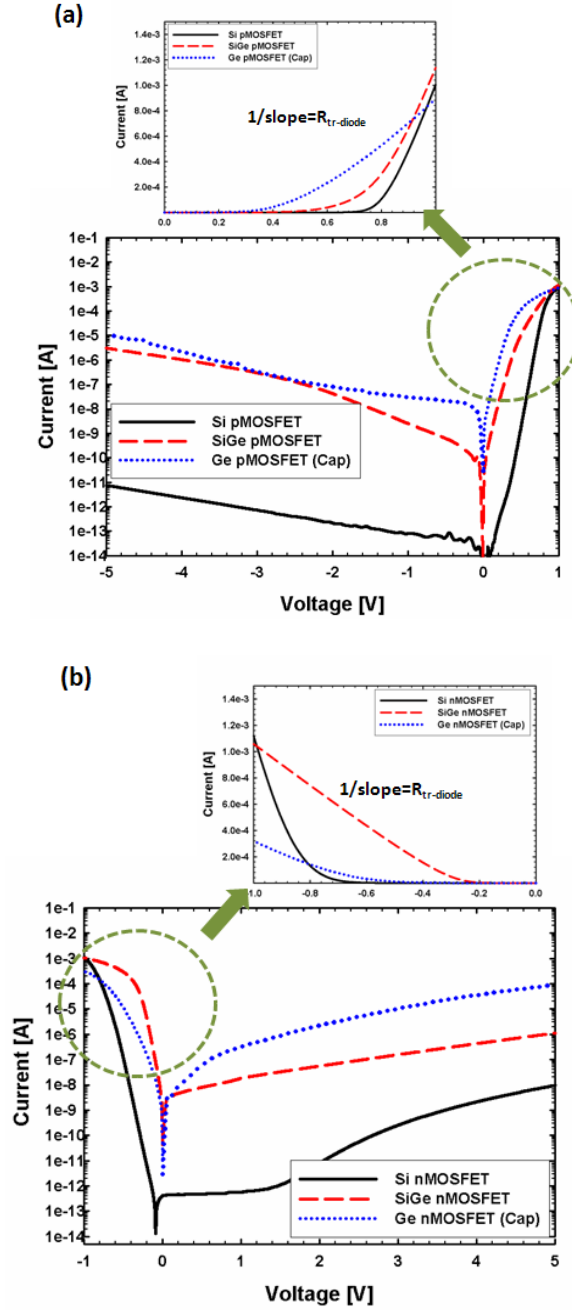
FIGURE 6.17: (a) IV characteristics from drain to bulk in forward and reverse bias in Si, SiGe, and Ge pMOSFET. (b) IV characteristics from drain to bulk in forward and reverse bias in Si, SiGe, and Ge nMOSFET. Effective on-resistance ($R_{tr-diode}$) is extracted from the slope in forward bias region.

The schematic diagram for diode current measurement from gated-diode MOSFET configuration is also shown in Fig. 6.15(b). IV characteristics from drain to bulk in forward and reverse bias in Si, SiGe, and Ge pMOSFET as well as nMOSFET is shown in Fig. 6.17(a) and 6.17(b), respectively. In the reverse bias regions, Ge pMOSFET and nMOSFET have a higher leakage current. In forward bias region, an effective on-resistance ($R_{gated-diode}$) is extracted from the slope, summarized in Table 6.2. As expected with previous simulation results, the highest $R_{gated-diode}$ is observed in Ge nMOSFET.

In the both diode structures, the Si control devices showed similar resistance while the SiGe and Ge devices showed higher resistance for n^+/p cases, which indicates that a huge voltage drop is occurred across the silicide and n^+ interface due to a greater Schottky barrier to the n^+ region. In addition, both n^+/p and p^+/n diodes exhibited increased reverse leakage for the SiGe and Ge devices, which can be explained by high interface states as simulated in Fig. 6.18.

From the results above, the reason of high R_{ext} for SiGe and Ge nMOSFETs is the high interface resistance in between the silicide and n^+ region because the workfunction of silicide is close to 4.5eV which provide less Schottky barrier height to p^+ doping in SiGe and Ge. Also it is expected that the total diode resistance for n^+/p and p^+/n is within the order range difference, which support that the interface resistance is the primary reason of nMOSFETs performance degradation. In conjunction with lowering interface states, thereby, junction engineering for reducing the interface resistance should be taken into account for SiGe and Ge n-type transistor design.
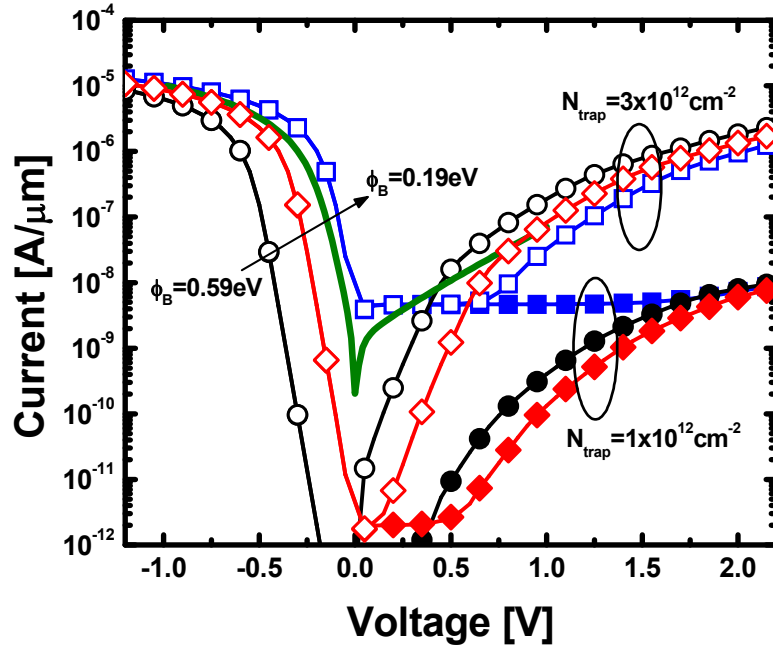
FIGURE 6.18: Simulated IV curves for n+/p diode with Schottky barrier (φB) and interface traps (N$_{trap}$).

TABLE 6.1: Key transistor parameters in Si, SiGe, and Ge MOSFETs

	CET [Å]	V$_{th}$ [V]		G$_{mmax}$/ C$_{ox}$ [S/F]		Sf [mV/dec]	
		nMOS	pMOS	nMOS	pMOS	nMOS	pMOS
Si	12	0.59	-0.68	4.3E+06	1.3E+06	71	70
SiGe	14	0.93	-0.20	7.3E+05	3.6E+06	129	80
Ge	14	0.73	-0.03	2.5E+05	2.5E+06	197	123

TABLE 6.2: Interface traps (D_{it}), external S/D series resistance (R_{ext}), and diode characteristics in Si, SiGe, and Ge MOSFETs.

	D_{it} [cm^{-2}eV^{-1}]	R_{ext} [Ohm]		$R_{gated-diode}$ [Ohm]		R_{diode} [Ohm]	
	nMOS	nMOS	pMOS	nMOS	pMOS	n$^+$/p Diode	p$^+$/n Diode
Si	7.1E+10	83	155	158	193	21	98
SiGe	8.3E+10	-	250	632	210	268	117
Ge	1.2E+13	2658	280	1045	524	502	218

6.6 SUMMARY

The origin of performance degradation in SiGe and Ge nMOSFETs was investigated with charge pumping technique and TCAD device simulation. Asymmetric and symmetric interface traps degrade subthreshold swing (Sf) and increase threshold voltage (V_{th}) in SiGe and Ge nMOSFETs. However, G_m degradation is originnated from significant amounts of parasitic series resistance in SiGe and Ge nMOSFET which can not be solely explained by high densities of interface trap distributions at the band edges. In order to confirm the results, the electrical characteristics for n$^+$/p and p$^+$/n diodes and gated diode MOSFETs are studied together with simulation results in order to support the hypothesis that the interface resistance is the primary reason of nMOSFETs performance degradation. We propose the possible reasons for performance degradation in SiGe and Ge nMOSFET together with simulation results. In conjunction with lowering interface state density, junction engineering for reducing the interface resistance should be taken into account for SiGe and Ge n-type transistor design.

6.7 REFERENCE

[1] International Technology Roadmap for Semiconductors (ITRS) 2007.

[2] S. J. Whang, S. J. Lee, N. Wu, C. X. Zhu, J. S. Pan, L. J. Tang, D. L. Kwong, "Germanium p- & n-MOSFETs fabricated with novel surface passivation (plasma-PH_3 and thin AlN) and TaN/HfO_2 Gate stack," in *IEDM Tech. Dig.*, 2004, pp.307-309.

[3] H. Shang, K. Lee, P. Kozlowski, C. D'Emic, I. Babich, E. Sikorski, M. Ieong, H.-S. P. Wong, K. Guarini, and W. Haensch, "Self-Aligned n-Channel Germanium MOSFETs With a Thin Ge Oxynitride Gate Dielectric and Tungsten Gate," *IEEE Electron Device Lett.*, vol. 25, no. 3, Mar. 2004.

[4] J. Oh, P. Majhi, H. Lee, O. Yoo, S. Banrejee, C. Y. Kang, J. Yang, R. Harris, H. Tseng, and R. Jimmy, "Improved Electrical Characteristics of Ge-on-Si Field Effect Transistors With Controlled Ge Epitaxial Layer Thickness on Si Substrates," *IEEE Electron Device Lett.*, vol. 28, no. 11, Nov. 2007.

[5] C. O. Chui, F. Ito, and K. C. Saraswat, "Nanoscale Germanium MOS Dielectrics-Part I: Germanium Oxynitrides," *IEEE Trans. Electron Devices*, vol. 53, no. 7, pp. 1501-1508, Jul. 2006.

[6] W. P. Bai, N. Lu, and D. L. Kwong, "Si Interlayer Passivation on Germanium MOS Capacitors With High-k Dielectric and Metal Gate," *IEEE Electron Device Lett.*, vol. 26, no. 6, pp. 378-380, Jun. 2005.

[7] J. P. Han, E. M. Vogel, E. P Gusev, C. D'Emic, C. A. Richter, D. W. Heh, J. S. Suehle, "Energy Distribution of Interface Traps in High-k Gated MOSFETs," in *VLSI Symp. Tech. Dig.*, 2003, pp. 161-162.

[8] J. P. Han, E. M. Vogel, E. P. Gusev, C. D'Emic, C. A. Richter, D. W. Heh, and J. S. Suehle, "Asymmetric Energy Distribution of Interface Traps in n- and p-MOSFETs With HfO_2 Gate Dielectric on Ultrathin SiON Buffer Layer," *IEEE Electron Device Lett.*, vol. 25, no. 3, Mar. 2004.

[9] P. Zimmerman, G. Nicholas, B. D. Jaeger, B. Kaczer, A. Stesmans, L. A. Ragnarsson, D. P. Brunco, F. E. Leys, M. Caymax, G. Winderickx, K. Opsomer, M. Meuris, and M. M. Heyns, "High performance Ge pMOS devices using a Si-compatible process flow," in *IEDM Tech. Dig.*, 2006, pp. 1-4.

[10] T. Takahashi, T. Nishimura, L. Chen, S. Sakata, K. Kita, and A. Toriumi, "Proof of Ge-interfacing Concepts for Metal/High-k/Ge CMOS ," in *IEDM Tech. Dig.*, 2007, pp. 697-700.

[11] Q. Zhang, J. Huang, N. Wu, G. Chen, M. Hong, L. K. Bera, and C. Zhu, "Drive-Current Enhancement in Ge n-Channel MOSFET Using Laser Annealing for Source/Drain Activation," *IEEE Electron Device Lett.*, vol. 27, no. 9, Sep. 2006.

[12] W. P. Bai, N. Lu, A. Ritenour, M. L. Lee, D. A. Antoniadis, and D. L. Kwong, "Ge n-MOSFETs on Lightly Doped Substrates With High-k Dielectric and TaN Gate," *IEEE Electron Device Lett.*, vol.26, no.3, Mar. 2006.

[13] R. Xie, Nan Wu, C. Shen, and C. Zhu, "Energy distribution of interface traps in germanium metal-oxide-semiconductor field effect transistors with HfO_2 gate dielectric and its impact on mobility," *Appl. Phys. Lett.* **93**, 083510 (2008).

[14] K. Tori, Y. Shimamoto, S. Saito, O. Tonomura, M.Hiratani, Y. Manabe, M. Caymax, and J. W. Maes, "The mechanism of mobility degradation in MISFETs with Al_2O_3 gate dielectric," in *VLSI Tech. Symp. Dig.*, 2002, pp. 188-189.

[15] M. V. Fischetti, D. A. Neumayer, and E. A. Cartier, "Effective electron mobility in Si inversion layers in metal-oxide-semiconductor systems with high-k insulator: The role of remote phonon scattering," *J. Appl. Phys.*, vol. 90, no. 9, pp. 4587-4608, 2001.

[16] E. P. Gusev, D. A. Buchanan, A. Kumar, D. DiMaria, S. Guha, A. Calegari, S. Zafar, P. C. Jamison, D. A. Neumayer, M. Copel, M. A. Gribelyuk, H. Okorn-Schmidt, C. D'Emic, P. Kozlowski, K. Chan, N. Bojarczuk, and L. A.Ragarsson, " Ultrathin high-k gate stacks for advanced CMOS devices," in *IEDM Tech. Dig.*, 2001, pp. 451-454.

[17] W. J. Zhu, T. P. Ma, S. Zafre, and T. Tamagawa, "Charge Trapping in ultrathin hafnium oxide," *IEEE Electron Device Lett.*, vol. 23, no. 12, pp.597-599, Dec. 2002.

[18] N. Wu, Q. Zhang, N. Balasubramanian, D. S. H. Chan, and C. Zhu, " Characteristics of Self-Aligned Gate-First Ge p- and n-Channel MOSFETs Using CVD HfO_2 Gate Dielectric and Si Surface Passivation," *IEEE Trans. Electron Devices*, vol. 54, no. 4, Apr. 2007.

[19] K. Martens, B. Kaczer, T. Grasser, B. De Jaeger, M. Meuris, H. E. Maes, and G. Groeseneken, "Applicability of Charge Pumping on Germanium MOSFETs," *IEEE Electron Device Lett.*, vol. 29, no. 12, pp. 1364-1366, Dec. 2008.

[20] D. Kuzum, T. Krishnamohan, A. J. Pethe, A. K. Okyay, Y. Oshima, Y. Sun, J. P. McVittie, P. A. Pianetta, P. C. McIntyre, and K. C. Saraswat, "Ge-Interface Engineering With Ozone Oxidation for Low Interface-State Density," *IEEE Electron Device Lett.*, vol. 29, no. 4, pp. 328-330, Apr. 2008.

[21] K. Martens, C. O. Chui, G. Brammertz, B. D. Jaeger, D. Kuzum, M. Meuris, M. M. Heyns, T. Krishnamohan, K. Saraswat, H. E. Maes, and G. Groeseneken, "On the Correct Extraction of Interface Trap Density of MOS Devices With High-Mobility Semiconductor Substrates," *IEEE Trans. Electron Devices*, vol. 55, no. 2, pp. 547-556, Feb. 2008.

[22] D. Kuzum, A. J. Pethe, T. Krishnamohan, Y. Oshima, Y. Sun, J. P. McVittie, P. A. Pianetta, P. C. McIntyre, and K. C. Saraswat, "Interface-Engineered Ge (100) and

(111), N- and P-FETs with High Mobility", in *IEDM Tech. Dig.*, 2007, pp. 723-726.

[23] K. Martens, B. D. Jaeger, R. Bonzom, J. V. Steenbergen, M. Meuris, G. Groeseneken, and H. Maes, "New Interface State Density Extraction Method Applicable to Peaked and High-Density Distributions for Ge MOSFET Development," *IEEE Electron Devices Lett.*, vol. 27, no. 5, May 2006.

[24] Synopsys Sentaurus Packages and Medici, Version A-2008.09, Synopsys Inc.

[25] R. People and J. C. Bean, "Calculation of critical layer thickness versus lattice mismatch for Ge_xSi_{1-x}/Si strained-layer heterostructures," *Appl. Phys. Lett.*, vol. 47, no. 3, pp. 322-324, Aug. 1985.

[26] G. Groeseneken, H. E. Maes, N. Beltran, and R. F. De Keersmaecker, "A reliable approach to charge-pumping measurements in MOS transistors," *IEEE Trans. Electron Devices*, vol. ED-31, no. 1, pp. 42-53, Jan. 1984.

[27] M. T.-Luque, R. Degraeve, M. B. Zahid, L. Pantisano, E. S. Andres, G. Groeseneken, and S. D. Gendt, "New Developments in Charge Pumping Measurements on Thin Stacked Dielectrics," *IEEE Trans. Electron Devices*, vol. 55, no. 11, Nov. 2008.

[28] S. S. Chung, S.-J. Chen, C.-K. Yang, S.-M. Cheng, S.-H. Lin, Y.-C. Sheng, H.-S. Lin, K.-T. Hung, D.-Y. Wu, T.-R. Yew, S.-C. Chien, F.-T. Liou, and F. Wen, "A Novel and Direct Determination of the Interface Traps in Sub-100nm CMOS Devices with Direct Tunneling Regime (12-16A) Gate Oxide," in *VLSI Symp. Tech. Dig.*, 2002, pp. 74-75.

[29] S. S. Chung, Y. R. Liu, C. F. Yeh, S. R. Wu, C. S. Lai, T. Y. Chang, J. H. Ho, C. Y. Liu, C. T. Huang, C. T. Tsai, W. T. Shiau, and S. W. Sun, "A New Observation of the Germanium Outdiffusion Effect on the Hot Carrier and NBTI Reliabilities in Sub-100nm Technlogy Strained-Si/SiGe CMOS Devices," in *VLSI Symp. Tech. Dig.*, 2005, pp. 86-87.

[30] T. Tsuchiya, Y. Imada, and Junichi Murota, "Direct Measurements of Trap Density in a SiGe/Si Hetero-Interface and Correlation Between the Trap Density and Low-Frequency Noise in SiGe-Channel pMOSFETs," *IEEE Trans. Electron Devices*, vol. 50, no.12, Dec. 2003.

[31] E. Simoen, M. B. Gonzalez, B. Vissouvanadin, M. K. Chowdhury, P. Verheyen, A. Hikavyy, H. Bender, R. Loo, C. Claeys, V. Machkaoutsan, P. Tomasini, S. Thomas, J. P. Lu, J. W. Weijtmans, and R. Wise, "Factors Influencing the Leakage Current in Embedded SiGe Source/Drain Junctions", *IEEE Trans. Electron Devices*, vol. 55, no. 3, Mar. 2008.

CHAPTER 7: CONCLUSIONS

7.1 CONCLUSIONS

In chapter 2, we presented a first-principles study of the structure and dynamics of small As-interstitial complexes (AsI_2, As_2I_2, AsI_3, and As_2I_3) in Si. The compact configurations of AsI_3^c and $As_2I_3^c$ are expected to dissociate easily and the extended configuration, $As_2I_3^{ext}$, forms a stable bonding network and has a strong binding energy of 2.64 eV. In presence of excess Si interstitials and high As concentration, As_2I_2 could be a key intermediate state and $As_2I_3^{ext}$ could provide a key nucleation site in the formation of larger As-interstitial clusters. A diffusion mechanism for neutral AsI_2 is proposed with an overall migration barrier of 0.36 eV. Our results show that AsI_2 may significantly contribute to As TED in the presence of excess Si interstitials. A novel diffusion mechanism for neutral As_2I_2 is suggested with an overall migration barrier of 1.03 eV and an intermediate, reoriented configuration with an energy of 0.42 eV. This detailed understanding of the relative roles of small As-interstitial complexes can provide valuable guidance for ultrashallow junction engineering.

In chapter 3, we have studied As-vacancy and interstitial-mediated As diffusion in strained Si by using DFT calculations. First, biaxial tensile strain was found not to significantly affect As deactivation. Second, tensile strain increases the stability of As-Si$_i$ pairs. Finally, an interstitial-mediated As diffusion in heavily As-doped Si will not be significantly affected by induced biaxial tensile strain.

In chapter 4, DFT-based first principles calculation to investigate the boron diffusion retardation in the presence of Ge was performed. First, the concentration of Ge-B pair is smaller than that of Si-B pair due to a lower binding energy of BI pair and

115

higher migration energy of Ge^I. Second, the diffusion direction of Si-B pair will prefer to be in the directions where substitutional Ge atom doesn't exist, resulting in a slow diffusion process of Si-B pair with higher Ge concentrations. Third, Si-Ge dumbbell will trap mobile Si^I available for {311} extended defects or dislocation loops and in turn reduce the overall density of Si extended defects. Moreover, the localization of Si^I by small clusters will open a possibility to segregate at the interface during damage annealing. The underlying mechanism we present in this work should contribute to developing an improved physical model for highly p-type ultrashallow junction transistors.

In chapter 5, a systematic study was performed to understand the mechanism of boron diffusion in SiGe/Si substrates. To improve the short channel behavior, SiGe thickness and Ge concentration should be carefully selected. In a given SiGe/Si substrate, Ge PAI can improve the short channel margin because boron diffusion is mitigated. There is a trade-off in terms of the impact of fluorine on short channel behavior and reliability characteristics.

In chapter 6, the origin of performance degradation in SiGe and Ge nMOSFETs was investigated with charge pumping technique and TCAD device simulation. Asymmetric and symmetric interface traps degrade subthreshold swing (Sf) and increase threshold voltage (V_{th}) in SiGe and Ge nMOSFETs. However, G_m degradation originates from significant amounts of parasitic series resistance in SiGe and Ge nMOSFET which cannot be solely explained by high densities of interface trap distributions at the band edges. In order to confirm the results, the electrical characteristics for n^+/p and p^+/n diodes and gated diode MOSFETs are studied together with simulation results in order to support the hypothesis that the interface resistance is the primary reason of nMOSFETs performance degradation. We proposed the possible reasons for performance degradation

116

in SiGe and Ge nMOSFET together with simulation results. In conjunction with lowering interface states, junction engineering for reducing the interface resistance should be taken into account for SiGe and Ge n-type transistor design.

Vita

Yonghyun Kim entered Chonnam National University in March of 1996. He graduated Summa Cum Laude from Chonnam National University with a Bachelor of Science in Electronics Engineering in February of 2000. In order to pursue Master degree, he entered Graduate School in Electrical Engineering and Computer Science in Seoul National University under the supervision of Prof. Sin-Doo Lee. In February of 2000, he received M.S. degree in the area of liquid-crystal (LC) display and LC optical filters. In order to pursue Ph.D degree, he entered Graduate School in Electrical and Computer Engineering in the University of Texas at Austin in August of 2004 and was admitted to Ph.D candidacy under the supervision of Prof. Sanjay K. Banerjee in July of 2008. During his doctoral study, he received National Fellowship from the Ministry of Information and Communication in South Korea in August of 2004. He also received Applied Material Graduate Fellowship with a full tuition and fees for two years from Applied Materials Inc. in September of 2006. He worked as an intern at SEMATECH at Austin from June of 2007 to May of 2009 and as a full-time intern at Intel Corp. at Austin from August of 2009 to May of 2010. He continues his career as a product development engineer at Intel Corp. at Austin.

Permanent address: 3607 Greystone Dr. 921, Austin, TX 78731, USA

Permanent email: erogen@gmail.com

This dissertation was typed by Yonghyun Kim.